Elastic measurements in ultra-thin polymer structures

by David Farmer MSci (Hons.)

Thesis submitted to the University of Nottingham

for the degree of Doctor of Philosophy

June 2015

School of Physics and Astronomy

Abstract

This thesis contains details of a series of experiments performed to investigate the acoustic and elastic properties of ultra-thin polymer structures.

Three main investigations were conducted. The first involved studying quantised vibrations in ultra-thin (∼100 nm) polystyrene films on silicon substrates. These films were vibrated via the picosecond acoustic technique, an optical pump-probe method.

Quantised, harmonic vibrations were observed in the films with frequencies of the order of 10 GHz. The polymer films were then loaded by evaporating small thicknesses (2.5 - 30 nm) of gold. The frequencies of loaded areas were observed relative to the unloaded films.

This frequency shift is described via a theory that considers the elastic wave equation in the structure with appropriate boundary conditions. Excellent agreement between experiment and theory is achieved, suggesting the potential for using these films as ultra-sensitive mass sensors.

The second experimental chapter deals with experiments performed on polymer Bragg reflectors. These multilayer structures were again investigated via the picosecond technique. The reflected intensity of the probe laser beam was observed to be modulated by the strain pulse as it travelled through the structure.

These results were compared to theoretically generated signals and this comparison suggests that, in the polymer structures considered here, the modulation can be described almost exclusively by the photo-elastic effect.

Although the modulation is small it opens up the possibility of using similar structures in combinations with micro-cavities to act as high frequency optical components.

The final experimental chapter details attempts to develop a new metrol-

ogy for elastic properties in ultra-thin polymer films floated on a water surface. The films were cut into annuli and placed on a Langmuir-Blodgett trough before surfactant was placed around the outside. By moving the barriers of the trough, a surface pressure difference between the inside and outside of the annulus could be controlled and a wrinkling pattern induced around the annulus.

A system for imaging and counting the wrinkles as a function of the surface pressure difference was developed and a theory that attempts to describe this is detailed. While the experimental technique is successful in producing highly controlled, reproducible wrinkles, the theoretical analysis currently overestimates the Young's modulus of the films. The reasons for this as well as avenues for further work are considered.

The results of these three investigations all demonstrate the rich physics accessible in ultra-thin polymer films. Furthermore, it points to their potential to be a key material as devices are more commonly manufactured at the nano-scale.

Publications and Conferences

The following two publications were the direct result of the work detailed in Chapters 4 and 5 respectively.

- Farmer, D. J., Akimov, A. V., Sharp, J. S. & Kent, A. J. *Quantized phonon modes in loaded polymer films.* J. Appl. Phys. **113**, 033516 (2013).
- Farmer, D. J., Akimov, A. V., Gippius, N. A., Bailey, J, Sharp, J. S. & Kent, A. J. *High-frequency acousto-optic effects in Bragg reflectors.* Opt. Express **22**, 15218-31 (2014).

The experiments conducted in Chapter 6 were selected for an oral presentation at

- 2014 APS March Meeting, March 3-7, Denver, CO

♫

I've loved, I've laughed and cried

I've had my fill, my share of losing

And now, as tears subside, I find it all so amusing

To think I did all that...

♫

Acknowledgements

There are, understandably, many people I need to thank for their help in the four years this has taken. First, obviously, is my supervisor, James. I can't imagine having had a better supervisor for my work, or one more supportive of all the extra-curricular activities I chose to pursue. More importantly, at a time of real personal difficulty for myself the level of support offered was above and beyond what could reasonably be expected. I'm lucky to have had you as a boss and a friend.

I am thankful to my immediate colleagues in the polymer group, in particular Mike Smith and James Bailey, who were always available to help or offer advice. This thanks extends to the entire Nanoscience group at Nottingham, a great bunch of colleagues and friends. I am sorry I spent so much time trying to get you to do outreach when we should have been in the lab!

There are too many friends and family who have supported me over the years to name them individually. I am a lucky guy to have been surrounded by people so willing to share a drink or two and listen to me rant or complain. The next round is on me.

And the final thanks, of course, to Nikki. For everything. We are running out of excuses not to organise this wedding...

Contents

1. Introduction

1.1 Soft Matter

We live in a world of soft materials. Our food, our clothes, the packaging they come in are all made from soft materials. Indeed, we ourselves are composed of soft materials. When then does something become 'soft'?

As a field, soft condensed matter is broad in its scope. It deals with materials that are neither simple liquids, nor crystalline solids. Instead, they display degrees of ordering that lay somewhere in between these extremes. The length scales considered in their study are also intermediate, lying between the atomic and the macroscopic.

These complex systems were often thought of as 'messy' or 'untidy'. As such, they were traditionally left to chemists or physical chemists to study. Progress in the physics of the field has been relatively recent, facilitated in a great part by the work of 'the father of soft condensed matter', Pierre-Gilles de Gennes.

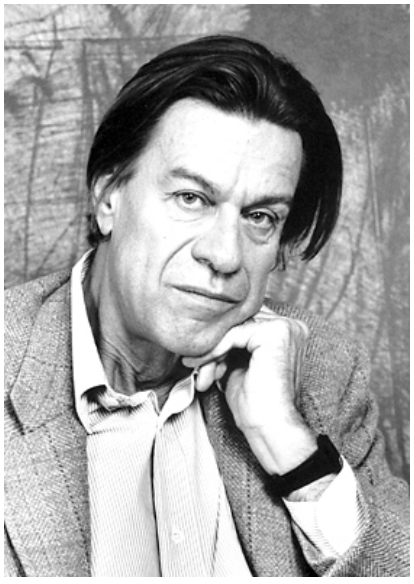

Figure 1.1: Pierre-Gilles de Gennes (1932 - 2007)

De Gennes was awarded the Nobel Prize in Physics in 1991 "for discovering that methods developed for studying order phenomena in simple systems can be generalized to more complex forms of matter, in particular to liquid crystals and poly-

mers". His work allowed these complicated, mesoscopic systems to be studied in a new light and kickstarted the expansion of the field of soft condensed matter in to the active, interdisciplinary area of research it is today.

Why though, is this field of messy, untidy materials of such interest? Beyond the rich physics that these systems display, they tend to share some general properties that make them of potential use. The intermediate size of the constituent parts often still allows for Brownian motion and fluctuations to occur. This in turn grants the ability for many soft matter systems to move towards an equilibrium and thereby self assemble. The self assembled states can often have complex or potentially useful structures.

In addition, when the low cost and ease of manufacturing such complicated structures from soft materials when compared with the often prohibitive cost and complexity of achieving the same with crystalline or 'hard' materials is a driving force behind much of the research in the field today. When the tendency of self assembled states to further order in a hierarchical fashion is considered, it is obvious that there is great potential for soft materials to revolutionise manufacturing in a range of fields, from the nano-scale up.

1.2 Polymers

One of the more important areas of soft condensed matter, and the subject of this thesis, is that of polymers. They are long, chain like molecules formed from many repeating units. Indeed, the name 'polymer' is simply the Greek for 'many-parts'.

This name was coined in the early 19th Century by the famous Swedish chemist Jöns Jacob Berzelius, although he initially used it to describe organic compounds with the same empirical formula but different molecular weights. Given they were being studied as long ago as this, it is perhaps surprising that some doubted their existence as late as the 1940's, refusing to believe single molecules could be so large [1].

It is the size and chain like nature of polymers that gives rise to many of their interesting physical properties. There are three main parameters that can be used to describe this size. The simplest, perhaps, is the degree of polymerisation, often denoted N. This is the number of repeat units, or 'monomers' that form the polymer chain.

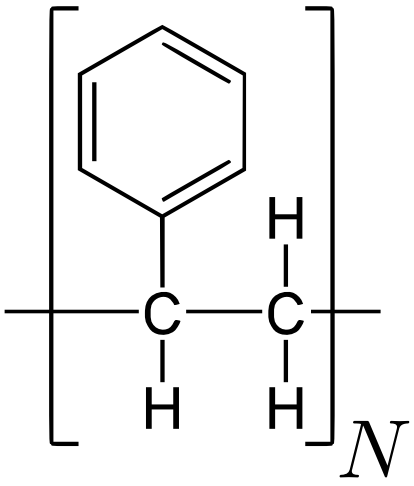

Figure 1.2: The chemical structure of a common polymer: polystyrene. This shows the repeating monomer unit where N is the degree of polymerisation.

The other two are measures of the molecular weight of polymers. The first, the Number Average Molecular Weight, M_n, is simply the total weight of all the polymer molecules in a sample divided by

the number of molecules. That is:

$$M_n = \frac{\Sigma_i N_i M_i}{N_i} \tag{1.1}$$

where M_i is the weight of a chain and N_i is the number of chains of that molecular weight.

The second is the Weight Average Molecular Weight, M_w. This is a weighted average so gives a measure of the molecular weight of the 'average' polymer chain in the sample. It is defined as so:

$$M_n = \frac{\Sigma_i N_i M_i^2}{\Sigma_i N_i M_i} \tag{1.2}$$

The fact that two measures are needed is indicative of the fact that in any real polymer sample there will be a distribution of chain lengths (or degree of polymerisation). An idea of how broad the distribution is is given by the polydispersity, $PD = M_w/M_n$, Clearly, for an ideal sample where all chains are the same length this will tend towards one.

It is not the case, however, that every polymer is a simple, un-branched chain, they can take many different forms. Some common architectures are shown in Fig. 1.3 but they are a small sample of the possible structures. The picture is further complicated when one considers block copolymers - where two different polymers are covalently bonded together as one chain. These have a rich variety of structures as well and can be further changed by modifying the relative lengths of each block.

As well as block copolymers, there are also random copolymers. These are formed of a random combination of different monomer units, again covalently bonded together. The properties of such copolymers tend to be intermediate between those of the homopolymers of the different monomer units.

Beyond synthetic polymers, there are also plentiful examples in nature of polymer chains. The ubiquitous natural rubber, harvested from trees

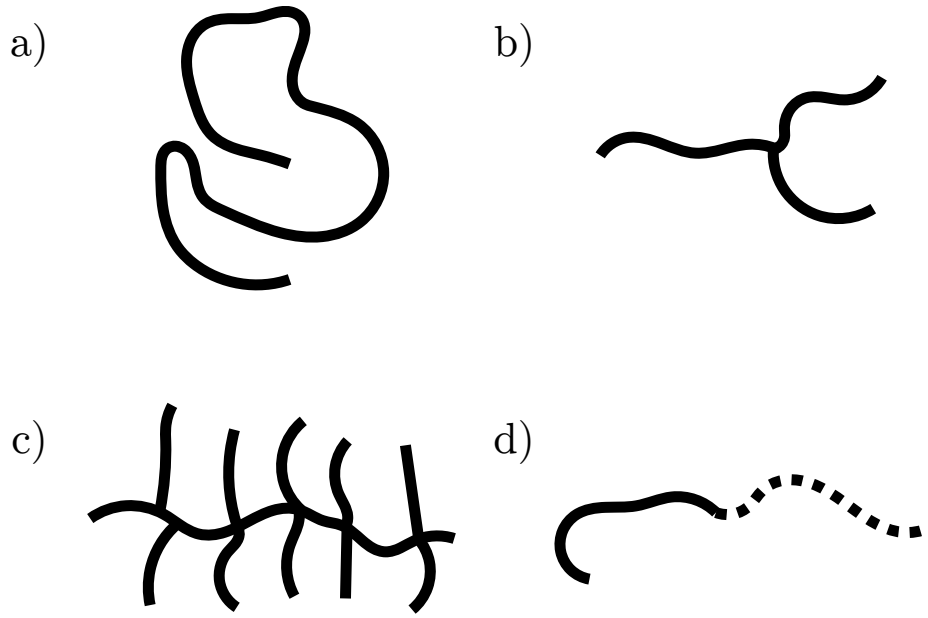

Figure 1.3: A selection of common polymer architectures: a) linear chain; b) branched chain; c) bottle brush; d) linear block copolymer. Block copolymers are chains where two or more different polymers are chemically bound together.

and historically used in so many different products and areas of manufacturing is simply polyisoprene [2]. Moreover, more complex polymers such as proteins and DNA form key parts of our biological make up [3]. These are both examples of sequenced copolymers, where a specific combination of monomers, nucleotides in the case of DNA or amino acids in the case of proteins combine to form the polymer chain.

There is a very wide variety of properties, and hence, uses of polymers due to the very wide range of different chemical structures they can take. Common examples of applications of polymers include elastomers such as the rubber used in tyres; plastics such as polyethylene or polystyrene, used for packaging, insulation or coatings; or fibres including natural materials such as cotton or wool, but also man made fibres such as nylon or acrylic.

It should be noted, however, that despite the wide range of chemical structures, polymer's physical properties often share universal characteris-

tics. This is primarily because the physics describing them is dominated by the fact that, regardless of their chemical properties, they are long stringy molecules that can't cross through each other.

Beyond the potential of their different chemistries and their many current applications, polymers offer great potential as materials for manufacturing a range of devices at the nano-scale. Structures of this size can routinely be fabricated via methods such as the spin coating of ultrathin films, a key technique for the work in this thesis [4]. They also share the common property of soft materials in that, given the right conditions, they can self assemble into a wide range of structures with domain spacings comparable to the size of the polymers themselves [3]. Examples of this include thin films of block copolymers ordering in to a range of structures depending on the relative lengths of the blocks [5, 6].

1.3 Motivation

As we seek to improve the technology in our lives, there is an increasing push towards minimising the size of this technology and the components it is formed of. A variety of devices from circuits and transistor chips to optoelectronic components are now routinely processed at nanometre length-scales. There are inherent difficulties, however, associated with these ultra-small devices.

Engineering and processing 'hard' crystalline materials with nanometre dimensions can be tricky, time-consuming and expensive. A common technique for creating structures of this size, for example, is molecular beam epitaxy. While capable of producing extremely thin layers of material, the technique relies on expensive ultra-high vacuum systems, as well as lengthy growth times. In contrast, soft materials, including polymers, offer an attractive route toward simplifying the manufacture of nanostructured devices thanks to the relative ease of their processing.

If then, soft materials are to be viable alternatives to hard condensed matter we need to further our understanding of their properties at the nanoscale. It is of particular importance for polymers, where the molecular size can approach tens of nanometres. It is clear that when molecules of this size are confined to similar dimensions then their mechanical properties may start to deviate significantly from the bulk.

This thesis is concerned specifically with the elastic properties of, and deformations in, ultrathin polymer structures. At these lengthscales, devices are likely to be sensitive to very small deformations and so it is important to understand how soft materials respond. One can imagine, for example, an optical reflector tuned to a specific wavelength of light. If a small vibration affects the structure in such a way as to change its optical properties then the device may be rendered useless unless this effect is

accounted for and understood.

It is important to understand that when we are discussing vibrations in ultrathin polymer structures we are firmly in the hypersonic regime, that is, vibrational modes of the order of GHz. The development of acoustic devices in this frequency range is a challenging task but promises new and attractive applications [7] [8] such as nanosensing [9] [10] or optical cooling [11] [12].

Clearly, if polymers are to provide a viable route for manufacturing devices such as these we need to understand their elastic properties in this regime as it is these which ultimately govern the acoustic response. It is this which motivates the hypersonic measurements of polymer films contained in this thesis.

The high frequency investigations of polymer nanostructures fit in the broader field of probing the physics and mechanical properties of polymers at the nanoscale. It is in this context that the experiments reported in this thesis were undertaken - aiming to characterise the elastic properties and investigate possible applications of polymer structures.

1.4 Thesis structure

This work is primarily composed of three separate experimental investigations. While they all focus on elastic measurements in ultra-thin polymer structures they have different goals and focuses. To this end, we start by covering some of the underlying concepts of polymer physics in Chapter 2. Chapter 3 then covers some of the reoccurring techniques used to process and characterise the films and multi-layers being studied.

The first experimental chapter, Chapter 4, details the results of experiments where high frequency acoustic measurements were performed on a polystyrene film. The film was loaded with varying thickness of gold and the shift in the frequency of the vibration of the films was determined. The results, along with the theory to support them are presented and analysed and possible applications discussed.

Chapter 5 also deals with high frequency acoustic measurements. In this case, the structure in question is not simple loaded film but a multi-layered polymer Bragg reflector. The effect on the optical properties of the reflector when an acoustic pulse travels through it is calculated and compared with the experimentally determined signals.

The final experimental chapter, Chapter 6, deviates from the high frequency measurements. Instead, it details the results of experiments performed where wrinkles were induced in ultra-thin, floated polymer annuli by controlling the surface tension both inside and outside the annulus. A theory is presented to describe both the onset and subsequent wavelength of the wrinkles. Characterising the way this wrinkling occurs allows the potential to measure the elastic properties of ultrathin films. This continues the efforts of the previous two chapters at probing the elastic properties of polymer nanostructures although it should be noted that these measurements take place in an entirely different frequency regime to the hypersonic

experiments.

Finally, Chapter 7 provides a brief conclusion to the work.

2. Polymer Theory

In this chapter we will cover some of physics that underpins polymer molecules. We then take a look specifically at the way elasticity arises in polymers.

2.1 Key physics

It is time to introduce some of the key physical concepts behind our understanding of polymer molecules. As mentioned above, these often messy systems are hard to describe rigorously. It is possible, however, to make significant progress understanding them using scaling laws and considering an 'ideal' chain.

The ideal polymer chain

The fact that they are long stringy molecules dominates the physics of polymers. They are not simply straight, unbent chains though. They are often curled and coiled back upon themselves, like an untidy pile of rope. To get an idea of the size of these molecules, there are two lengths we can define for an ideal polymer chain.

The first is the *contour length*, R_{contour}. This is simply the the total length of the polymer chain and can be written as the degree of polymerisation, or number of monomers, N times the length of a single monomer, a.

$$R_{\mathrm{contour}} = Na \tag{2.1}$$

The simplest model of a polymer, our ideal chain, treats each monomer as having an independent, random orientation to its neighbours. This means that the molecule as a whole can be described as an ideal random

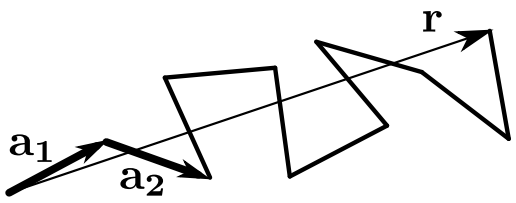

Figure 2.1: An 'ideal' polymer chain. Each monomer can be represented as a vector, $\mathbf{a_i}$. The end to end vector is labelled $\mathbf{r}$.

walk.

The second length we are interested in then, is the "end-to-end" distance of this coiled up random walk. This should give an idea of the space the polymer chain takes up. As a consequence of each step in our model being random and independent, however, the average end to end distance is clearly zero. A more appropriate measure of chain size is the *root mean square (r.m.s) end to end distance*, R_{rms}.

We can derive an expression for this length by representing each monomer as a vector in a random walk. Summing these vectors over the entire chain then gives us an end to end vector, $\mathbf{r}$, as shown in Figure 2.1.
The derivation for R_{rms} then follows as:

$$\mathbf{r} = \sum_{i=1}^{n} \mathbf{a_i}$$

$$\mathbf{r}.\mathbf{r} = r^2 = \sum_{i=1}^{n} \mathbf{a_i}.\mathbf{a_i} + \sum_{i \neq j} \mathbf{a_i}.\mathbf{a_j}$$

$$r^2 = Na^2 + a^2 \sum_{i \neq j} \cos\theta_{ij}$$

where $\cos\theta_{ij}$ is the angle subtended by $\mathbf{a_i}$ and $\mathbf{a_j}$. We can simplify this by substituting,

$$\sum_{i \neq j} \cos\theta_{ij} = N\langle\cos\theta\rangle$$

where $\langle\cos\theta\rangle$ is the average value of $\cos\theta_{ij}$ along the chain. In this simple model, the monomers can point in any direction so we can calculate $\langle\cos\theta\rangle$ by assuming that each direction is equally likely and taking the average

value of a continuous function as so,

$$\begin{aligned}\langle \cos\theta \rangle &= \frac{\int_0^{2\pi} \cos\theta \mathrm{d}\theta}{2\pi - 0} \\ &= \frac{1}{2\pi}[\sin\theta]_0^{2\pi} = 0\end{aligned}$$

So for our ideal chain, $\langle \cos\theta \rangle = 0$, and it follows that,

$$r^2 = Na^2$$

and the r.m.s end to end distance is,

$$R_{\mathrm{rms}} = r = aN^{\frac{1}{2}} \tag{2.2}$$

Using this, one can estimate the size of typical polymer chains in a polymer melt (a polymer liquid above its glass or crystallisation temperature). Using polystyrene as an example, we know that the molecular weight of a styrene monomer is 104 Da and each monomer in the chain has a length $a \approx 0.2$ nm. This means that for a typical chain of $M_w = 1000$ kDa: $R_{\mathrm{contour}} \simeq 2$ μm, $R_{\mathrm{rms}} \simeq 20$ nm.

It is useful to know the distribution of possible end to end chain lengths as well as an r.m.s. value as this will allow us to obtain the configurational entropy of the chain as well. If we calculate the number of possible combinations for a given end to end distance, R, we can write down the distribution function as so [3],

$$\Omega_R = Ae^{-\frac{3R^2}{2Na^2}} \tag{2.3}$$

where Ω_R is a statistical weight and A is a normalisation constant. A full derivation of this formula is contained in Appendix A.

This distribution has a Gaussian form. An example for a small polymer chain is plotted in Figure 2.2. As expected, the width of the distribution scales to the r.m.s. size of the polymer chain ($\sigma = a\sqrt{N/3} = R_{\mathrm{rms}}/\sqrt{3}$ to be precise). As this distribution gives us the number of available configurations

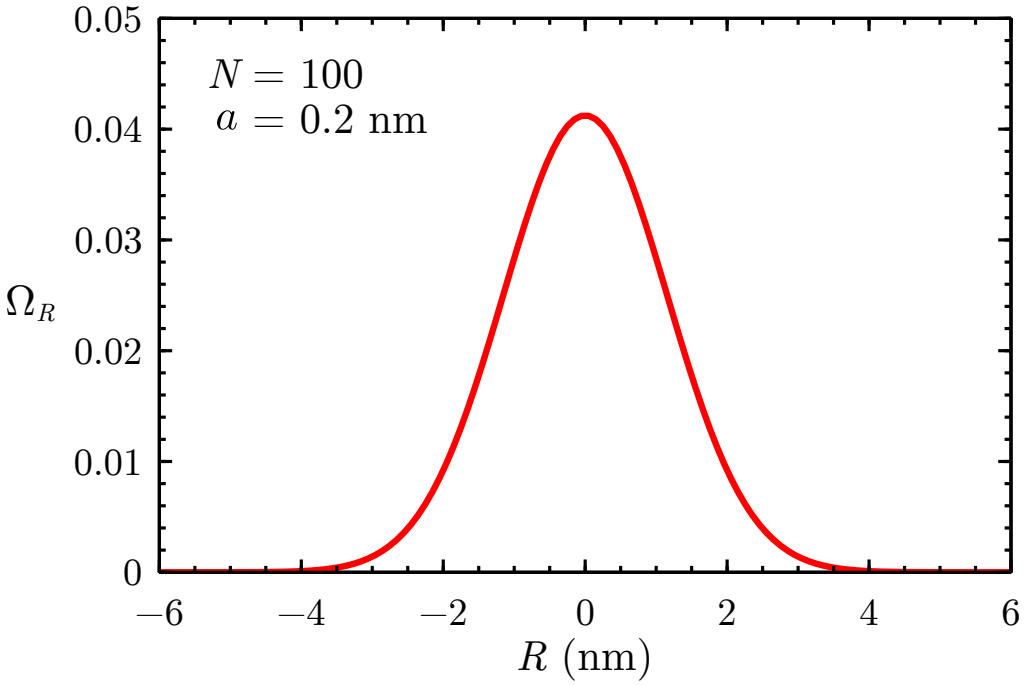

Figure 2.2: The distribution of end to end distances for an ideal random walk. It has a Gaussian form centred on $R = 0$ and the width scales with the size of the polymer chain.

of the chain we are able to use it to calculate the entropy of the chain using the Boltzmann form:

$$S = k_B \ln \Omega_R \tag{2.4}$$

where k_B is the Boltzmann constant.

With this, we are now in a position to write down the free energy, G, of an ideal polymer chain. In general, the free energy can be written as:

$$G = H - TS \tag{2.5}$$

where H is the enthalpy of the chain, T is the absolute temperature and S is the entropy. As enthalpic interactions between monomers in a melt are only weakly dependent on the end to end distance, we can simplify and write the free energy in terms of only the entropic contribution:

$$G = -TS \tag{2.6}$$

Using the Boltzmann form of the entropy (Eqn. 2.4) and distribution function for our ideal chain (Eqn. 2.3) we can write an expression for the free energy in terms of the end to end distance of the chain, the chain dimensions and temperature:

$$G = -k_B T \ln A + k_B T \frac{3R^2}{2Na^2} \tag{2.7}$$

This will be useful in the next section when we consider the elastic properties of polymers.

Real polymer chains

It is obvious that for real polymers, the ideal chain model is not entirely adequate. There are a number of issues related to the physical structure of a polymer molecule that it does not take in to account.

The first of these is that, for a real chain, the orientation of it's monomers is not independent of its neighbours. Chemically, we know that the bonds between monomers cannot simply take a random orientation or rotate freely. There are definite bond angles and hence there are correlations between neighbouring monomers.

These correlations, however, are only short ranged when compared with the length of the polymer chain. This can be seen simply when one considers that the correlation between two neighbouring monomers is:

$$\mathbf{a_i}.\mathbf{a_{i+1}} = a^2 \cos\theta$$

In general then, the correlation between two monomers that are an arbitrary number of links, m, apart is:

$$\mathbf{a_i}.\mathbf{a_{i+m}} = a^2 \cos^m \theta$$

The cosine function is always less than 1 so as m increases, the correlations become smaller. That is, as two monomers are further apart on the chain,

the correlation between them becomes negligible. This allows the chain to be split up in to 'blobs', or subunits, that are longer than the length of the correlations.

On this longer length scale, one might expect the chain to behave like a random walk once more but for an isolated chain this is not the case due to the second key feature of real polymer chains that is not accounted for in the ideal chain model: that the monomers have a finite volume. This means that they cannot intersect with each other and as such cannot form an ideal random walk. Instead, they must take a self-avoiding path.

This is called the excluded volume effect and introduces a repulsive term in to the free energy equation for the chain. To obtain this term, we assume the monomers behave like gas molecules in a fixed volume and calculate the difference in the entropy between the ideal case and the non-ideal, excluded volume case.

We assume the polymer molecule is confined to a volume, $V \sim R^3$, and write down the expression for the entropy of an ideal gas in this case [13]:

$$S_{\text{ideal}} = \frac{N}{2} k_B \ln\left(\frac{V}{N}\right) \tag{2.8}$$

Now, when we exclude the volume of the monomers, our total available volume becomes $V - Na^3$ and so,

$$\begin{aligned} S_{\text{non-ideal}} &= \frac{N}{2} k_B \ln\left(\frac{V - Na^3}{N}\right) \\ &= \frac{N}{2} k_B \ln\left(\frac{V}{N}\left(1 - \frac{Na^3}{V}\right)\right) \\ &= \frac{N}{2} k_B \left[\ln\left(\frac{V}{N}\right) + \ln\left(1 - \frac{Na^3}{V}\right)\right] \\ &= S_{\text{ideal}} + \frac{N}{2} k_B \ln\left(1 - \frac{Na^3}{V}\right) \end{aligned} \tag{2.9}$$

If we remember that $\ln 1 + x \approx x$ when $x \ll 1$, then we can simplify this expression in the case where the volume of the monomers is small compared

to the total volume, i.e. $\frac{Na^3}{V} \ll 1$:

$$S_{\text{non-ideal}} = S_{\text{ideal}} - \frac{N^2}{2} k_B \frac{a^3}{V} \tag{2.10}$$

So, the effect of the excluded volume correction is to add an extra entropic term to the free energy:

$$G_{\text{excl. vol.}} = -ST = +k_B T \frac{N^2 a^3}{2R^3} \tag{2.11}$$

Adding Eqn. 2.11 to the free energy expression for an ideal chain, Eqn. 2.7, we obtain the free energy for a real chain as a self-avoiding random walk:

$$G = -k_B T \left(\ln A - \frac{3R^2}{2Na^2} - \frac{N^2 a^3}{2R^3} \right) \tag{2.12}$$

It should be noted again that this is for an isolated chain. In a polymer melt for example, the neighbouring chains effectively screen the excluded volume effect and random walk statistics are recovered [3].

Before we move on to discussing how elasticity arises in polymers, it is worth quickly describing the nature of polymers in the form of a glass, as this state reoccurs throughout the experiments contained in this work.

Glassy polymers

There are a wide range of glass forming materials that are encountered in everyday life. On obvious example are the oxide glasses that make our windows. Most polymers can also form glasses. Examples such as poly(methyl methacrylate) (PMMA), often sold as Perspex, are common in the world around us.

Perhaps the best way to think about glasses as a state of a matter is that they are like liquids that do not flow. They share the lack of long range ordering common to liquids but as they are kinetically arrested they behave like a solid, with an effectively infinite viscosity and a finite shear modulus.

A key concept needed to understand glasses is that of the *relaxation time*. There are many different types of relaxation in condensed matter, for example a structural relaxation of a polymer chain. One specific relaxation case is useful to our understanding here. If one imagines a liquid, then each molecule can be though of as being surrounded by a 'cage' of it's neighbours. For a molecule to move to a new position, it takes a certain amount of time for it to overcome the interactions with its neighbours. This is the *alpha* relaxation time, τ.

If one attempts to deform the liquid on a timescale less than τ then the molecules are not able to rearrange or flow and as such can't release the applied stress. This means they behave as a solid with equivalent elastic properties.

This is true even of simple liquids such as water but we don't observe this behaviour often as their relaxation times are of the order of 10^{-13}-10^{-11} seconds [3]. These are clearly much shorter than the timescales on which we typically deform water. Polymeric liquids, however, may have relaxation times of the order of 1 second and so appear glassy much more frequently.

The relaxation time of a liquid is dependant on temperature. As the temperature of a liquid is lowered the relaxation time increases. At some point this becomes comparable to the time of the experiment and the liquid effectively can't flow - it has become a glass. The temperature at which this occurs is commonly labelled T_g, the glass transition temperature.

The physics of the glass transition has been studied for 60 years but there is still no complete theory that explains all its features. Models such as the Adam-Gibbs model [14], which considers the way a molecules' neighbours would have to move cooperatively for it to take a new position, describe some aspects of the transition but discussion of them is beyond the needs of this work.

Practically, one can determine T_g experimentally, for example by performing calorimetry and watching for a discontinuity in the heat capacity of the material as it is cooled [15]. It should be noted though, that as T_g is dependent on the time of the experiment, different cooling rates will produce a different T_g.

Different polymers display a range of glass transition temperatures but many lie in easily reachable ranges. Polystyrene, for example, has a T_g of 95° [16]. This is a very useful property as it means they can easily be processed and moulded in to a variety of shapes by heating them above their T_g and forming the desired structure before quickly fixing this structure in place by quenching the sample so it returns to a glassy state.

Now that some of the key physics describing polymer molecules has been covered, it is appropriate to consider the elasticity of polymers and how this arises.

2.2 Elastic properties

The topic of this thesis is a series of experiments that probe the elastic and acoustic properties of polymers at the nanoscale. It is useful, therefore, to investigate how elasticity arises in polymers.

The elastic modulus of polymers

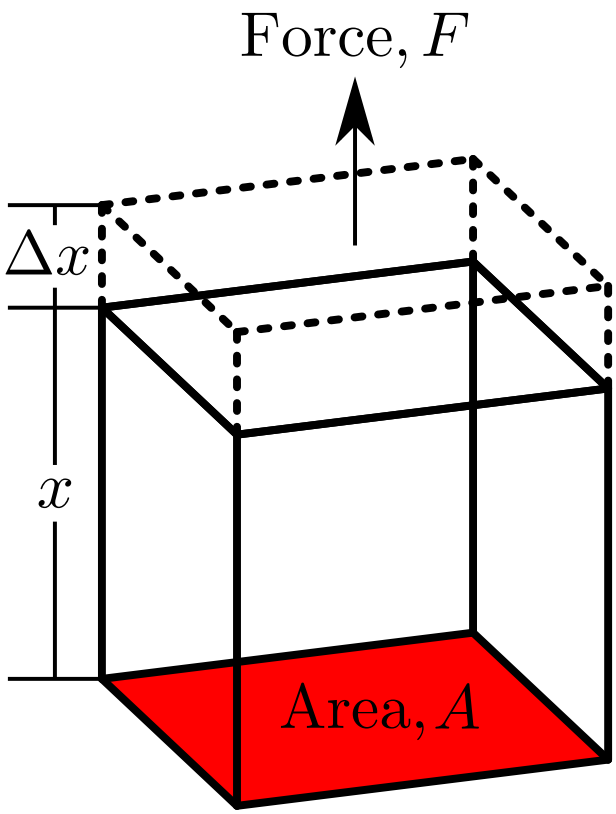

Figure 2.3: This diagram shows a one dimensional strain resulting from a stress on a material. The stress is a force, F, applied on an area area, A, that results in an extension of Δx to the initial length of the material, x.

In very general terms, when a stress is applied to an elastic material, it results in a strain. The constant of proportionality between these two is the Elastic Modulus, E. This is often referred to as the Young's Modulus, named after the 19th century English polymath, Thomas Young.

To define E properly, consider Figure 2.3 which shows an example of a one dimensional strain. We define stress as the force per unit area:

$$\sigma = \frac{F}{A}$$

The strain is defined:

$$\epsilon = \frac{\Delta x}{x}$$

The Young's modulus is then defined as:

$$E = \frac{\sigma}{\epsilon} \tag{2.13}$$

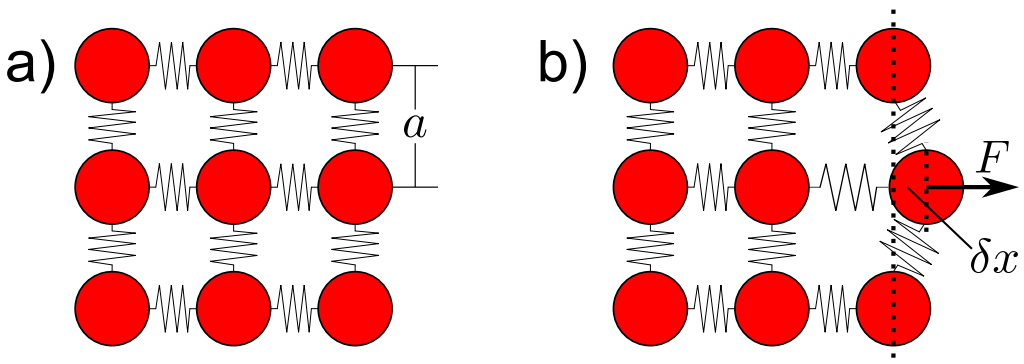

Figure 2.4: a) An example Hookean solid. The molecules of the solid (red dots) sit in an interatomic potential due to their nearest neighbours (represented by black springs). They have a an equilibrium separation of a. b) A force, F, causes a small displacement δx in one of the molecules.

We can calculate the Young's modulus from first principles to find its general form. First, we consider a Hookean solid like that shown in Figure 2.4a. We assume that each molecule sits in an interatomic potential, $U(r)$, due to it's interactions with its nearest neighbours. The equilibrium separation of the molecules is a.

If a force, F is applied to a molecule, it results in a small displacement, δx, as shown in Figure 2.4b. We can then expand the interatomic potential

using a Taylor series around the equilibrium separation:

$$U(a+\delta x) = U(a) + \delta x \left.\frac{\mathrm{d}U}{\mathrm{d}r}\right|_{r=a} + \frac{1}{2}\delta x^2 \left.\frac{\mathrm{d}^2U}{\mathrm{d}r^2}\right|_{r=a} + \ldots \tag{2.14}$$

At equilibrium, however, the net force on an atom is zero:

$$F(a) = -\left.\frac{\mathrm{d}U}{\mathrm{d}r}\right|_{r=a} = 0$$

So Eqn. 2.14 becomes:

$$U(a+\delta x) = U(a) + \frac{1}{2}\delta x^2 \left.\frac{\mathrm{d}^2U}{\mathrm{d}r^2}\right|_{r=a} + \ldots \tag{2.15}$$

We can write Eqn. 2.15 in the form:

$$U(a+\delta x) = U(a) + \frac{1}{2}k\delta x^2 + \ldots \tag{2.16}$$

where,

$$k = \left.\frac{\mathrm{d}^2U}{\mathrm{d}r^2}\right|_{r=a} \tag{2.17}$$

is a spring constant.

Returning to our definitions of stress, strain and the Young's modulus:

$$\begin{aligned} \sigma = \frac{F}{A} = E\epsilon = E\frac{\delta x}{a} \\ F = \frac{EA}{a}\delta x \end{aligned} \tag{2.18}$$

Eqn. 2.18 has the form of Hooke's law with a spring constant:

$$k = \frac{EA}{a} \tag{2.19}$$

Remembering that the area per atom is $A = a$ we can now equate our spring constant equations 2.17 and 2.19 and rearrange for E. This gives us a general expression for the Young's modulus:

$$E = \frac{1}{a}\left.\frac{\mathrm{d}^2U}{\mathrm{d}r^2}\right|_{r=a} \tag{2.20}$$

It is worth noting that the Young's modulus has units of Pa, which is equivalent to Jm^{-3}. This means it can be viewed as a measure of the bond energy density of a material. For a low Young's modulus, this equates to weak bonds, or relatively few of them: the material will be soft and malleable. Conversely, a high bond energy density or Young's modulus means the material will be rigid. Polymers typically have a Young's modulus of a few GPa, although this can be highly temperature dependant.

In a polymer sample, the Young's modulus has contributions from intermolecular forces (i.e. Van der Waals interactions) but an intramolecular contribution related to elastic deformation of the polymer chain. As E is related to the bond energy density, we can calculate the elastic modulus of an ideal polymer chain using Eqn. 2.20 where the potential, U, is the expression for the free energy of an ideal polymer chain, Eqn. 2.12.

$$E = \frac{1}{a} \left. \frac{\mathrm{d}^2 G}{\mathrm{d}r^2} \right|_{r=a}$$
$$E = \frac{3k_b T}{Na^3} \tag{2.21}$$

This means that the polymer chain behaves like a spring but interestingly, the restoring force is entropic in origin. As the polymer chain is stretched out the number of possible conformations decreases resulting in an unfavourable decrease in entropy. The polymer opposes this by generating a restoring force.

The Young's modulus of polymer chains also has an unusual temperature dependence in that as temperature increase, so does the value of E. This is in contrast to most materials, where increasing the temperature makes them easier to deform.

It should be noted, that for a glassy polymer, where the molecules are coiled up randomly in a kinetically arrested structure, the stretching of individual chains is minimal although bonds are free to rotate slightly [17]. The main contribution to E for glassy polymers comes from the

intermolecular Van der Waals interactions and the "cage" like dynamics of this state, rather than the intramolecular 'entropy spring' action described immediately above.

The relation to acoustic properties

If one imagines an acoustic pulse propagating through a material, it can be thought of as a travelling deformation. Clearly then, the nature of its propagation is likely to be strongly dependant on the elastic properties of the medium. In this context, two useful acoustic properties to define are the *speed of sound* and the *acoustic impedance*.

The longitudinal speed of sound, c, can be written in terms of the density, ρ, Poisson ratio, ν, and Young's modulus, E of a material as [18]:

$$c = \sqrt{\frac{E(1-\nu)}{\rho(1+\nu)(1-2\nu)}} \tag{2.22}$$

For polymers, speeds tend to be of the order of 2000-3000 ms^{-1}.

The acoustic impedance, Z, is a measure of a medium's resistance to the propagation of sound. It is analogous to the electrical impedance of an electrical circuit component. More formally, it is defined as the amount of acoustic pressure that is generated by a given acoustic volume flow rate.

We can define it simply in terms of the density of a material and the speed of sound in that material:

$$Z = \rho c \tag{2.23}$$

The acoustic impedance is a very useful property when describing sound. If one imagines a sound wave travelling through air and hitting a brick wall, it will mostly be reflected. This can be described in terms of the sound propagating through a medium with relatively low Z (the air) and hitting a medium with much higher Z (the wall).

Similarly, if one wanted to design a system made from many different materials, but wanted to minimise internal reflections of sound waves, they could attempt to match the impedances of each material.

We now move on to discuss the key experimental techniques used in the work carried out for this thesis.

3. Experimental Techniques

This chapter covers the most commonly used techniques for the work in this thesis. First, the spin coating technique which was used to prepare all of the ultra-thin polymer films. Second, ellipsometry; this optical technique is a way of characterising the films once they are made. In particular, it was used for most of the thickness measurements of the films.

Then, the picosecond acoustic technique that was used to generate the high frequency acoustic pulses in Chapters 4 & 5 is briefly introduced. Finally, the Langmuir-Blodgett trough that was used for the measurements in 6 is covered.

3.1 Spin coating

Spin coating is an ubiquitous polymer processing technique. It can be used to reproducibly create uniform polymer films with low ($\sim$ 1nm) roughness over a wide range of thicknesses. The main steps in the process are outlined in Figure 3.1. In brief, to create a film this way, a droplet of polymer solution is placed on a substrate that is then rotated rapidly.

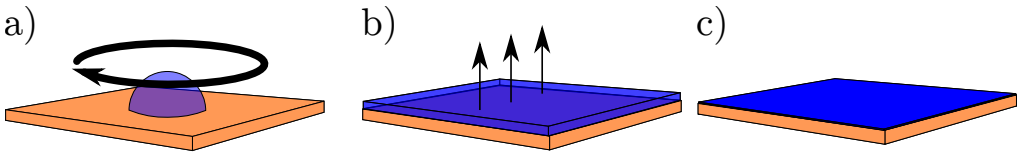

Figure 3.1: This diagram shows the spin coating process. A droplet of polymer solution is placed on the substrate which is spun rapidly (a). As it spins, the droplet spreads out and the solvent starts to evaporate (b). At a certain point, enough of the solvent has evaporated that the polymers aren't able to rearrange and the final film is formed (c).

The desired polymer is first dissolved in a good solvent, normally to concentrations of the order of a percent by weight. This solution is then

placed on the desired substrate and spun at a few thousand rpm. Excess solution flies off the edge forming a solvent swollen film on the substrate. At this point, the polymers can still flow and rearrange but as the solvent evaporates their structure is locked in and the result is a flat, thin film.

A variety of factors effect the thickness of the film produced. The two most important are the concentration of the polymer solution and the spin speed. Figures 3.2 and 3.3 contain plots showing the typical thickness dependence on these two factors.

Other factors that can affect the thickness of the films include the molecular weight, M_w, of the polymer, the initial acceleration of the spin phase and the solvent evaporation rate, which is itself of product of not only the volatility of the solvent but also atmospheric conditions.

After spin coating, the samples are often thermally annealed. Typically this is at a temperature above the glass transition of the polymers, allowing them to relax and flow. This step ensures that any remaining solvent from the spin coating is evaporated but also allows the polymer chains to relax structurally, removing any unfavourable conformations that may have been locked in during the rapid initial removal of the solvent.

The main advantage of spin coating is its relative simplicity when compared with other methods, such as thermal processing, which often requires vacuum or specialist apparatus in addition to precise temperature control. It is also a very fast process with the high spin speeds causing the film to dry quickly. Although it is somewhat wasteful, with the majority of the polymer solution being lost while spinning, it is the most commonly used technique for preparing thin polymer films for research.

The spin coating process was used to produce all of the samples studied in this thesis. The technique used to measure the thickness of the films in almost every case was ellipsometry, and it is this that will be discussed next.

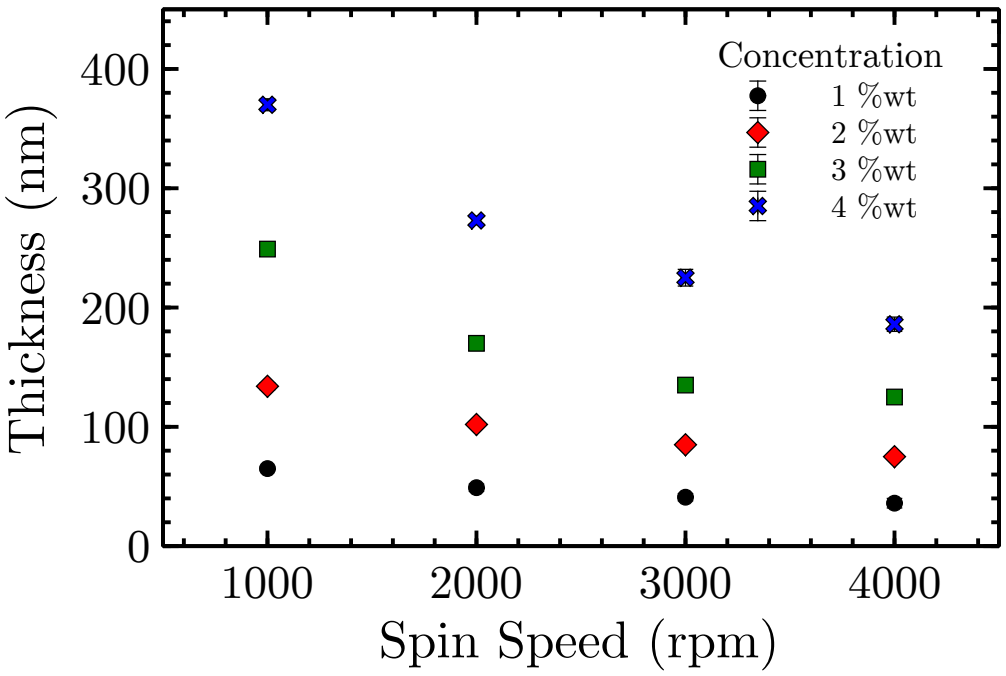

Figure 3.2: This plot shows the dependence of spin coated film thickness versus the spin speed, for a variety of solution concentrations. The data was collected for polystyrene (192 kDa) films on silicon substrates and the solvent used was toluene. The errors are of the order of a few nanometres so are barely visible on the plot.

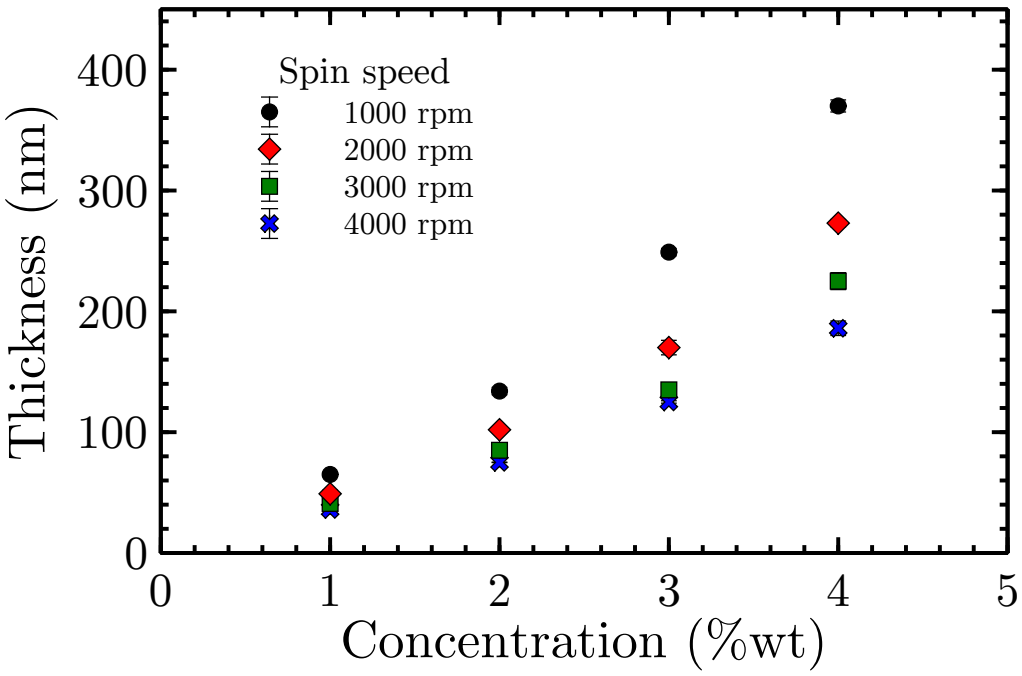

Figure 3.3: This plot shows the dependence of spin coated film thickness versus the concentration of the solution used, for a variety of spin speeds. The data was collected for polystyrene (192 kDa) films on silicon substrates and the solvent used was toluene. The errors are of the order of a few nanometres so are barely visible on the plot.

3.2 Ellipsometry

Ellipsometry is an optical technique for investigating the properties of thin films. It can be used to probe both the dielectric properties of films, but also physical properties such as the film's composition and roughness. In particular, for the work contained in this thesis, it was used as the main method of measuring films thicknesses.

It is an extremely sensitive technique that can measure film thicknesses to an accuracy of a few angstroms. This is remarkable as it is typically much less than the wavelength of light used to make the measurement. Instead, ellipsometry relies on modelling changes in the polarisation of light as it reflects off a film. An advantage of using polarised light is that it means the technique is less sensitive to ambient light conditions so doesn't require the dark room conditions of other optical techniques.

There are many different possible set-ups for ellipsometry but they can essentially be broken in to two separate groups: single wavelength and spectroscopic. Single wavelength ellipsometry uses a laser with a well defined wavelength to probe the sample. This is suitable for measuring film thicknesses and some dielectric properties. Spectroscopic ellipsometry uses a broad band light source and can be used to obtain the full complex refractive index of the film at a range of wavelengths.

The ellipsometry performed to measure film thicknesses in this thesis used a custom built, single wavelength nulling ellipsometry set-up. A schematic of this is shown in Figure 3.4. It consists of a HeNe laser ($\lambda = 633$nm), two rotatable (i.e. free to rotate about the optical axis) linear polarisers, a quarter wave plate and a photodiode. The two linear polarisers are called the polariser and analyser and their angles of polarisation with respect to the optical axis are labelled P and A respectively.

To understand how the ellipsometer works, we can follow the path of

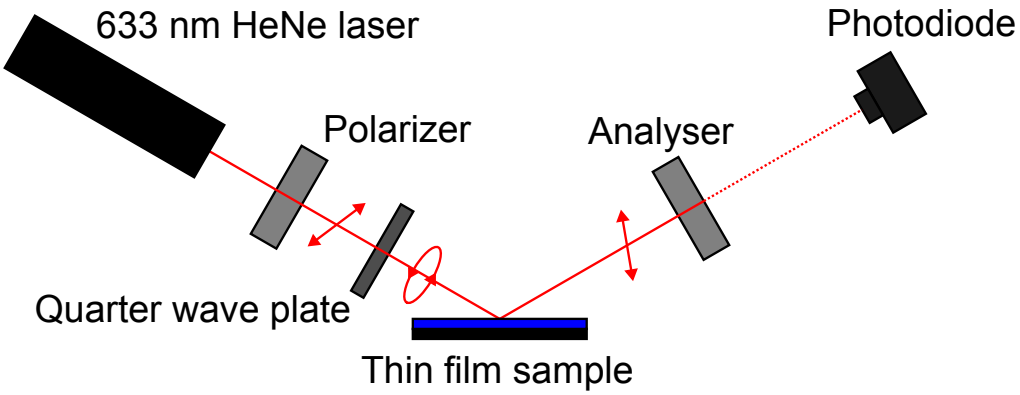

Figure 3.4: A schematic of the ellipsometry set up used for film thickness measurements. Light leaves the laser and passes through a rotatable linear polariser then a quarter wave plate before hitting the sample. The reflected light passes through another rotatable linear polariser (the analyser) and is collected by a photodiode. Also marked is the desired polarisation of the light for the null condition to be a achieved (no light reaching the diode).

the light through it. First, light leaves the laser with some elliptical polarisation. For linearly polarised lasers this can be achieved by adding a quarter wave plate immediately after it. It is then linearly polarised to some angle P by the Polariser and then passes through a fixed quarter wave plate. When linearly polarized light travels through a quarter wave plate it becomes elliptically polarised (or circular if the axis of polarisation is at 45° to the fast axis of the quarter wave plate). This light then hits the sample at a fixed angle of incidence.

In general, when linearly polarized light hits a surface, the reflection is elliptical. Conversely, for some precise elliptical polarisation, the reflected light will be linearly polarised. To achieve this, the polariser angle, P, is changed while the quarter wave plate angle is fixed.

This condition that is tested by the second linear polariser (the analyser). If the light reflected off the sample is linearly polarised, there will be some analyser angle, A at which no light will be transmitted to the photodiode. This is the desired experimental result, also known as the null

condition.

For a fixed quarter wave plate and angle of incidence, the angles of P and A that produce the null condition are unique within a single quadrant ($0 \leq P, A \leq 90°$). Using these values, the film thickness can be calculated. This, however, is not a straightforward process.

For characterising film thicknesses for the work in this thesis a simple sample structure was used. This typically was the polymer film spun cast on an oxide coated silicon substrate. Even for this simple case though, it is not possible to directly determine the film thickness using only two measured parameters (P and A). Not only does the refractive index and thickness of the film matter, but the refractive index of the silicon substrate as well as the refractive index and thickness of the oxide layer will affect the way the way the light reflects.

To be able to pull out useful information from the technique then, we need to rely on modelling what we expect P and A to be for a given situation. We can do this via an optical transfer matrix method. Using estimated, known or measured values for the refractive indices and thickness of each material (including the polymer), each medium, m, in the sample can be represented with a 2x2 transmission matrix, T_m, as so:

$$T_m = \begin{pmatrix} e^{i2\pi nd\cos\theta/\lambda} & 0 \\ 0 & e^{-i2\pi nd\cos\theta/\lambda} \end{pmatrix} \tag{3.1}$$

where n is the refractive index of the layer, d is the layer thickness and θ is the angle of incidence.

For the boundaries, the Fresnel reflection and transmission coefficients, r and t, can be calculated. These are different for each polarisation. Using these we can represent an interface between two materials with a 2x2 boundary matrix as so:

$$B_{1,2} = \begin{pmatrix} 1/t_{12} & r_{12}/t_{12} \\ r_{12}/t_{12} & 1/t_{12} \end{pmatrix} \tag{3.2}$$

where the '12' subscripts represent the light travelling from a material 1 in to a material 2.

By multiplying each boundary matrix (B) and transmission matrix (T) in turn, we generate a 2x2 matrix, M that describes the optical properties of the sample as a whole. For a single polymer film on an oxidised silicon substrate, for example:

$$M_{\text{total}} = B_{\text{air/polymer}} T_{\text{polymer}} B_{\text{polymer/oxide}} T_{\text{oxide}} B_{\text{oxide/silicon}} \tag{3.3}$$

This matrix, M, is calculated for each polarisation and from these, reflection coefficients for each of the s and p polarisations, r_s and r_p, can be extracted. This allows us to write the complex reflectance ratio, ρ of the system:

$$\rho = \frac{r_p}{r_s} \tag{3.4}$$

This can be parametrised using an amplitude component, Ψ, and the phase difference, Δ as so:

$$\rho = \tan \Psi e^{i\Delta} \tag{3.5}$$

The angles P and A are then related to Ψ and Δ as so:

$$P = \frac{\Delta}{2} - 45^\circ \tag{3.6}$$

$$A = \Psi \tag{3.7}$$

assuming the quarter wave plate is at -45° to the optical axis. More information on modelling the ellipsometry angles this way can be found in [19].

In practice, the refractive index of the silicon and oxide layers as well as the oxide thickness are well known and can be measured without a polymer film present. For the polymers used in the work here, the refractive indices are well known also. By fixing all these values in the model, the only free parameter is the thickness of the polymer film.

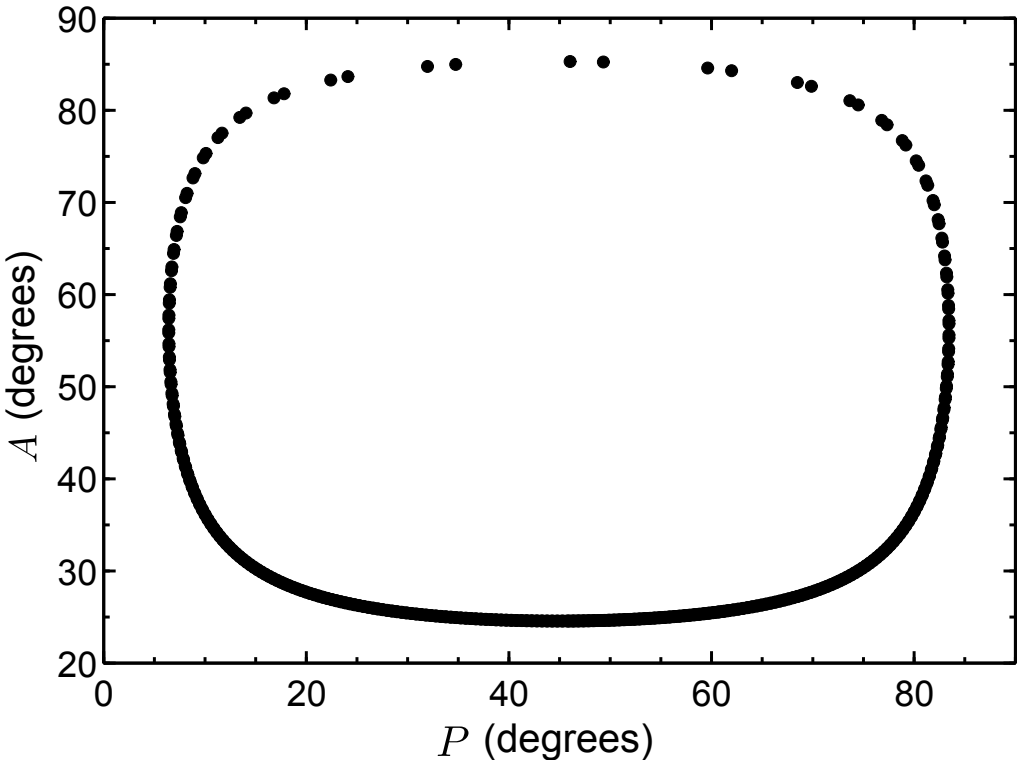

Figure 3.5: A plot showing a typical example of modelled P vs A values for a polymer film on an oxide covered silicon substrate. The values shown here are for a PS film with thicknesses between 0 and 500 nm and a refractive index of $n_{\mathrm{PS}} = 1.595$, on a silicon substrate ($n_{\mathrm{Si}} = 3.74$ -0.019i) with a 2 nm oxide layer ($n_{\mathrm{oxide}} = 1.46$), for light of wavelength $\lambda = 633$ nm incident at $\theta = 58°$.

In this case, we can generate a series of P and A values, stepping through different polymer film thicknesses. The results of one such calculation are shown in Figure 3.5. Once these values have been calculated, the measured P and A values can be matched up and the corresponding thickness of the film can be extracted.

Measuring film thicknesses this way is relatively quick and very accurate, with errors typically less than a nanometre. It does rely on being able to prepare flat, homogeneous films as the high sensitivity of the technique means that any variations in film thickness or excessive roughness in the sample can cause large deviations in the measured angles, or prevent the null condition being achieved at all.

3.3 Picosecond acoustic technique

The picosecond acoustic technique is an optical pump probe technique used for investigating thin films and nanostructures. First developed in the 1980's by Christian Thomsen and Humphrey Maris [20, 21], it uses ultra-short laser pulses to generate elastic strain pulses. It is this technique that forms the basis of the measurements performed to determine the elastic properties of the polymer structures discussed in Chapters 4 and 5. There are many different experimental set-ups to perform the technique, a schematic of the one relevant to this work is shown in Figure 3.6.

In brief, the technique proceeds as so: An ultra-short, high energy laser pulse, called the pump pulse, is focused either directly onto the sample or onto a transducer film (normally metal) attached to it. This high energy pulse results in a local thermal expansion that generates a strain pulse in the sample structure. The strain pulse is detected by a complementary laser probe pulse that is delayed relative to the pump. The optical reflectance or refractive index in the sample changes as the strain pulse propagates and this causes a change in intensity in the reflected probe pulse. By varying the delay time between pump and probe, the time dependant oscillations of the sample in response to the strain pulse can be investigated.

Due to the short laser pulse length, the strain pulse created in the transducer has a broad acoustic spectrum with frequencies up to hundreds of GHz. It is this that is the main advantage of the picosecond technique in comparison with other ways of producing strain pulses, for example via a piezoelectric transducer.

As a technique it is normally applied to hard materials and structures but it has been shown that polymer films can support coherent acoustic pulses as well [22]. The acoustic pulse propagates through the substrate and polymer sample with the speed of longitudinal sound and can, in practice,

be described either as a Gaussian displacement pulse or as the first derivative of this, a strain pulse. The precise shape of the pulse is considered in more detail in Chapter 5.

The experimental set-up used for the measurements in this thesis was a custom built system belonging to Prof. Anthony Kent at the University of Nottingham. The optical arrangement used to create the pump and probe beams is shown in Figure 3.7. The polymer samples were typically mounted on 50 μm thick single crystalline silicon substrates. To act as a transducer, aluminium films approximately 50 nm thick were evaporated on to the back of the substrates. The pump and probe pulses were 60 fs in length, produced by a Ti-Sapphire laser with a repetition rate of 5 kHz.

The pump and probe beams were aligned on opposite sides of the sample. The probe pulse was delayed in arriving at the sample relative to the pump beam, as it travelled a longer path around the optical bench. The precise length of this delay was controlled by routing the pump beam via a stepper mirror. By moving this mirror back and forth, the probe beam could measure the response of the sample at different points after the arrival of the pump beam thus allowing the collection of a time resolved signal of the period when the strain pulse was in the polymer structures. The range of this mirror set the maximum time window that could be be sampled. These were typically 2 ns in length, with a temporal resolution of 1000 fs.

The changes in the intensity of the reflected probe beam as the strain pulse distorted the polymer structures were relatively small. To detect them, a balance photodiode was used, with a reference beam taken from the probe beam before it hit the sample via a partial mirror. This signal was then amplified via a lock-in, triggered with a repetition rate of 2.5 kHz using a mechanical chopper locked to the 5 kHz pump beam frequency.

Further information related to the specific measurements that were made are contained in Chapters 4 and 5.

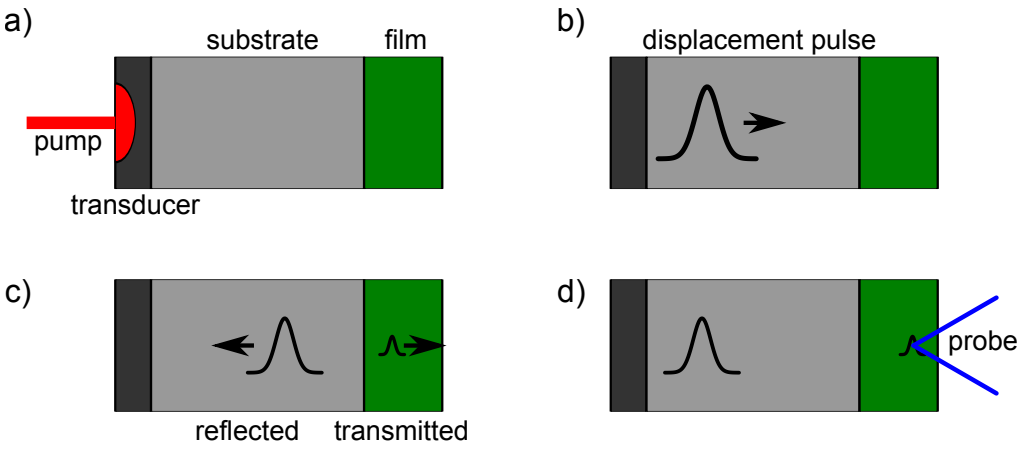

Figure 3.6: A schematic of the picosecond acoustic process used for the work in Chapters 4 and 5. From a) to d): the strain pulse is created by thermal expansion in the transducer, is injected into the substrate, is partially reflected from the substrate/sample interface, and finally, is detected in the transparent, polymer sample via the probe pulse.

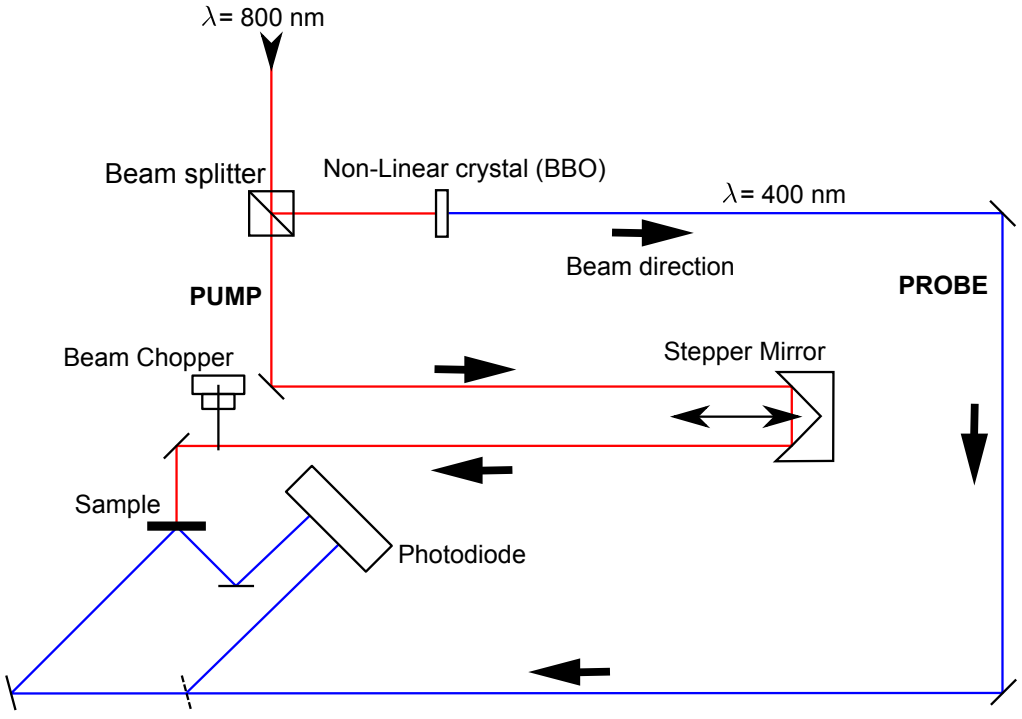

Figure 3.7: A schematic diagram showing the optical set-up. The initial beam is split into two paths, the pump and the probe. The probe beam has it's wavelength halved and then is reflected off the film/load side of the sample to a balance photodiode. The pump beam is directed to the reverse of the sample via a stepper mirror. By moving this mirror, the delay between the arrival of pump and probe beams can be controlled.

3.4 Langmuir-Blodgett trough

Langmuir-Blodgett (or LB) troughs are laboratory systems that are designed to compress molecular monolayers on the surface of some liquid subphase, normally water. They are often used to deposit these monolayers on to substrates that are dipped in to the trough. More generally, they can be used to measure properties such as the surface tension of the layers under compression.

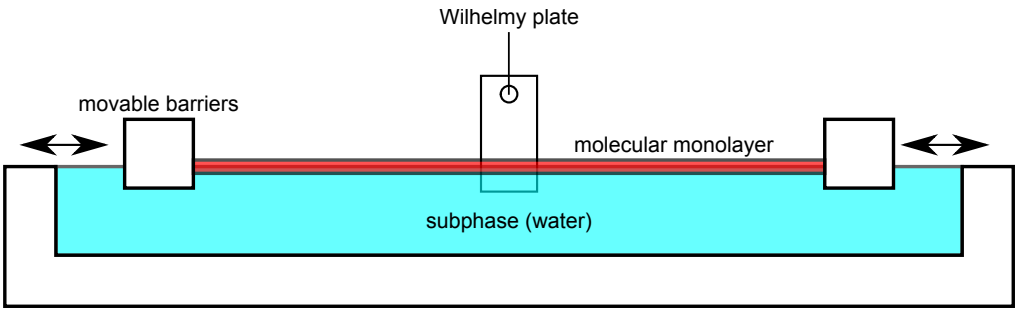

Figure 3.8: A schematic showing a typical LB trough set-up. The barriers move, controlling the compression, or concentration of the molecular monolayer and subsequently the surface pressure as measured by the Wilhelmy plate. Other configurations exist, for example having one barrier and a fixed wall. Other features can include sample dippers, cameras etc.

A schematic of a typical LB arrangement is shown in 3.8. It includes a trough to hold the liquid subphase, on which the monolayer sits. This is deposited by adding a few drops of a dilute solution of the desired molecule to the trough. This effect relies on the molecule in question having both hydrophilic and hydrophobic ends, meaning that it will preferentially sit at the water/air interface. The concentration of the monolayer is controlled via movable barriers. There are many possible configurations of this barrier arrangement and often toughs have other equipment such as sample dippers added as well. The surface pressure or tension are often measured by means of a Wilhelmy plate.

A Wilhelmy plate consists of a small plate which is often made of material such as filter paper, although other types exist. This plate is attached to a force transducer. As the plate is dipped in to the trough, the surface tension of the monolayer, or subphase (if the monolayer is not present), pulls down on the plate as it is wetted. This pull is measured by the force transducer and a surface tension calculated via the Wilhelmy equation:

$$\gamma = \frac{F}{l \cos \theta} \tag{3.8}$$

where γ is the surface tension, F is the capillary force on the plate, l is the wetted perimeter of the plate and θ is the contact angle between the plate and the liquid. θ is often assumed to be $0°$, equivalent to perfect wetting.

It is possible to self-build LB trough systems, however, many commercial solutions exist. For the experiments in this thesis, a trough produced by KSV-Nima was used. Further details of this system and the modifications made can be found in Chapter 6.

4. Quantised vibrations in loaded films

4.1 Introduction

The development of gigahertz (GHz) and terahertz (THz) acoustic devices is a challenging task which promises new and attractive applications [7] [8] . A wide class of potential acoustic devices is based on nanostructures where the acoustic phonon spectrum is quantized. Typical examples of such nanostructures are nanomechanical cantilevers, beams, strings and free standing membranes where the frequency of quantized phonons detected experimentally reaches hundreds of GHz [23]. The most promising applications for devices utilizing quantized phonons are nanosensing [9] [10], optical cooling [11] [12], phonon lasing [24], and quantum information processing [25].

The nanostructures used in these previous experiments were usually fabricated from crystalline materials (e.g. silicon). Soft materials, like polymers, are used more rarely because of the comparatively higher phonon damping that occurs in these materials [26]. Recent experiments, however, with thin polymer films and multilayers have shown that phonon quantization is still very pronounced for frequencies up to a few tens of GHz [27].

Polymeric nanostructures have a number of advantages when compared with crystalline materials. They do not need to be free-standing and can be supported by solid substrates; phonon quantization is still likely to occur because of the large acoustic mismatch that exists between the polymer and the substrate. Polymers may be easily fabricated into films with nanometre dimensions using techniques such as spin-coating or melt processing and ad-

ditional further patterning of polymer surfaces is also possible using nano-imprint lithography based approaches [28]. Block copolymer materials also provide a rich variety of architectures that can facilitate the manufacture of interesting nano-structures with well defined shapes and sizes [29].

The ability to create and manipulate nanometre scale structures is the driving force behind many advances in modern technology and engineering, in diverse fields such as medicine [30] and electronics [31]. Concurrently, there is a growing need to develop methods of measuring characteristics such as the mass, volume and the chemical composition of objects with sizes comparable to the dimensions of individual molecules. The development of new sensing principles for various physical and chemical characteristics has always been a priority in material science research. Of particular relevance is the need to detect the adsorption of small amounts of material that is adsorbed or deposited at interfaces. There are a number of physical phenomena which can form the basis of the function of such nano-sensors [32–34]. The most common of these are sensors that use acoustic resonators that operate in the MHz and GHz frequency range [35].

These micro-mechanical resonators are already widely used as mass sensors in many diverse fields of science and technology because of their ability to detect small amounts of deposited material. These small changes of mass are detected by measuring shifts in the resonant frequency, f_0, of the resonator as material is deposited on the surface. The current industry standard is the quartz crystal micro-balance (QCM) which uses a quartz crystal as the resonator [36]. Here, the change in resonant frequency, Δf_0, is proportional to f_0^2 as described by the well known Sauerbrey equation,

$$\Delta f_0 = -\frac{2f_0^2}{A\sqrt{\rho_q \mu_q}}\Delta m, \tag{4.1}$$

where:

Δm - change in mass

A - piezoelectrically active crystal area

ρ_q - density of quartz

μ_q - shear modulus of quartz

This is derived by treating the film as an extension of the thickness of the underlying quartz and is valid when the relative change in frequency is small and the mass is coupled strongly to the oscillations of the crystal. Conventional QCMs work in the low (typically 10–20) MHz regime, however, systems working with frequencies as high as 170 MHz exist with mass sensitivities in the range of pg/(cm^{2}Hz), allowing mass changes as small as $\sim$0.2 ng/cm^2 to be detected [37]. These values assume that the deposited load consists of a complete, uniform layer, and as such, they correspond to effective thicknesses of material of less than an atomic monolayer.

Beyond this, acoustic waves can also provide additional information about the material deposited on the surface of the resonator. The QCM-D technique, for example, considers the energy dissipation of the waves by recording their decay, as well as their frequencies [38, 39]. This acoustic information can be combined with other types of resonances (e.g. surface plasmon resonance), that provide an independent thickness measurement, allowing studies of the size, shape and binding properties of biomolecules such as DNA, phospholipids and a wide variety of proteins [38–40].

An obvious goal in the development of new sensors of this kind is to increase the sensitivity to deposited mass, to achieve something close to single molecule detection. For acoustic resonator based sensors, the most straightforward way to achieve this is to increase f_0. This can be achieved by using structures that have nanometre scale dimensions, for example, nano-mechanical and nano-electromechanical resonators (e.g. a vibrating cantilever in an electrical oscillatory circuit) [9, 10, 41]. The frequency may also be increased significantly by the excitation of higher frequency vi-

brational modes (harmonics). In free-standing silicon membranes, modes corresponding to a frequency as high as $f_n = 300$ GHz ($n = 15$), have been excited [23].

A further goal is to obtain additional information about the properties of the material that is deposited on the surface of the sensor. This can include information about chemical composition, adhesion and visco-elastic properties, as well as details about any chemical reactions that take place between the sensor and the adsorbed material. For instance, the mechanical properties of certain polymeric systems may change via the manipulation of a bond that can undergo reversible breaking and reformation in response to various external stimuli, such as changes in temperature and pH or UV irradiation [42, 43].

In order to realize these goals, one might think of using a sensor with a mass comparable to that of the object under investigation, such as the structure studied in this chapter: an ultra-thin ($\sim$100 nm) polymer film supported on a silicon substrate.

As mentioned above, the ease of processing polymers makes them ideal candidates for forming nanostructures. Moreover, it may also be desirable to have resonator surfaces that will be sensitive to the presence or absence of particular adsorbed materials, for example enzymes or organic pollutants [44]. In this respect, polymer films are excellent candidates for use as surface sensitive materials due to the wide range of available surface chemistries [44].

The aim of the work presented in this chapter is to demonstrate the changes to the hypersonic quantized phonon spectrum when a polymer film is loaded with a mass of another material. These experiments are an important demonstration of the potential for using ultra-thin polymer films as mechanical resonators for hypersonic nanosensing applications. It is shown that as well as being able to detect adsorbed mass, the polymer films

have the potential to provide information about changes in the elastic and mechanical properties of the adsorbed material under certain conditions. Specifically, the results are analysed using two models: the first considers simply loading the polymer film with some mass; and the second includes the elastic coupling of the adsorbed material with the polymer film.

4.2 Method

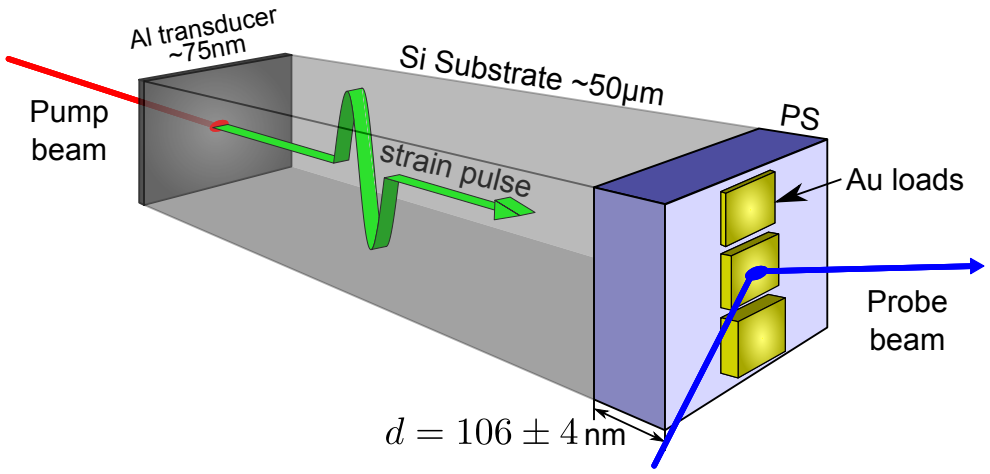

Figure 4.1: A schematic diagram showing the experimental set-up. The pump beam hits the aluminium transducer causing a thermo-elastic expansion that results in a strain pulse being injected into the silicon substrate. This strain pulse propagates through the silicon and into the polystyrene film and load (if present), where it is measured via the change in intensity of a reflected probe beam

Aluminium (Al) films with a thickness of 75 nm were deposited on the surface of 50 μm thick single crystal silicon (Si) substrates. Polystyrene (PS) (Sigma Aldrich, M_w= 192 kDa) films were spin coated on to the opposite surface of the Si substrates from 2%wt solutions in toluene. A drop of solution was placed on each substrate and rotated at 2000 rpm. This procedure resulted in the production of uniform polymer films with thickness values of 106 $\pm$ 4 nm. The thickness of each film was measured using a home built single wavelength ($\lambda = 633$ nm) self-nulling ellipsometer. Areas, typically measuring 3 mm by 2 mm, of high purity gold were then deposited on the PS coated surface of the sample using thermal evaporation at a pressure of 1x10^{-5} torr. The thickness of the gold layers was measured using a quartz crystal resonator that was placed close to the samples in the evaporation chamber. Gold layer thickness values in the range 2.5–30 $\pm$

0.5 nm were obtained.

The hypersonic experiments were performed at room temperature using a picosecond acoustic technique. The corresponding experimental scheme is shown in Figure 4.1. The Al film was excited by 60 fs optical (pump) pulses ($\lambda = 800$ nm), with a repetition rate of 5 kHz using an amplified Ti-sapphire laser. The pump beam was focused to a 200 micrometer diameter spot which resulted in the maximum energy density on the Al film being $\sim$10 mJ/cm^2. When the Al film is optically excited in this way it expands thermo-elastically and a bipolar strain pulse with a duration of $\sim$10 ps is injected into the neighbouring Si substrate. The strain pulse propagates through the Si with the velocity of longitudinal polarized (LA) sound (8430 m/s) and reaches the Si/PS interface in a time of $\sim$6 ns. The strain pulse is then partially reflected due to the acoustic mismatch between PS and Si and partially transmitted into the polymer film. This results in a hypersonic wavepacket of coherent of longitudinal (LA) phonons being excited in the PS film.

The acoustic wavepacket in the PS film was detected by measuring the change in the intensity of an optical probe pulse ($\lambda = 400$ nm) as a function of its delay, t, relative to the pump pulse. This delay time was controlled by routing the pump beam via a moveable delay line. A schematic of the complete optical set-up can be found in Figure 3.7. Simply, the initial beam is split into two paths, the pump and the probe. The probe beam has it's wavelength halved by passing it through a non-linear crystal and then is reflected off the film/load side of the sample and on to a balance photodiode. The pump beam is directed to the reverse of the sample via a stepper mirror. By moving this mirror, the delay between the arrival of pump and probe beams can be controlled.

The changes, ΔI(t), in the intensity of the reflected probe beam from the Au-loaded polymer film could be detected due to the very precise align-

ment and focusing of the probe beam on to the photodiode. Even a small change in the position of the surface of the sample, such as that caused by the acoustic pulse is sufficient to change the position of the spot on the photodiode, thus changing the measured intensity. These changes were monitored using a balance photodiode and a lock in amplifier, triggered with a repetition rate of 2.5 kHz using a mechanical chopper locked to the 5 kHz pump beam frequency. For each different Au thickness, 5 measurements were taken, each at a different point on the deposited area. The measurement positions were chosen to be away from the edges of the areas so as to avoid any edge effects. The results presented in Figure 4.2 are the average of these measurements with associated error bars. No significant differences were observed in the shapes of the temporal signals when the excitation pump and probe beam power densities were varied

4.3 Results

Samples of the measured intensity signals, ΔI(t), are shown in Figure 4.2(a) for each Au thickness value. The changes in the reflectance start at t = 0, which corresponds to the arrival of strain pulse at the free surface of the sample. The signals have a complicated oscillatory behaviour which is reproducible at all points on the surface for each Au load layer. No significant differences were observed in the shapes of these temporal signals when the excitation pump and probe beam power densities were varied. General features, such as the period of the oscillations, the decay time and the amplitude of ΔI(t) in the plain (unloaded) PS film (see the upper curve in Figure 4.2(a)), were similar to those detected in earlier work on PS films [27]. It can clearly be seen that the signals change significantly when the thickness of the Au load increases. More specifically, for thick Au films the period of the slower oscillations increases and the high-frequency features are smeared out.

Figure 4.2(b) shows fast Fourier transforms, obtained in 2 ns time windows, of the corresponding ΔI(t) data shown in Figure 4.2(a). Two distinct resonant peaks, marked by solid arrows, can easily be seen in the spectra. These peaks correspond to the quantized LA vibrations in the hybrid PS/Au film. The large acoustic mismatch between the PS and Si substrate means that the excited acoustic modes (i.e. phonons) cannot escape easily from the film. In plain PS films, such confinement results in quantization that has an analog with closed-pipe organ modes with frequencies of [27]:

$$f_n = \frac{(2n+1)s}{4d}, \tag{4.2}$$

where: n is an integer, s is the longitudinal (LA) speed of sound in the polymer and d is the thickness of the polymer film.

The two peaks in the spectrum for the plain (uncoated) PS film (upper curve in Figure 4.2(b)) correspond to the modes with frequencies f_0 and

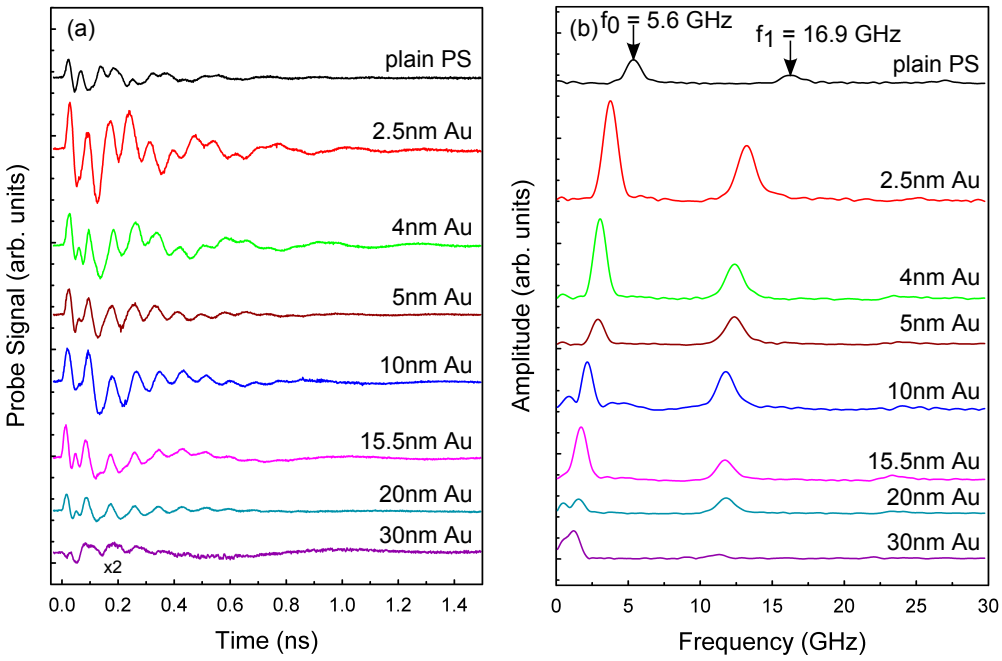

Figure 4.2: (a) Representative examples of temporal changes in the reflectivity of the probe beam, ΔI(t), measured using 400 nm, femtosecond laser pulses at the surface of unloaded and Au loaded polystyrene films; (b) Amplitude fast Fourier transform spectra obtained from the corresponding temporal traces shown in (a). The vertical arrows indicate the frequencies f_0 and f_1 of the fundamental and first quantized resonances respectively.

f_1 related to n = 0 and n = 1 respectively given by the above equation. For Au loaded PS films, equation 4.2 is no longer valid, and the values of f_n change: the positions of the peaks shift, corresponding to a decrease in the quantised frequencies with the increase of the Au load thickness. The magnitude of the changes in f_0 and f_1 following the deposition of Au layers lie in the GHz frequency range and f_0 for the highest load (30 nm Au film) decreases by a factor of 3.

4.4 Theory

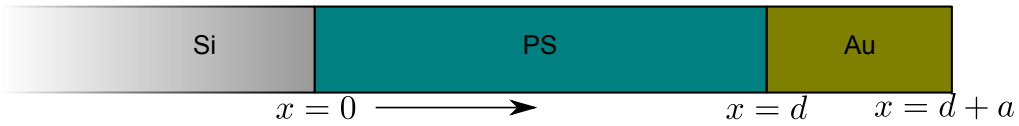

Figure 4.3: A schematic showing the 1D sample structure considered. A semi-infinite silicon substrate ($x < 0$) is coated by a PS film of thickness d ($0 \leq x \leq d$). The gold load, thickness a, is deposited on the top surface of the PS film.

The aim of the analysis is to calculate resonant frequencies for longitudinal elastic standing waves in the polymer/load structure. These waves are described by the displacement, $u(x,t)$, of atoms in the structure perpendicular to its surface. The elastic equation describing this is:

$$\rho_m \frac{d^2u_m(x,t)}{dt^2} - c_{11}^m \frac{d^2u_m(x,t)}{dx^2} = 0, \tag{4.3}$$

where: ρ_m is the bulk density of layer m and c_{11}^m is the elastic constant of layer m.

This has solutions of the form:

$$u_m(x,t) = e^{i\omega t}(A_m e^{i\omega x/s_m} + B_m e^{-i\omega x/s_m}), \tag{4.4}$$

where: ω is the angular frequency ($\omega = 2\pi f$), $s_m = \sqrt{c_{11}^m/\rho_m}$ is the LA sound velocity in each layer and A_m and B_m are arbitrary amplitudes.

As is the case for the unloaded PS films studied in a previous work [27], the Si substrate can be considered semi-infinite and the film can be considered to be effectively pinned ($u(0,t) = 0$) at this interface. Any influence on the measured oscillations due to acoustic pulses returning after reflection through the substrate can be discounted, as the transit time is expected to be ~12 ns. This is much larger than the 2 ns decay time observed for oscillations in the polymer/load structure. A more complicated analysis, where the boundary condition at the Si/PS interface was treated similarly

to the PS/Au interface was also performed. This was done by introducing two new constants relating to the amplitude of the wave in the silicon and introducing new boundary conditions of the same form as the PS/Au interface. This more complex system could still be solved using a linear algebraic method, however, as can be seen in Figure 4.4, this predicted phonon frequencies that were identical to those expected in the case of a pinned Si/PS interface.

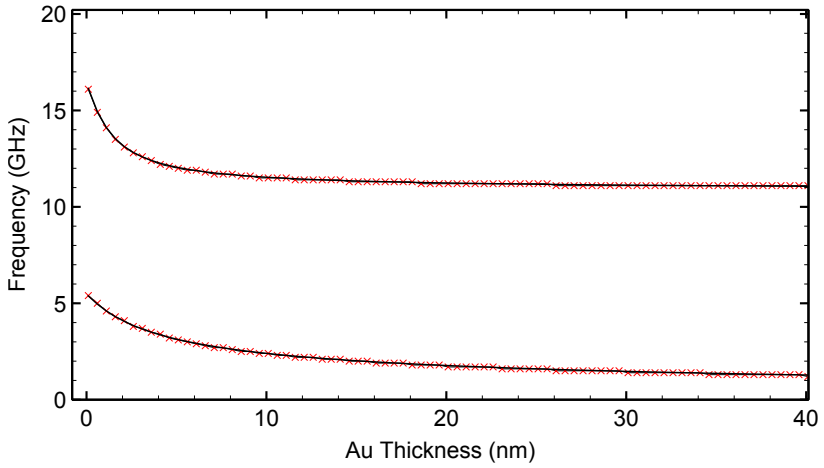

Figure 4.4: This plot shows a comparison between the calculated frequency modes using both a pinned PS/Si interface (black lines) and where it was free to move (red crosses). It can be seen that these are identical to within the precision of the calculation for the film structure presented here (PS thickness = 106 nm).

At the PS/load interface, two cases each described by a different boundary condition are considered. In the first case, which shall be called the "load" model, it is assumed that no elastic waves are excited in the load which has a mass per unit area, σ_{load}. The extreme case of this situation is when the load behaves as a solid mass that follows the displacement of the top surface of the polymer film. Then, the stress in the film at the film-load interface ($x = d$) is equal to the force per unit area exerted by the load. As such, the boundary condition at the interface may be written

as:

$$c_{11}^{\mathrm{PS}} \left.\frac{du_{\mathrm{PS}}}{dx}\right|_{x=d} = \sigma_{\mathrm{load}} \left.\frac{d^2u_{\mathrm{PS}}}{dt^2}\right|_{x=d} \quad . \tag{4.5}$$

Using this and the pinning condition at the Si/PS interface, the solution to equation 4.3 becomes:

$$\tan\left(\frac{\omega_n d}{s_{\mathrm{PS}}}\right)\omega_n\sigma_{\mathrm{load}} = Z_{\mathrm{PS}} \quad , \tag{4.6}$$

where: $Z_m = s_m\rho_m$ - the acoustic impedance of layer, m. The frequencies of the eigenmodes in this case, $f_n = \omega_n/2\pi$, may be found numerically using a simple Newton-Raphson method [45].

The second case, referred to as the "elastic" model, is when the elastic wave extends into the bulk of the load. Then the boundary conditions at $x = d$ are obtained by matching the displacement and stress in the film and load and can be written in the form:

$$u_{\mathrm{PS}}(d,t) = u_{\mathrm{load}}(d,t), \tag{4.7a}$$

$$c_{11}^{\mathrm{PS}} \left.\frac{du_{\mathrm{PS}}}{dx}\right|_{x=d} = c_{11}^{\mathrm{load}} \left.\frac{du_{\mathrm{load}}}{dx}\right|_{x=d} \quad . \tag{4.7b}$$

The boundary condition at the load/air interface is that of zero strain, $\left.\frac{du_{\mathrm{load}}}{dx}\right|_{x=d+a} = 0$ (see Figure 4.3). Using this condition, equations 4.7a, 4.7b and the pinning condition at the Si/PS interface, the solution to equation 4.3 in this case becomes:

$$\tan\left(\frac{\omega_n d}{s_{\mathrm{PS}}}\right)\tan\left(\frac{\omega_n\sigma_{\mathrm{load}}}{Z_{\mathrm{load}}}\right) = \frac{Z_{\mathrm{PS}}}{Z_{\mathrm{load}}} \quad . \tag{4.8}$$

The left hand side of this equation is plotted in Figure 4.5 along with a dotted line representing $Z_{\mathrm{PS}}/Z_{\mathrm{load}}$. It is clear that solutions exist and these can be found numerically.

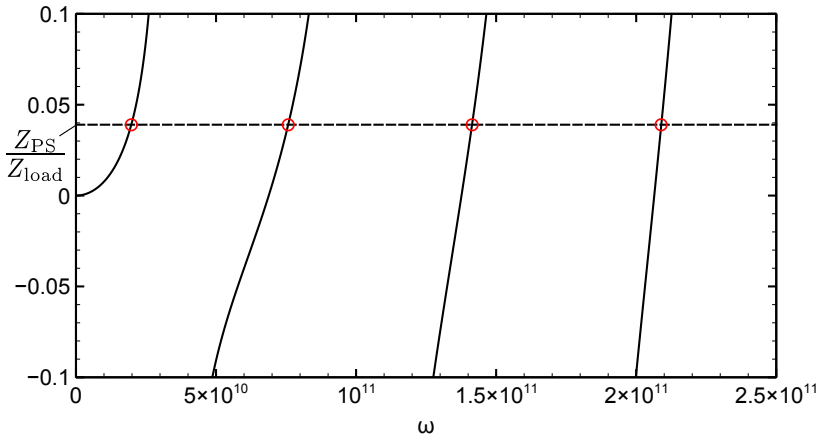

Figure 4.5: This plot shows the left hand side of Equation 4.8 (black lines). It can be seen that solutions to Equation 4.8 exist where the left hand side equals $Z_{\mathrm{PS}}/Z_{\mathrm{load}}$ as expected, these are circled in red. This was calculated for a 106 nm thick PS film and a mass per unit area, σ_{load}, corresponding to a 5 nm layer of gold.

4.5 Discussion

Figure 4.6 shows how the frequencies, f_0 and f_1 depend upon the thickness and mass of the adsorbed gold layers (lower and upper scales respectively). Each point was calculated as the average of 5 repeated measurements for each Au thickness, each taken at a different point on the Au loaded areas. The measured frequency for each Au thickness proved accurately reproducible, as can be seen from the small vertical error bars, representing the standard error. The calculations were performed for both the "load" and "elastic" models using a thickness, $d = 105$ nm (same as the films studied within experimental error) and the following parameters: $s_{\mathrm{PS}} = 2300$ m/s, $s_{\mathrm{load}} = s_{\mathrm{Au}} = 3200$ m/s, $\rho_{\mathrm{PS}} = 1047$ kg/m^3, $\rho_{\mathrm{load}} = \rho_{\mathrm{Au}} = 19300$ kg/m^3.

These values are the same as those expected for bulk PS and Au, and when used in conjunction with equation 4.2, correctly predicted the frequencies measured in the unloaded films. The results of these frequency calculations for each of the two models were almost identical and they are shown in Figure 4.6 as solid lines. The agreement between measured data

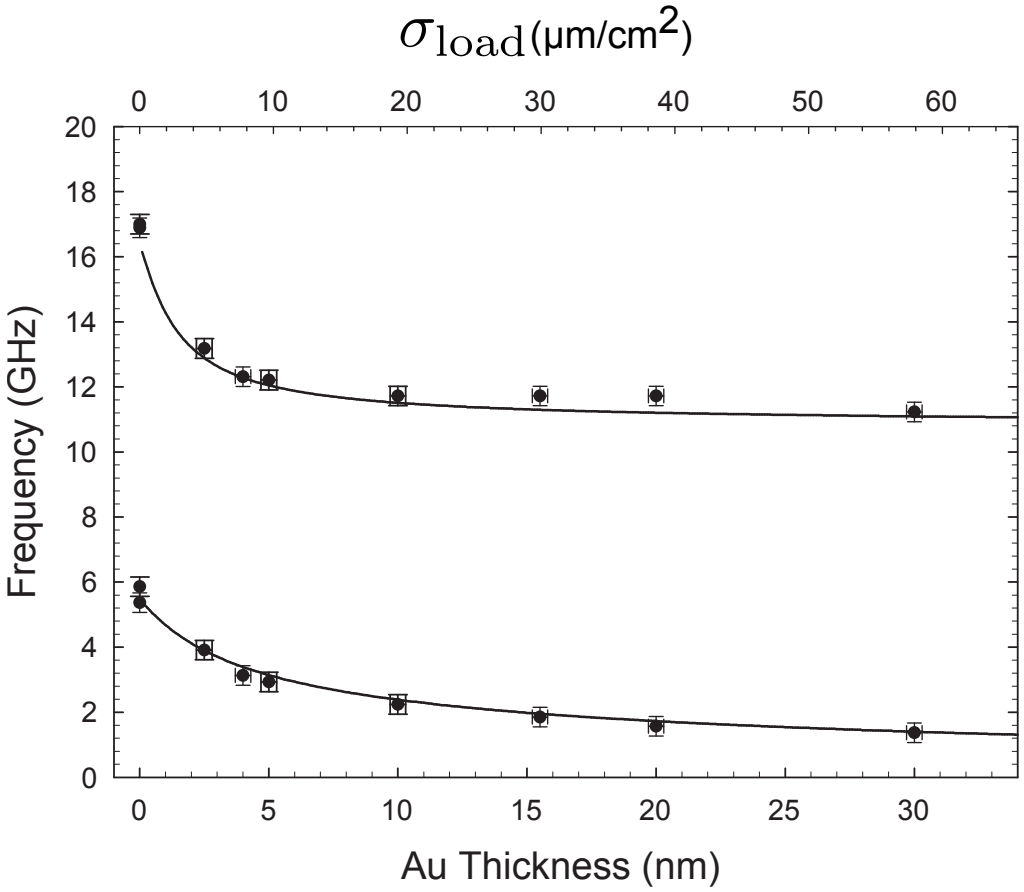

Figure 4.6: The resonant frequency of PS films as a function of the mass/thickness of the deposited Au load. Measured (symbols) and calculated (solid lines) values show how the frequencies of the fundamental and first harmonic of the PS oscillator depend upon the thickness (lower scale) and areal mass density (upper scale) of the Au load. The calculations obtained for the "load" and "elastic" models are the same to within the level of uncertainty.

and the predicted values is excellent.

This plot shows that large relative changes in f_0 and f_1 take place when the Au load is only a few nanometres thick. Further increases in thickness, up to 30 nm, show a tendency to cause saturation of the frequency shifts. The appearance of a strong non-linearity of the frequency dependence on the thickness/areal mass density of the applied load is to be expected and occurs at load thickness values of $d \sim 1$ nm ($\sigma_{\text{load}} \sim 2\ \mu\text{g/cm}^2$). An obvious explanation for this is that, in this experiment, the ratio of areal densities $\sigma_{\text{load}}/\sigma_{\text{PS}}$ is not a negligibly small value as even a small thickness of gold has a significant mass relative to the polymer films and is therefore likely to strongly influence the frequency of the films' vibration.

If the deposited load is small, then it couples to the oscillations of the resonator , analogous to the Sauerbrey equation (equation 4.1). Under these conditions the load can be assumed to act like a small increase in the mass, or thickness, of the film. The corresponding change in frequency described is obtained by rewriting equation 4.2 in terms of areal mass density rather than a thickness and differentiating. Doing this, the following expression for the change in frequency due to a small change in mass is obtained:

$$\Delta f = \frac{df}{dm}\Delta m = \frac{-4f_n^2}{s_{\text{film}}\rho_{\text{film}}(2n+1)}\frac{\Delta m}{A}, \tag{4.9}$$

where: $\Delta m/A$ is the additional mass per unit area. This provides an estimate of the ultimate frequency sensitivity of the polymer film to deposited mass. For the structure presented here ($f_1 = 16.9$GHz, $s_{\text{PS}} = 2300$ m/s), a mass sensitivity of 650 $\times 10^{-18}$ g/(cm^2 Hz) is obtained. This is 8 orders of magnitude better than current state of the art QCM systems [37].

To find the conditions under which the load and elastic models give essentially different eigenmode frequencies, the calculations were performed for a wide range of load parameters, σ_{load} and Z_{load}. Figure 4.7 shows the dependence of the second quantized frequency, f_1, on the relative load mass

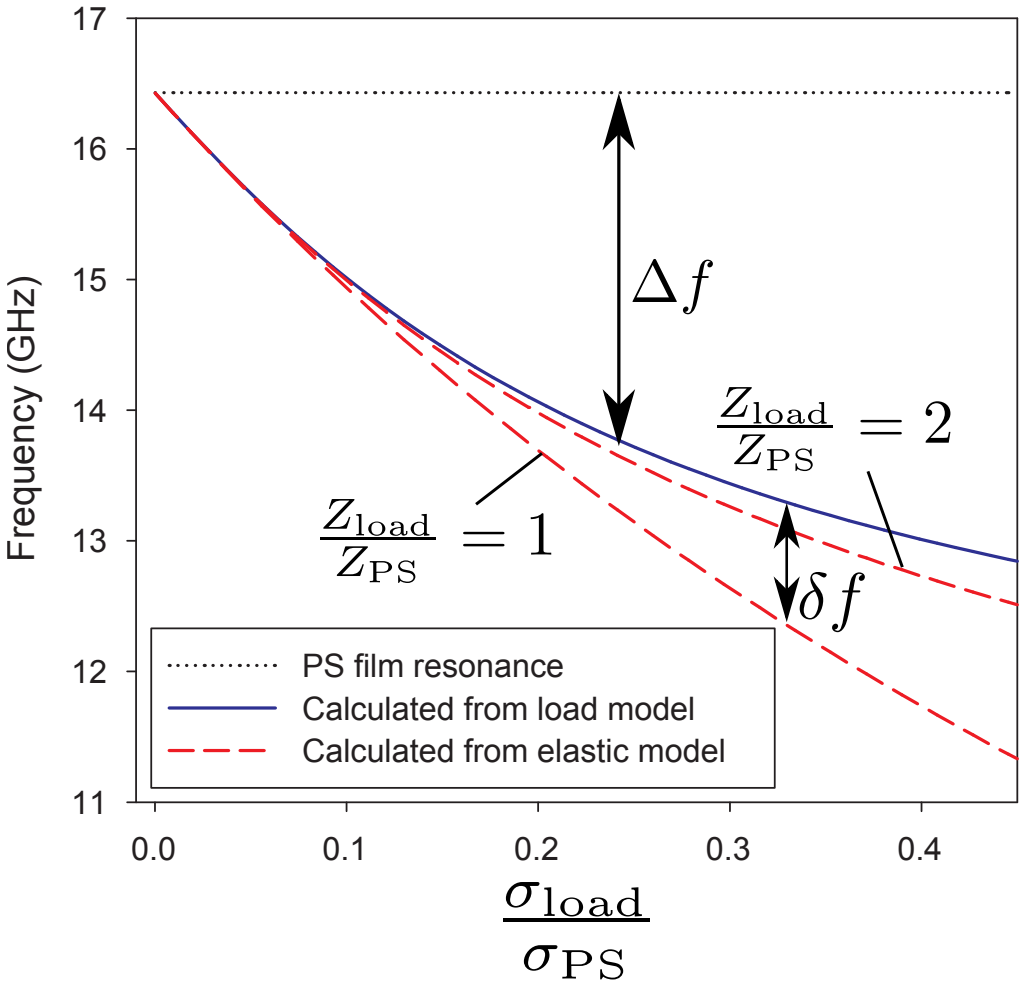

Figure 4.7: Results of calculations of the shift in the first harmonic frequency, f_1, against areal mass density for a 100 nm PS film loaded with material with acoustic impedance Z_{load}. The solid curve is obtained using the load model and two dashed curves correspond to the elastic model for $Z_{\mathrm{load}} = 1$ and 2; (b) a surface plot of the relative difference in frequency as calculated by the load and elastic models as a function of the relative mass and impedance of the load.

for the PS films studied here. The solid curve is the calculated result of the load model (eq. 4.6) and the dashed curves are calculated using the elastic model (eq. 4.8) for two values of load impedance. It is seen that the load model is only valid for low values of σ_{load}. The difference between the predictions of the two models, δf, also increases as Z_{load} decreases.

Figure 4.8 shows a surface plot where the difference between the first quantized frequencies calculated for each model, df, is plotted as a function of σ_{load} and Z_{load}. In the regions where $\frac{df}{\Delta f} \sim 0$, both models give almost identical results. However, there are a wide range of σ_{load} and Z_{load} values where the acoustic properties of the samples studied here will deviate from the simple case described by the load model.

A practical question arises regarding the validity of the load or elastic model in each particular case. From Figures 4.7 and 4.8 it is clear that these two models give identical results when σ_{load} is negligible relative to the mass of the sensor, regardless of the value of Z_{load}. This is commonly the situation that occurs when using a QCM, as the quartz crystals used as oscillators are relatively large. For low mass sensors, such as the ultra-thin polymer film presented here, the ratio $\sigma_{\text{load}}/\sigma_{\text{PS}}$ is not negligible. For even the smallest (2.5 nm thick) Au load studied here, $\sigma_{\text{load}}/\sigma_{\text{PS}} = 0.5$.

It is likely that if probing, for example, organic materials, this ratio would be less, but still far from zero and the question regarding the validity of the load or elastic model in each case becomes increasingly important. In reality, the answer depends on whether the load couples strongly to the oscillations of the PS films. If the coupling is poor, the load model is capable of reproducing the observed frequency shifts. If there is good coupling between the polymer sensor layer and the attached load, then the elastic model becomes more suitable. In this latter case the frequency predictions obtained via the load and elastic models differ significantly if $Z_{\text{load}}/Z_{\text{PS}} < 2$. For the relatively dense Au loads studied here, $Z_{\text{load}}/Z_{\text{PS}} =$

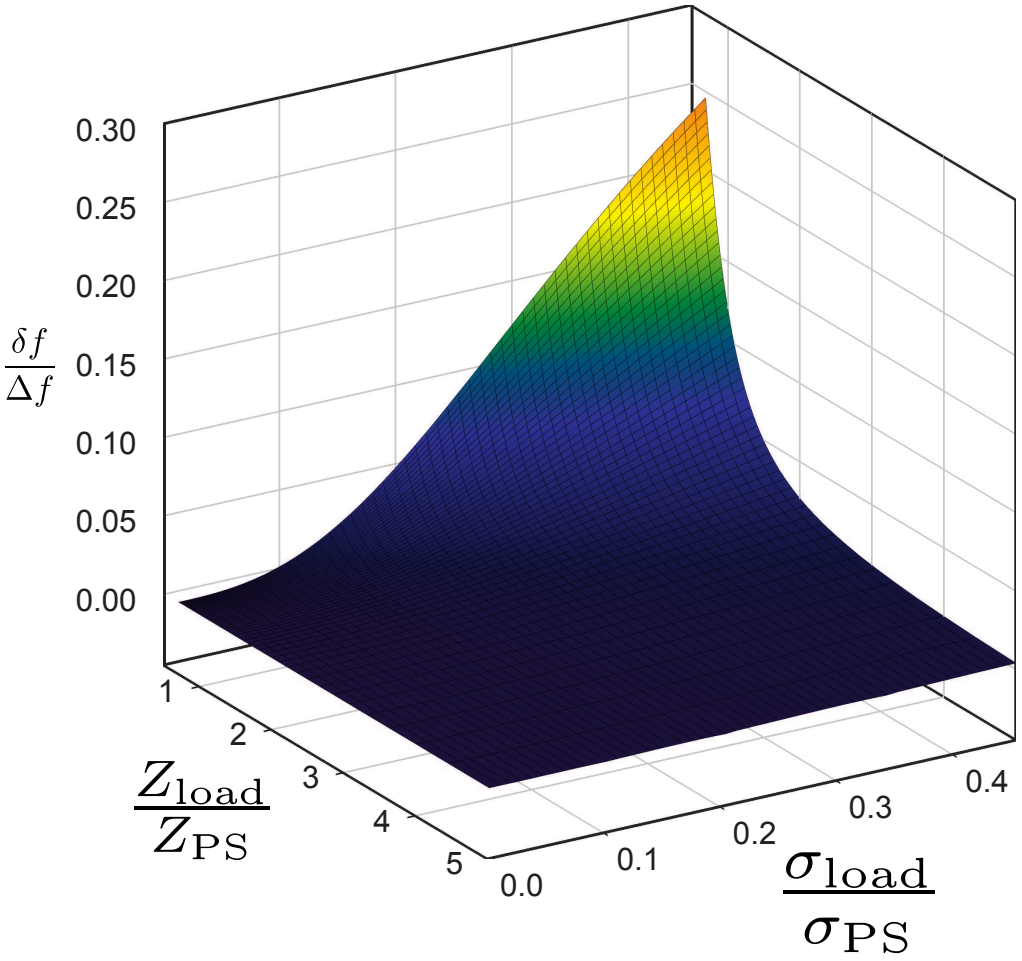

Figure 4.8: A surface plot of the relative difference in frequency as calculated by the load and elastic models as a function of the relative mass and impedance of the load.

26, and consequently the frequency shifts predicted using either model are essentially identical.

The results point to the potential application of polymer films as ultra-sensitive hypersonic sensors for investigating a variety of systems. At low masses ($\leq$ 10 ng/cm^2), the specific sensitivity to changes in mass deposited on the polymer surface is estimated from Figure 4.6 to be about 650 ag/(cm^2 Hz). This is approximately 8 orders of magnitude better than current state-of-the-art quartz crystal microbalance (QCM) systems, due to the higher frequency used. However, the actual mass sensitivity that can be achieved in practice is limited by the precision with which changes in the frequency can be measured.

This depends both on the damping and the signal to noise ratio as well as the resolution of the FFT, which is set by the duration of the signal (or the distance the the delay line can be moved). The damping lowers the Q of the system, and hence leads to broadening of the spectral lines, but if the signal to noise ratio is sufficiently high it is possible to measure the shift of a line which is some fraction of its linewidth, for example by using a peak fit to find the central value of the peak. In the experiment here the frequency resolution is $\sim$100 MHz, which is about 10% of the linewidth. This corresponds to being able to detect areal mass densities of 65 ng/cm^2, which is only one order of magnitude worse than state-of-the-art QCM systems that can resolve a fraction of a Hz at about 10 MHz.

It is possible that the frequency resolution of the experiments reported here could be improved by increasing the signal to noise ratio by, for example, using a higher repetition rate femtosecond oscillator instead of the amplified femtosecond laser (it should be pointed out here that the pump beam from the amplified laser was heavily attenuated, and it would be possible to achieve similar pump power density using a femtosecond oscillator if the spot was focused to $\sim$10 μm). Given that the mass sensitivities are

similar, and the current requirement for an ultrafast laser, it seems unlikely that the polymer based sensor could compete with the, much simpler to operate, QCM sensors except with regard to potentially better spatial resolution to adsorbed mass as the laser spot is small ($\sim$100 μm) compared to typical QCM sensors ($\sim$1 cm^2).

One interesting possibility that would potentially increase the usability of a polymer sensor is if the vibrations could be generated and measured electrically, as is the case with the piezoelectric quartz crystals in a QCM. Piezoelectric polymers exist, polyvinylidene fluoride (PVDF) is a common example, so in theory this could be achieved. Forming ultra-thin, homogeneous films of these polymers is not, however, a trivial task. PVDF for example is a crystalline polymer that does not spin-coat well so alternate processing methods must be considered. If this could be achieved, such a system would have the potential for both relatively easy excitation and detection of vibrations in the GHz regime.

The above comparisons of the polymer device with QCMs, however, assume a vacuum or gas environment. Applications of QCMs in studies of, for example, protein adsorption on surfaces require operation in liquids where strong damping significantly decreases their sensitivity. The advantage of a sensor working at frequencies in the 10s of GHz range is that it will be largely mechanically decoupled from fluids with viscosity comparable to water, and so, in this regime the ultimate sensitivity of a polymer hypersonic mass sensor could be better than QCMs. These measurements could be performed using the current pump-probe technique, for example by building a liquid cell with an optical window for the probe beam.

It is also expected that the mass changes and acoustic impedances of organic materials, such as proteins, will lie in the region where the frequency shift is sensitive to Z_{load}, possibly allowing for additional information regarding the mechanical and elastic properties of the load to be extracted.

These potential advantages of the polymer-based device could be more easily exploited with the use of electrical means of generation and detection of acoustic waves in the 10s of GHz range, for example by using a piezoelectric polymer such as polyvinylidene fluoride (PVDF).

4.6 Conclusion

It has been shown that the frequencies of quantized GHz phonon modes in ultra-thin polymer films are sensitive to adsorbed material. The frequency shifts lie in the GHz range and a decrease in frequency of a factor of 3 is detected for the fundamental mode when loading a $\sim$100 nm polystyrene film with a 10 nm film of gold. The results are analysed using models where the polymer film is coupled or alternatively decoupled elastically to/from the load. The calculations performed suggest that under certain conditions the film is very sensitive, not only to the areal mass density of the load, but to its acoustic impedance as well. These results suggest potential applications for the films as ultra-sensitive hypersonic mass sensors.

5. Acousto-optic effects in Bragg reflectors

5.1 Introduction

The interaction of acoustic and electromagnetic waves in solids has been a topic of intense study since the beginning of 20th century and has resulted in many practical applications, such as acousto-optical modulators, filters and deflectors [46]. During the last decade, the field of acousto-optics has progressed to include studies of nanometre scale objects, aimed at exploiting acoustic waves in nano-photonic and opto-mechanical devices.

Traditional Brillouin scattering experiments have, so far, provided basic information about the acoustic spectra and the strength of acousto-optical interactions in various nano-structures, where both the refractive indices, and the acoustic impedances are periodic in space with periods less than 1 micrometer [47–51]. In addition, acousto-optical effects excited in optical fibres provide the possibility of gigahertz (GHz) light modulation [52–54]. Another rapidly developing field concerns structures which exhibit both optical and acoustic resonances [55–59] and which demonstrate exciting phenomena such as optical cooling [11,12,60] and stimulated sound emission (saser devices) [24, 61] .

The mechanisms governing the interaction of light with high-frequency phonons in photonic nanostructures are still under debate and, as such, are the subject of much of the current research into high-frequency acousto-optics. Generally, the photoelastic effect (i.e. the dependence of the permittivity of a material on strain, induced by an acoustic wave) is considered to be the most important mechanism in transparent bulk solids with

momentum conservation between the acoustic and electromagnetic waves governing various acousto-optical phenomena [62]. In periodic structures, acoustic waves also modulate the positions of the internal interfaces and the size of the domains in the structure. Such dynamic changes, which occur at the frequency of the acoustic wave, modulate the way that light interferes inside the structure. These in turn result in the modulation of the optical properties of the nanostructure as a whole.The interplay between the photoelastic effect and interface modulation determines the final optical output (e.g. reflection, transmission, scattering and the localization of photons) that is induced by acoustic waves in such a nano-photonic device.

For strong interactions to occur between photons and phonons in nano-photonic devices, the wavelengths of the sound and light must be comparable. To produce acousto-optic devices that operate in the visible range of wavelengths requires materials that are structured on the 10-100 nm length scale and which typically have acoustic vibrational frequencies of $\sim$10 GHz.

A particular branch of the current research in this area concerns periodic nano-structures with photonic stop bands (PSBs) [48]. These stop bands occur due to the periodicity of the structure,typically alternating layers of opaque materials with different dielectric properties. As incident light encounters an interface in the structure, it is partially transmitted and partially reflected. If the layers thicknesses are chosen appropriately then these partial reflections will constructively interfere for a given wavelength and angle of incidence. This process then leads to the characteristic stop band in the entire structures' reflectivity.

The periodic nature of such structures means that they can also exhibit phononic stop bands, if the spatial variations in the acoustic properties of the structure occur on length scales comparable to the acoustic wavelength. With careful design, such structures may confine both optical and acoustic waves simultaneously, leading to a significant enhancement of the

interactions between photons and phonons [63] . In practice, however, this situation is hard to achieve as producing structures which possess both complete photonic and phononic stop bands is a technically complex task [64]. Theoretical works in this area are mostly limited to calculations of dispersion relations for various 2D and 3D photonic-phononic crystals [63, 65] , but there are also studies which have tried to calculate the optical output of such nano-photonic devices (e.g. reflectance or transmittance) [64,66].

In the past, significant milestones in high-frequency acousto-optics have been achieved through the study of 1D (i.e. periodic in one dimension) photonic structures. As an example, it has recently been shown that acoustically induced modulations of the optical reflectivity in a high-quality planar micro-cavity increase in strength when the optical wavelength corresponds to the cavity mode [59]. The reported observations suggest realistic prospects for various advanced, high-frequency applications.

The majority of current nano-photonic devices (e.g. lasers, nano-cavities etc.) require distributed Bragg reflectors (DBRs) as elements of the device. DBRs are multi-layered periodic films, that are often classified as 1D photonic crystals. DBRs characteristically possess PSBs and their optical properties have been studied in detail [67]. However, no experimental or theoretical works considering the high-frequency acousto-optical properties of DBRs exist. It is not clear, therefore, whether there is a difference apparent in the acousto-optical interactions inside a DBR when compared to a homogeneous film of the same thickness and mean refractive index. It is clear that this is not trivial, even for the simplest case, when the acoustic dispersion is linear and phononic stop-bands do not exist. It is this issue that has motivated the work in this chapter, in which the acousto-optical effects inside a polymer DBR are studied using picosecond acoustic methods.

The main aims of this work were to characterize coherent photo-elastic

effects in a polymer based DBR where no acoustic mismatch exists between the layers using both experimental and theoretical methods. In this chapter, the results of experiments where picosecond strain pulses were injected into DBR structures are presented. The pulses were monitored as they travelled through the multilayer structure by measuring the temporal evolution of the optical reflectance at a wavelength in the vicinity of the PSB. This is the aforementioned (Section 3.3) picosecond acoustic technique which has been widely used to study the acoustic properties of homogeneous, transparent solid and liquid films [68, 69]. A theoretical analysis is presented and the results obtained from the DBR are compared with homogeneous single films. The experimental results and theoretical analysis show that both the photoelastic effect and the modulation of the interfaces inside the DBR contribute to the reflectance changes and the relative size of these two contributions depends on the wavelength, angle of incidence and polarization of the optical probe beam.

5.2 Theory

In this section , we will consider what happens when a strain pulse travels through a sample in more detail. At first, the simplest case of the signal obtained from a homogeneous transparent film is considered. This is then extended to the case of a DBR, allowing qualitative predictions of the expected behaviour to be made.

A schematic of the experimental setup for measuring a transparent, homogeneous film deposited on a crystalline silicon substrate is shown in Figure 5.1. Picosecond strain pulses are generated by a pulsed optical excitation of an aluminium (Al) film, deposited on the back side of the substrate [22] . These strain pulses are injected into the substrate where they propagate in the z-direction with the velocity of longitudinal sound until they reach the transparent film. The strain pulse is partially transmitted into the film and propagates through with a sound velocity, s_0.

The spatial/temporal evolution of the displacement, $u_z(z - s_0t)$, and strain, $\eta_{zz}(z-s_0t)$, pulses shown in Figure 5.2 may, in practice, be described by a Gaussian function and its derivative respectively:

$$u_z(z') = u_0 \exp\left(-\frac{z'^2}{z_0^2}\right), \qquad \eta_{zz}(z') = \frac{du_z}{dz} = -\frac{2u_0 z'}{z_0^2}\exp\left(-\frac{z'^2}{z_0^{\,2}}\right) \quad (5.1)$$

where $z' = z - s_0t$ is the reduced coordinate, z_0 is a parameter which characterizes the width of the displacement pulses and u_0 is its amplitude (see Figure 5.2) and t is time. The strain pulse, $\eta_{zz}(z - s_0t)$, has an anti-symmetric shape with an amplitude, $\eta_0 = 1.2u_0/z_0$, and the spatial interval between the minimum and maximum points is $\sqrt{2}z_0$. The values of z_0, u_0 and η_0, shown schematically in Figure 5.2, depend on the optical pump excitation conditions and the properties of both the substrate and the film. Typically, for solid substrates like sapphire or silicon, and soft (e.g. polymer) films, $z_0 \sim 10$ nm, which is smaller than the typical period of DBRs and photonic cavities designed to manipulate visible light.

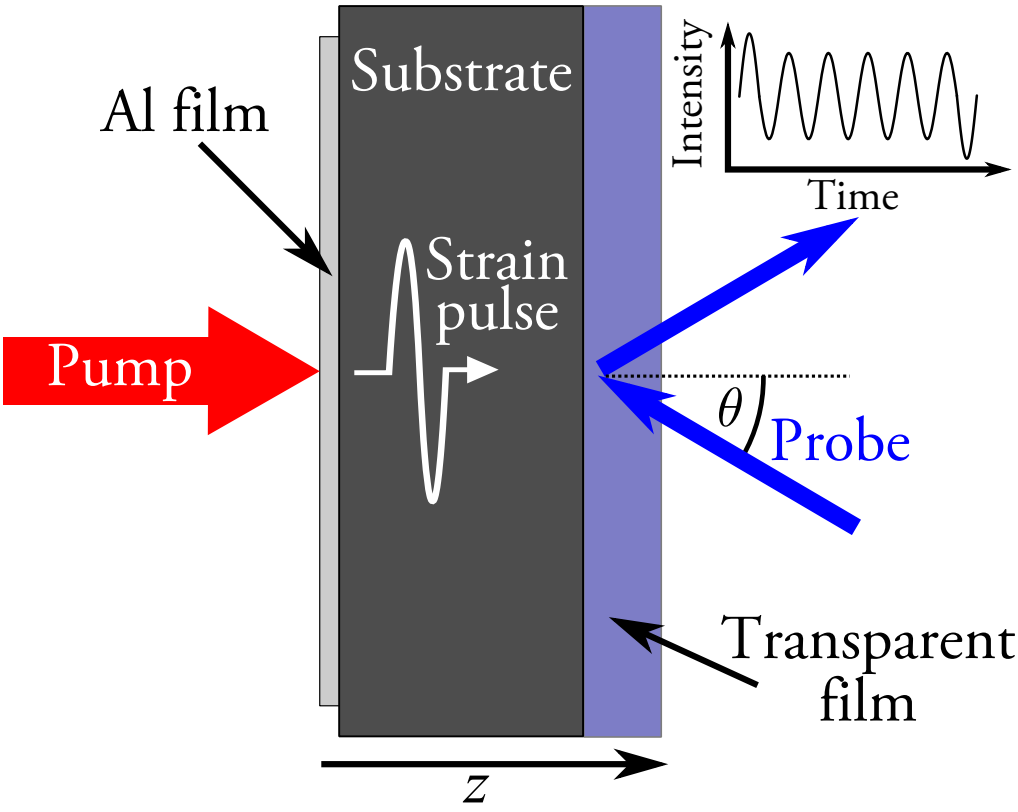

Figure 5.1: A schematic showing an experimental set-up used to perform picosecond acoustic interferometry on a transparent, homogeneous film. The inset shows an example output signal where the reflected probe intensity is modulated by the strain pulse.

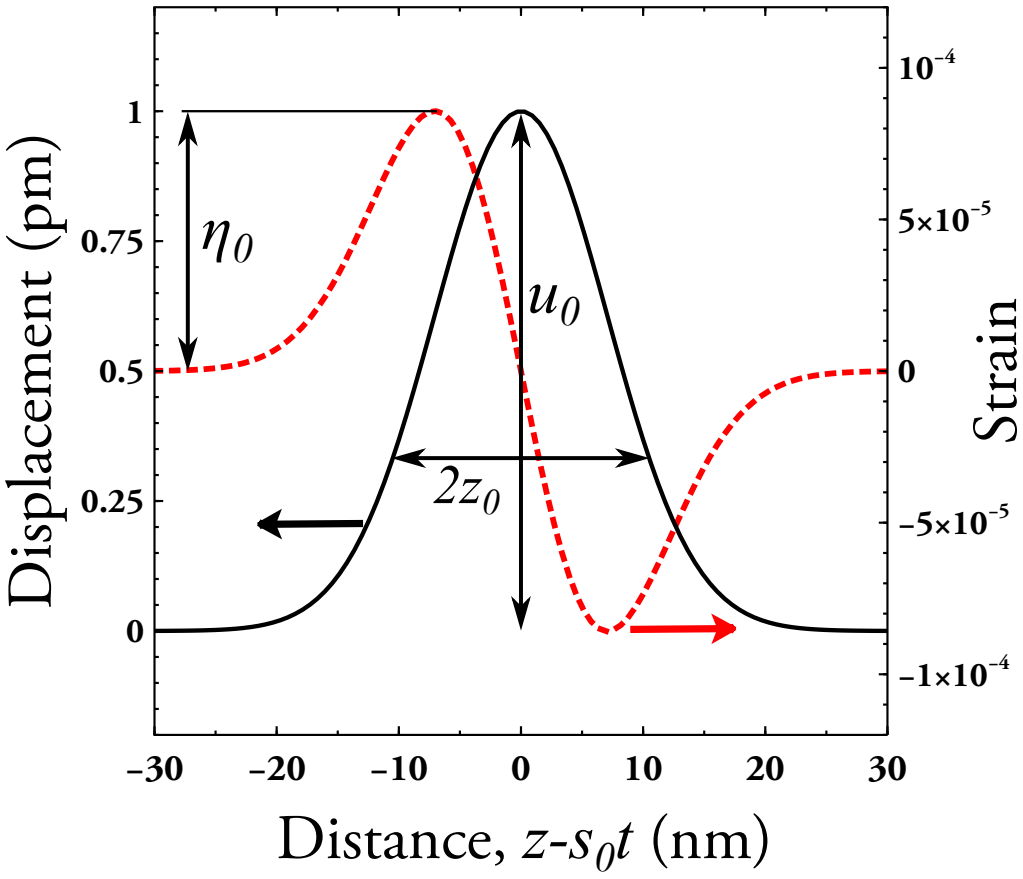

Figure 5.2: This graph shows the expected Gaussian shape of the displacement pulse (black, solid line) and the related strain (red, dashed line).

The maximum reliable experimental displacement and strain amplitudes are $u_0 \sim 10^{-11}$ m and $\eta_0 \sim 10^{-3}$ respectively [22]. The strain pulses can be considered as picosecond acoustic wavepackets with a broad spectrum of plane acoustic waves, $u \sim e^{-i(\omega t - q_z z)}$, where the dependence of frequency, ω, on the wavevector, q_z, is given by the dispersion relation for acoustic phonons. Thus, for bulk, homogeneous media, $\omega = s_0 q_z$, and in practice the acoustic wavepacket of the picosecond strain pulse is centred at the frequency 30-50 GHz depending on the excitation conditions [21].

As the strain pulse propagates through the film, it creates local changes in density, which change the permittivity tensor and thus modulate the optical reflectance of the sample. If the thickness of the film is significantly larger than the optical wavelength, then the effect of the strain pulse may be considered qualitatively as additional source of reflection of an incident probe beam inside the film. The light reflected from the strain pulse then interferes with the light reflected from the surface of the film and the substrate. As the strain pulse propagates through the films, the phase relation between the reflected beams changes periodically between constructive and destructive interference. This results in the output intensity of the reflected probe beam, $I(t)$, oscillating with a period, T, described by the equation [22]:

$$T = \frac{\lambda}{2 s_0 \sqrt{\epsilon - \sin^2 \theta}} \tag{5.2}$$

where ϵ and θ are the permittivity of the film and the angle of incidence of the probe beam respectively. The oscillations are often called Brillouin oscillations because the inverse period T^{-1} is equal to the frequency shift in the Brillouin spectrum for specular reflected light. The amplitudes of Brillouin oscillations are governed by the changes, $\delta\epsilon_{ij}$, of the permittivity tensor, ϵ_{ij}, which for isotropic media may be written as [70]:

$$\delta\epsilon_{xx} = \delta\epsilon_{yy} = -\epsilon_0^2 p_{12}\eta zz \quad \text{and} \quad \delta\epsilon_{zz} = -\epsilon_0^2 p_{11}\eta zz \tag{5.3}$$

where p_{12} and p_{11} - are elasto-optical constants. In addition to the Brillouin oscillations, $I(t)$ will also contain oscillating components due to the change of the total film thickness at times, t, when the strain pulse reaches the substrate and air interfaces of the film. An example of an output signal due to the modulation of the film reflectance by these effects is shown schematically in the inset of Figure 5.1.

It is important to note that Eq. 5.2 can also be obtained by considering momentum conservation for the interaction between the optical probe beam and an acoustic plane wave with frequency $\omega = 2\pi T^{-1}$ in the wavepacket of the picosecond strain pulse. The wavevectors of the specular reflected optical and acoustic waves, $\mathbf{k}$ and $\mathbf{q}$ respectively, should fulfill the condition, $q_z = 2k_z$, and by taking into account the linear dispersion relations of both the light and sound, Eq. 5.2 can be obtained.

If the homogeneous film is replaced by a DBR, the origin of the oscillations in the reflected light becomes more complicated to understand due to the periodically varying nature of the DBR structure. A DBR is defined as being formed by n periodically alternating layers with thicknesses d_1 and d_2 and permittivities ϵ_1 and ϵ_2 respectively (see Figure 5.3). First, considering the Brillouin oscillations, and using the momentum conservation argument as above, the periodic optical properties of the DBR modify the condition for conservation to give:

$$q_z = 2k_z + \frac{2\pi l}{d_1 + d_2} \tag{5.4}$$

where $l = 0, \pm 1, \pm 2 \ldots$. At $l = 0$, Eq. 5.4 reduces to the same condition as for the homogeneous film, but if $l \neq 0$ it is clear that several acoustic harmonics may contribute. Moreover, the presence of both photonic, and

potentially, phononic stop bands leads to non-linear dispersion relations. Together, this acts to change the dependence of the period of the oscillations on the angle of incidence of the probe beam from that in Eq. 5.2, and renders it non-linear with respect to λ.

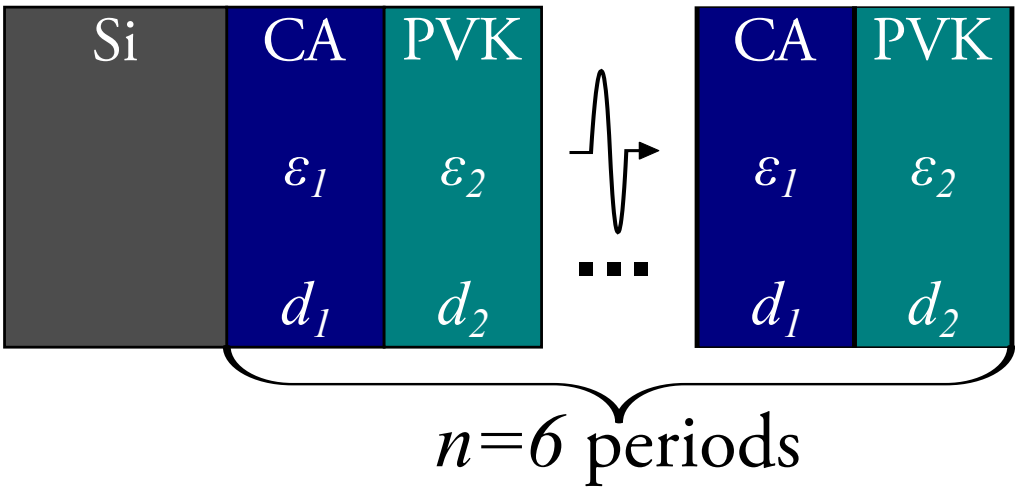

Figure 5.3: A schematic showing the structure of the experimentally measured DBR, consisting of alternating layers of CA and PVK on a Si substrate.

Secondly, as the strain pulse travels through the DBR, it modulates the position of the internal interfaces between layers. As the position of these interfaces changes, the interference conditions inside the DBR change. This modulates the reflectance of the DBR and leads to further oscillations in the reflected signal, $I(t)$. These changes are generally not harmonic oscillations and their temporal evolution requires special consideration as discussed below.

The specific tasks of the work in this chapter were to characterize the period of Brillouin oscillations in a DBR and to investigate the spectrum of these photoelastically generated oscillations in the DBRs. A DBR was deliberately chosen where no acoustic mismatch existed between the layers and the decision was made to concentrate on optical wavelengths in the vicinity of first PSB. This case is most important in practice when the

operating wavelength in nanophotonic devices falls into the PSB of the DBR.

In the work shown below, the main qualitative conclusions obtained from the picosecond acoustic interferometry experiments are that the angular and wavelength dependencies of the oscillation period are suppressed in the region of the photonic stop band. These conclusions are supported by numerical calculations that show good agreement, suggesting that the essential physics of this situation has been captured.

5.3 Method

The polymer DBRs were prepared on 50 μm thick, polished Si substrates by spin coating alternating layers of commercially available cellulose acetate (CA) and poly-9-vinylcarbyzole (PVK) from mutually exclusive solvents (diacetone alcohol and chlorobenzene respectively) using a technique similar to that reported previously [71]. The densities of the polymers were $\rho_{CA} = 1.3$ g cm^{-3} and $\rho_{PVK} = 1.2$ g cm^{-3} respectively. The resulting structure consisted of 6 repeating polymer bilayers with a 72 ± 1 nm CA film on the bottom and a 65 ± 2 nm PVK film on top (12 layers in total). The individual layer thickness values were measured using a single wavelength self-nulling ellipsometer ($\lambda = 633$ nm, 60° angle of incidence). The entire sample was annealed for 12 hours under vacuum (1 mtorr) at 145 °C to remove residual solvent and any stresses that might have been introduced in the multilayer structure during the spin coating procedure.

The permittivities ϵ_{CA} and ϵ_{PVK} of the polymers were measured using a spectroscopic ellipsometer (J.A. Woollam Co., Inc., α-SE$^{\text{TM}}$) and at $\lambda = 400$ nm, $\epsilon_{CA} = 2.22$ and $\epsilon_{PVK} = 3.06$. Figure 5.4(a) shows the measured reflectance spectra of the studied DBR at three different angles of incidence, θ. The spectra show a clear photonic stop band near to 400 nm. The wavelength of the centre of the stop band decreases as θ increases. The measured spectra show good agreement in the position, width and angular dependence compared to theoretical predictions calculated using an optical transfer matrix method based on the measured thicknesses and refractive indices of the multilayer structure (Figure 5.4(b)).

The transfer matrix method used was similar to that described in Section 3.2, where the structure is represented as a series of 2x2 matrices that describe the effect to incident light of either a layer or a boundary between layers. By multiplying these together, a total matrix, M that corresponds

to the optical response of the entire structure is obtained. Intuitively, this has the form of a boundary matrix, similar to that described in Equation 3.2, so we can use it to calculate the Fresnel reflection coefficient, r for the structure. From this, the reflectance can be calculated as a percentage as:

$$\text{Reflectance} = rr^* \times 100 \tag{5.5}$$

The picosecond acoustic experiments were performed at room temperature. Before the DBRs were deposited, an Al film with a thickness of 75 nm had been thermally evaporated on to the back surface of the Si substrate. This Al film was excited using 60 fs optical (pump) pulses from an amplified Ti-sapphire laser (λ = 800 nm), with a repetition rate of 5 kHz. The pump beam was focused to a 200 μm diameter spot which resulted in the maximum energy density on the Al film being $\sim$ 10 mJ cm^{-2}. The estimated parameters of the strain and displacement pulses injected into the DBR are as shown in Figure 5.1(b).

The high-frequency acoustic properties of the polymers that formed the DBR were studied independently. Single CA and PVK films, 82$\pm$1 and 51$\pm$ 2 nm thick respectively, were excited as above, and the coherent oscillations of closed organ-pipe modes in the films were measured. Examples of these measurements are shown in Figure 5.5. Recalling Equation 4.2 these modes have frequencies described as [27]:

$$f_n = \frac{(2n+1)s}{4d},$$

where n is an integer, s is the longitudinal (LA) speed of sound in the polymer and d is the thickness of the polymer film. Hence, from these frequencies, the values for the longitudinal sound velocities in the polymers, s_{CA} and s_{PVK}, were obtained. In these films s_{CA} = 2600 ms^{-1} and s_{PVK} = 2400 ms^{-1}, with decay time $\sim$4 ns at $\sim$10 GHz. Consequently, the acoustic impedances, $Z_{CA} = \rho_{CA}s_{CA}$ and $Z_{PVK} = \rho_{PVK}s_{PVK}$, of the polymer

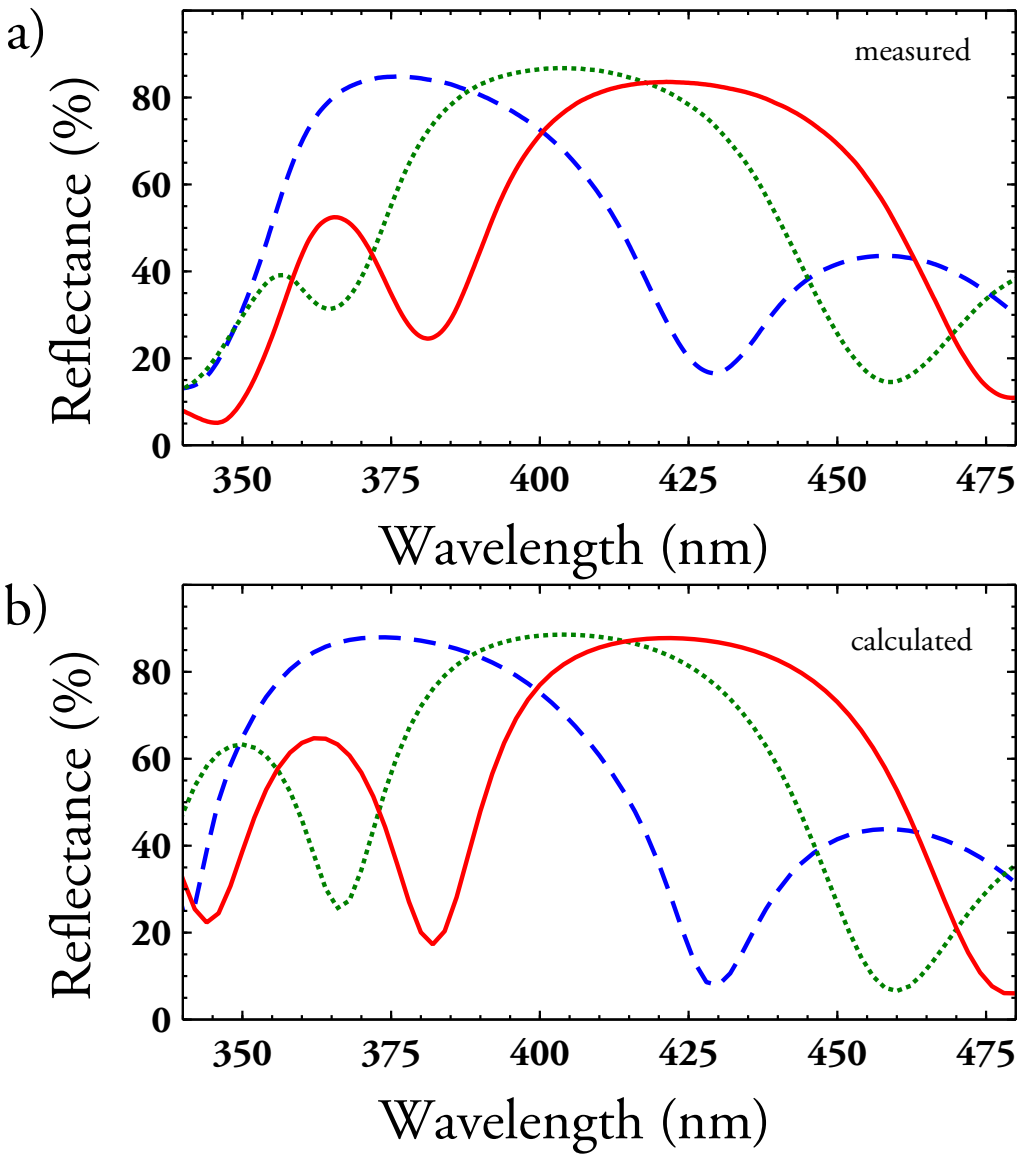

Figure 5.4: Measured (a) and calculated (b) reflectance spectra for the DBR studied, obtained at three different angles, 20° (red, solid line), 35° (green, dotted line), 55° (blue, dashed line).

layers are very close: $Z_{CA} \approx Z_{PVK} \approx 3$ MPa.s.m^{-1} which allows both reflections of the strain pulse at CA/PVK interfaces and effects related to the phononic stop bands in the DBR to be ignored. In this case, the strain pulse injected into the DBR propagates through the sample with the same temporal/spatial shape until it reaches the interface of the DBR with the air. There, the strain pulse is reflected with an associated phase change and propagates back towards the Si substrate.

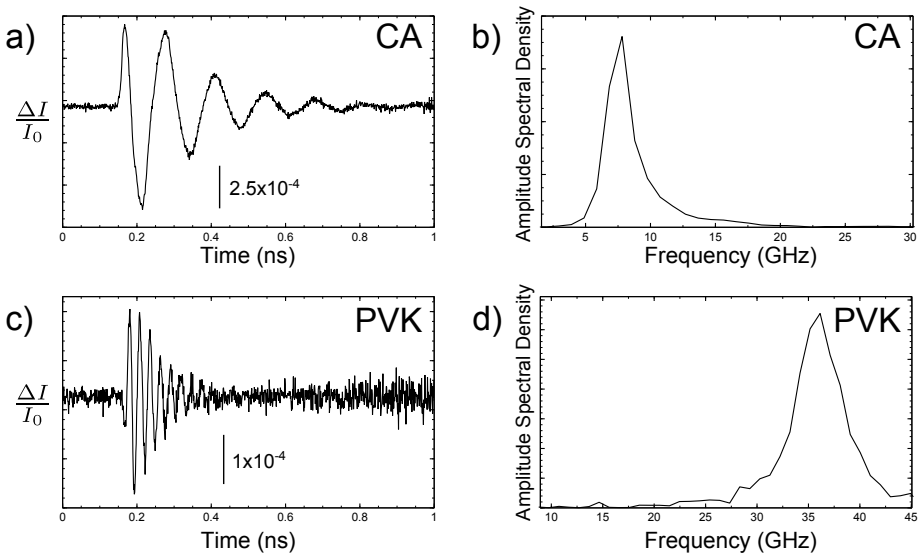

Figure 5.5: Example measured signals and associated FFT results for both the CA single film ((a) and (b) respectively) and the PVK film ((c) and (d)). The CA film gave a larger signal with a strong f_0 mode, whereas the PVK films yielded smaller signals with oscillations primarily evident in the f_1 mode as evidenced by the faster decay and higher frequency.

5.4 Results

The main goal of the experiments was to measure the temporal evolution of the optical reflectance changes as the strain pulse propagated through the DBR. Picosecond temporal resolution is achieved by probing the reflectance of the DBR with a second harmonic optical pulse, originating from the same femtosecond laser that provides the pump beam. The intensity of the reflected probe pulse, $I(t)$, is measured as a function of t, the delay of the probe pulse relative to the pump excitation of the Al transducer. The wavelength of the probing beam, $\lambda = 400$ nm, was fixed, so the spectral position of the probe light relative to the PSB of the DBR was controlled instead by changing the angle of incidence, θ (see Figure 5.1). In addition, the probe beam could be either *s*- or *p*- polarized.

The signals, $\Delta I(t)/I_0$, ($\Delta I(t) = I(t) - I_0$, where I_0 is the intensity of the probe beam reflected from the sample without any pump excitation, i.e. no oscillation in the sample) measured for three values of θ are shown in Figure 5.6(a). All signals show oscillations starting at $t_1 = 6.11$ ns which corresponds to the time it takes for the strain pulse to propagate through the Si substrate. The period T of the oscillations varies depending on both θ and the polarization and $I(t)$ changes abruptly at $t_2 = 6.46$ ns which corresponds to the time when the strain pulse hits the DBR/air interface. The left and right dashed vertical lines in Figure 5.6(a) indicate the values of t_1 and t_2 and thus, the interval between the dashed lines corresponds to the time $t_1 < t < t_2$, where the strain pulse is travelling through the DBR, after the injection from Si substrate and before the first reflection from the DBR/air interface. This transient time window, where the oscillations have the highest amplitudes, is the most useful for further analysis because it does not include the phase modulation of $I(t)$ due to reflections from the Si/DBR and DBR/air interfaces. The measured values

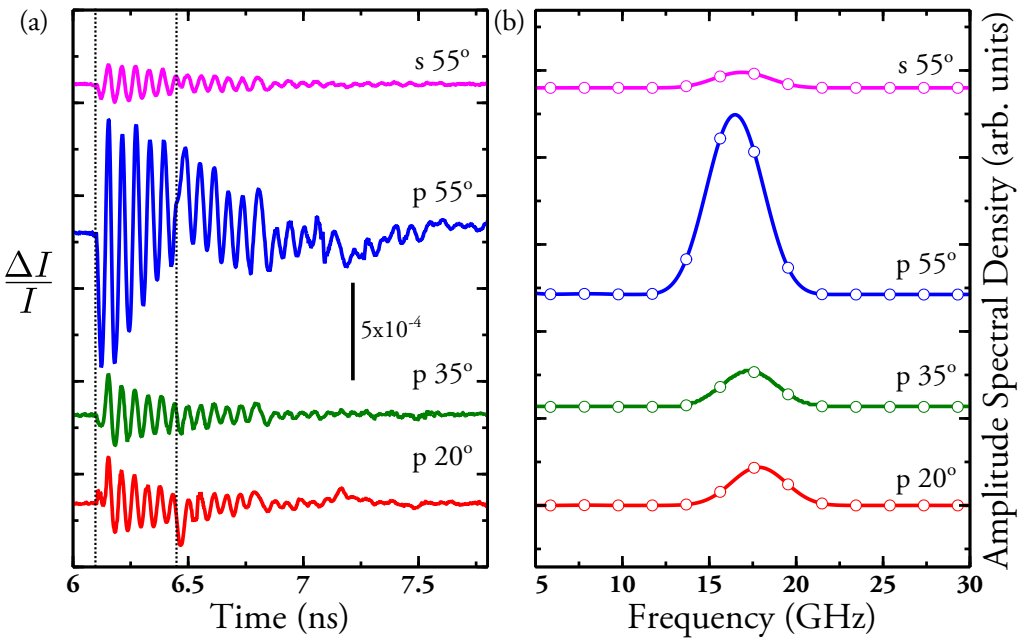

Figure 5.6: (a) Examples of the signals obtained in the picosecond acoustic experiments for a variety of polarizations and angles of incidence. (b) Results of FFT's performed on the signal in the time window between the dotted lines in (a) (dots). Also shown are the results of zero-padded FFT's (solid lines) to act as a guide for the eye. It is clear that only one spectral component is resolved for the time window considered.

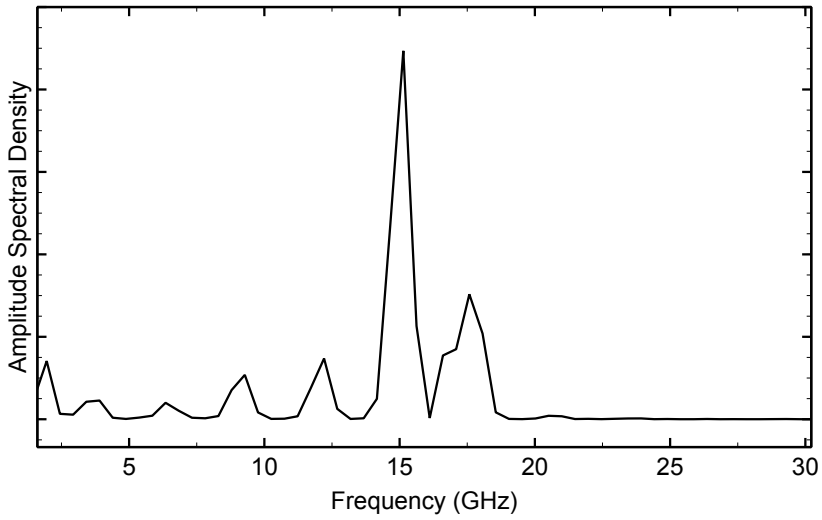

Figure 5.7: An example of an FFT performed on the whole signal with multiple peaks due to vibrations of the whole film. This spectrum is for the p55° signal seen in Figure 5.6(a)

of t_1 and t_2 allow an estimate of the average sound velocity in the DBR to be obtained as $\bar{s} = 2343$ ms^{-1}. This is 6% less than the mean sound velocity obtained from the measurements on individual films. This small difference in $\bar{s}$ is likely due to water present in the single films which were stored for a period after annealing before measurement. CA in particular is prone to swelling and holding water [72], likely changing both its thickness but also its acoustic properties slightly. By comparison, the CA films in the multilayer structure were annealed and immediately 'capped' by PVK films, preventing this swelling.

Figure 5.6(b) shows the spectra of the measured signals, $\Delta I(t)/I_0$, obtained by fast Fourier transforming (FFT) the signal in the transient time window between the dashed lines in Figure 5.6(a). The spectra show only one line centred at a frequency, f, between 15 and 20 GHz that is weakly dependent on the angle θ and the probe beam polarization. The fact that there is a single spectral line supports the assumption that, for the case presented here, multiple reflections of acoustic waves at the internal interfaces of the DBR may be ignored. If this were not the case, $\Delta I(t)/I_0$ would display beating oscillations, and the spectrum would consist of more than one peak [22]. The width of the spectral line is limited by the width of the time window of the FFT. If a longer time window encompassing the whole signal is used (6 ns $< t <$ 8 ns), then the signal includes the phase shifts of $\Delta I(t)/I_0$ from strain pulse reflection at the DBR/Air and DBR/Si interfaces and eventually detects vibrations of the whole DBR structure, which has a total thickness of 820 nm. FFT's performed in this time window are more complicated compared to those in Figure 5.6(b), consisting of several narrow lines, for an example, see Figure 5.7. For the periodic structure of the DBR, these contributions to the FFT spectra due to vibrations of the whole film mask the features specific to the acousto-optical interactions inside the DBR and thus will not be addressed further.

The oscillatory behaviour of $\Delta I(t)/I_0$ in the DBR sample studied displays similar characteristics to the case of a homogeneous film of a transparent material [68]. As discussed above, the oscillations are the result of the interference of the probe beams reflected from the transient strain pulse, which propagates at the LA sound velocity in the polymers, and those reflected from the surface of the film and CA/Si interface. The task remains to understand the reason for the existence of harmonic oscillations with a single frequency and the absence of higher spectral components which might be expected based upon the predictions of 5.4.

5.5 Discussion

It is useful to start by discussing qualitatively what the expected modulation of the signal will be in the ideal case of a semi-infinite DBR ($n \to \infty$). First, the photoelastic effects will be considered by returning to the momentum conservation description of the Brillouin oscillations.

Starting with the condition for momentum conservation from Eq. 5.4, a simplification where the $l = 0$ mode is the dominant contribution to the signal will be used. This happens when the perturbations to the permittivity tensor, $\delta\epsilon_{ij}$, are equal throughout the DBR and the dielectric contrast between the individual layers is also small. When this is the case, the amplitude of electromagnetic waves corresponding to higher harmonics due to permittivity modulation in the structure will be negligible. As such, there will only be one solution for q_z and in an acoustically homogeneous DBR, only a single frequency in the wavepacket of the strain pulse will modulate the reflected light.

When the wavelength, λ, of the light incident on the DBR is far from the PSB, there is no significant difference from the case of a homogeneous film. The period, T, of the oscillations will be accurately described by Equation 5.2. When λ falls within the PSB, however, the oscillatory behaviour becomes significantly different. This corresponds to wavelengths: $\lambda_l < \lambda < \lambda_h$, where λ_l and λ_h are the optical wavelengths that correspond to the lower and upper edges of the PSB respectively, shown schematically in Figure 5.8. In the centre of the PSB of a semi-infinite DBR, the reflectance is close to unity, so is not strongly dependent on changes in permittivity. Using the momentum conservation condition in Equation 5.4, with $l = 0$, it can be shown that when probing inside the PSB ($\lambda_l < \lambda < \lambda_h$), q_z is independent of λ: $q_z = \mathrm{Re}(k_z) \approx 2\pi/(d_1 + d_2)$. The frequency, ω, of the acoustic modes that interact with the optical beam therefore, is governed

by the acoustic dispersion relation, $\omega(\mathbf{q})$. For the work here, the acoustic contrast between layers is small, so using a linear dispersion relation, $\omega = \bar{s}q_z$, where $\bar{s}$ is the mean sound velocity in the DBR, is valid [47]. In this case then, the period of Brillouin oscillations in an ideal semi-infinite DBR does not depend on λ when $\lambda_l < \lambda < \lambda_h$.

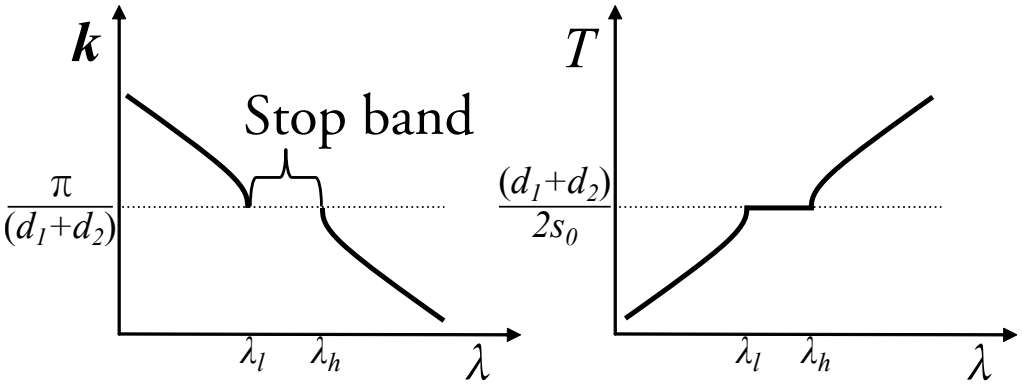

Figure 5.8: The optical dispersion relation of a semi-infinite ($n \gg 1$) DBR and the period (T) of the Brillouin oscillations in such a structure in the region of the photonic stop band.

The second effect governing the acousto-optical output of the DBR is modulation of the position of interfaces in the sample. The reflectance of the DBR changes when the strain pulse is passing the edges of the DBR, similar to the homogeneous film, but also when the pulse passes internal interfaces between layers. The maximum shift of an interface is typically equal to the amplitude, u_0, of the displacement pulse. For narrow strain pulses ($z_0 \ll d_1, d_2$) the modulation of the interfaces should result in the appearance of spikes in the temporal evolution of the reflected signal. The time intervals between the nearest spikes of opposite phase will be equal to the time it takes for the strain pulse to propagate through each layer, d_1/s_1 and d_2/s_2 respectively, and be independent of the probing wavelength λ and incident angle θ.

The numerical analysis presented below has two goals: to provide quan-

titative support to the qualitative description based on momentum conservation; and to compare the experimental results described in Section 5.4 with numerical calculations. The calculations were performed for a DBR with the same parameters as those used in the experiments: the permittivities were $\epsilon_1 = \epsilon_{CA} = 2.22$ and $\epsilon_2 = \epsilon_{PVK} = 3.06$ at 400 nm; layer thicknesses were $d_1 = 72$ nm and $d_2 = 65$ nm corresponding to the thicknesses of CA and PVK layers respectively The dispersion of ϵ_1, ϵ_2 and the permittivity of Si were taken into account in the calculations;. The calculated edges of the PSB for a semi-infinite DBR of these materials are $\lambda_l = 419$ nm and $\lambda_h = 457$ nm. As discussed, multiple reflections of the strain pulses at interfaces inside the DBR were not considered and a mean sound velocity inside the DBR, $s = 2343$ ms^{-1}, was used.

The numerical calculations of $\Delta I(t)/I_0$ were performed by our collaborator, N. A. Gippius. They were made using a standard transfer matrix formalism, that accounted for modifications of both the layer thickness and the refractive index due to the strain pulse (photoelastic effect). The latter was assumed to be static, i.e. small Doppler shifts were ignored as they were much smaller than the spectral resolution of the experiments. The parameters of the strain pulse (see Figure 5.2) used in the calculations were $z_0 = 10$ nm and $u_0 = 1$ pm. The optical beam was taken to have an infinitely narrow spectral width, which is valid in situations where the spectral width of the probing pulse (3 nm for the experiments here) is smaller than the width of typical spectral features in the DBR's reflectance spectra shown in Figure 5.4. The elasto-optical constants (see Equation 5.3) were chosen to be the same in each polymer, so that the perturbations of the permittivity, $\delta\epsilon_{ij}$, are the same for each layer ($\epsilon_{CA}^2 p_{12}^{CA} = \epsilon_{PVK}^2 p_{12}^{PVK} = \beta$). This simplification, which is unlikely to be exactly realized in practice, allows the general properties of the acousto-optical effects inside DBRs to be understood.

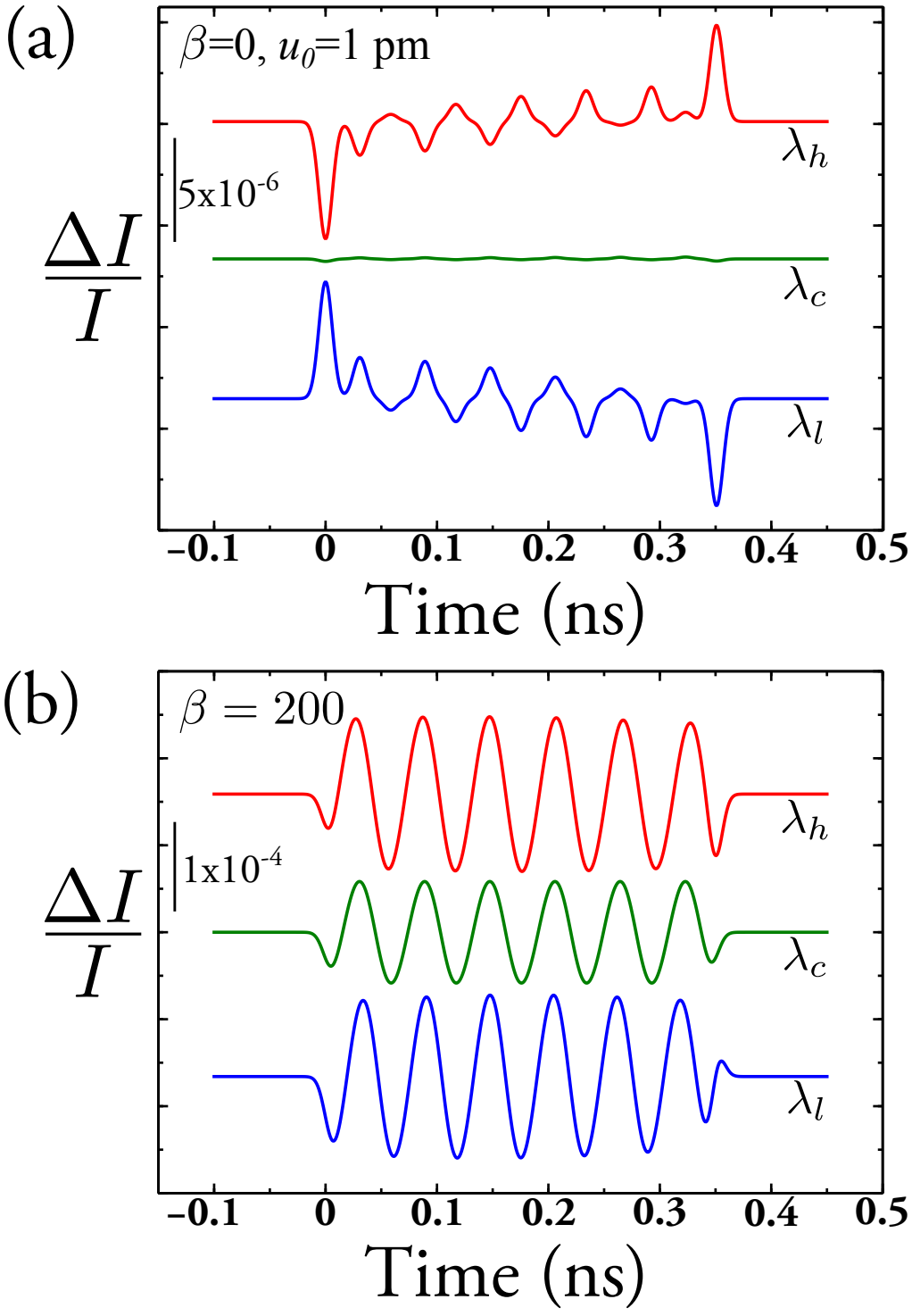

Figure 5.9: (a) Calculated signals at different wavelengths of incident light for the experimental DBR considering only the changes in structure due displacement of internal interfaces. (b) Calculated signals at different wavelengths of incident light for the experimental DBR where photoelastic modulation of the structure is dominant i.e. β is large.

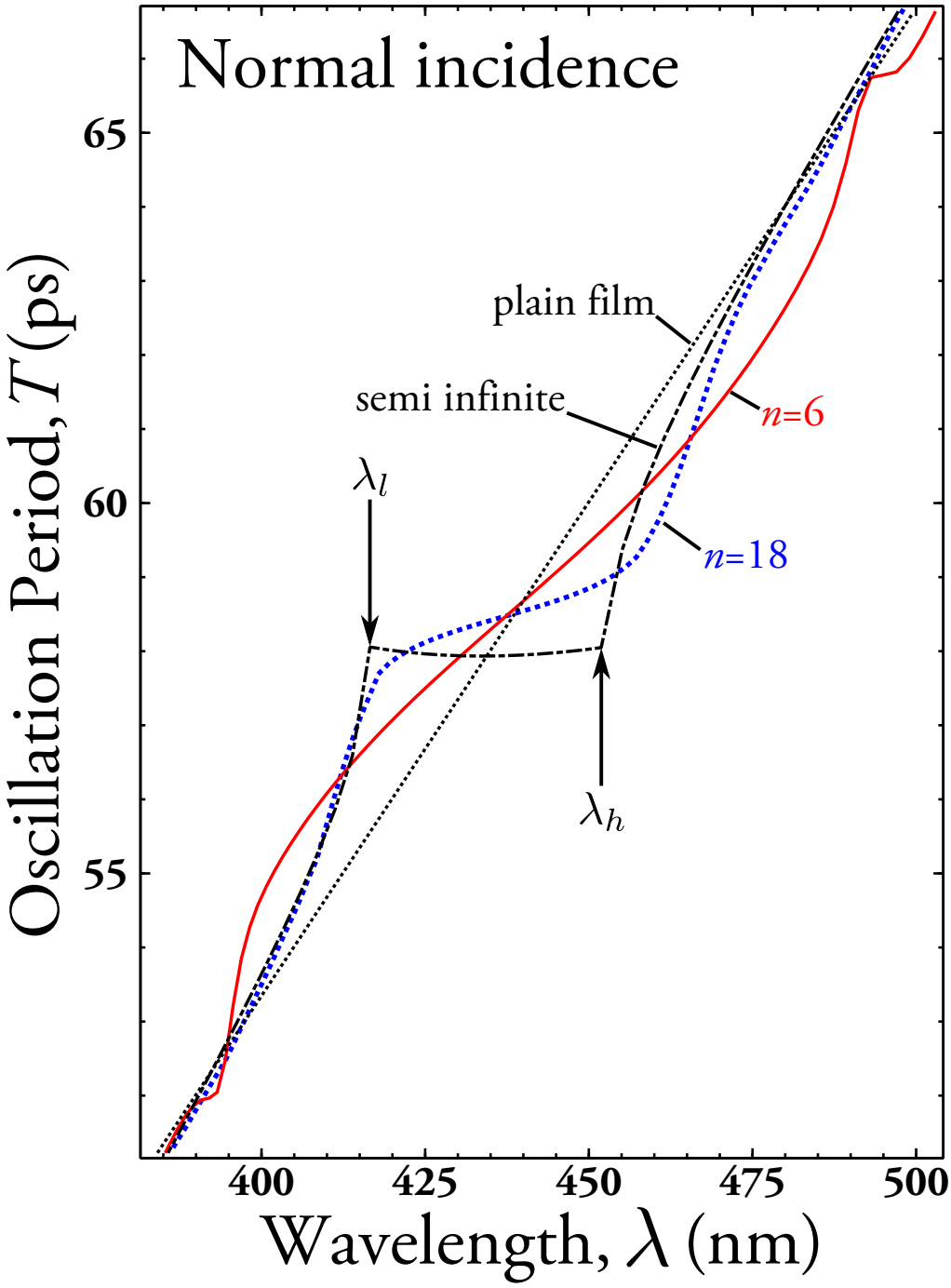

Figure 5.10: Results of calculations of the incident wavelength dependence of the oscillation period, T, for increasing numbers of layers in the DBR. As the number of layers increases, the dependence of T tends towards to the case for a semi-infinite DBR as expected.

The signals, $\Delta I(t)/I_0$, were calculated as a function of the probing wavelength, λ, in order to show how close the dependence of the oscillation period T on λ in real DRBs is to the case when $n \to \infty$. $\Delta I(t)/I_0$ was calculated for $n = 6$, at three values of λ, corresponding to the centre and each edge of the PSB. To demonstrate the effect of each mechanism for acousto-optical modulation, two extreme cases for the strength of the photoelastic effect are shown: $\beta = 0$ (Figure 5.9(a)) and $|\beta| = 200$ (Figure 5.9(b)). These correspond to purely interface displacement driven modulation and to a dominantly photoelastic modulation respectively. These two effects are shown schematically in Figure 5.11. The temporal evolution of $\Delta I(t)/I_0$ in these two cases is very different: the signal induced by interface displacement is strongly anharmonic and the position of the peaks in the signal does not depend on λ; the signal dominated by photoelastic mechanisms is harmonic and the period, T, of the oscillations appears to depend slightly on λ.

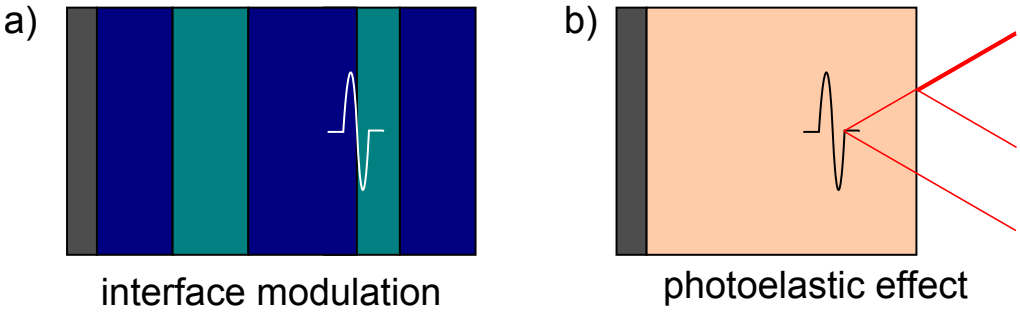

Figure 5.11: This figure show schematically how the two mechanisms for modulation of the structures optical response work. a) shows modulation of the interfaces, where the strain pulse shifts the position of an interface in the structure, changing the optical depth of that layer. b) shows the photoelastic effect, where the strain pulse creates a small change in the local dielectric properties of the polymer meaning that some light is reflected off the pulse. This interferes with light reflected from the surface of the structure.

The amplitude of $\Delta I(t)/I_0$ when probing at the centre of the PSB

($\lambda = \lambda_c$) is less than when probing at the edges. It is obvious that in the semi-infinite PSB, when the reflectance is 100% for $\lambda_l < \lambda < \lambda_h$, the amplitude of the signal will be zero for both mechanisms. For the finite number of periods there will be always non-zero modulation but as shown in Figure 5.9(a) and (b) the difference in the amplitudes between probing with λ inside and outside the PSB is very different for two mechanisms: for the changes of the reflectance induced by the displacement of the interfaces the amplitude decreases by a factor of 40-50 when probing in PSB of the DBR with $n = 6$; when considering only the photoelastic mechanism in the same PSB the amplitude of $\Delta I(t)/I_0$ is a factor of two smaller than when probing at the edges . The slight dependence of T on λ in the region of the PSB appears contrary to the qualitative discussion above. It is, however, a consequence of the fact that this calculation is for a real DBR, with a finite number of layers.

Figure 5.10 shows the dependence of the oscillation period, T, on λ for two DBRs: $n = 6$, the same as the measured structure; and $n = 18$, a DBR three times the size. These are calculated for the case where the photoelastic effect is dominant ($|\beta| \gg 1$). These calculations are compared to a curve corresponding to a semi-infinite DBR. The dashed-dotted line corresponds to a homogeneous film with $\epsilon = 2.62$. It can be seen that in the vicinity of the PSB, for $n = 6$, $T(\lambda)$ already differs by several percent relative to the homogeneous film. As n increases, T becomes increasingly sensitive to λ at the very edges of the stop band (λ_l and λ_h) while the dependence inside the stop band decreases. As expected, further increasing n results in $T(\lambda)$ approaching the case of the semi-infinite DBR.

These results serve to show that the calculations support the qualitative description of the influence of the PSB on the properties of Brillouin oscillations due to the photoelastic effect in a DBR. In the given example, when the photoelastic mechanism is dominant, the difference in T in a DBR

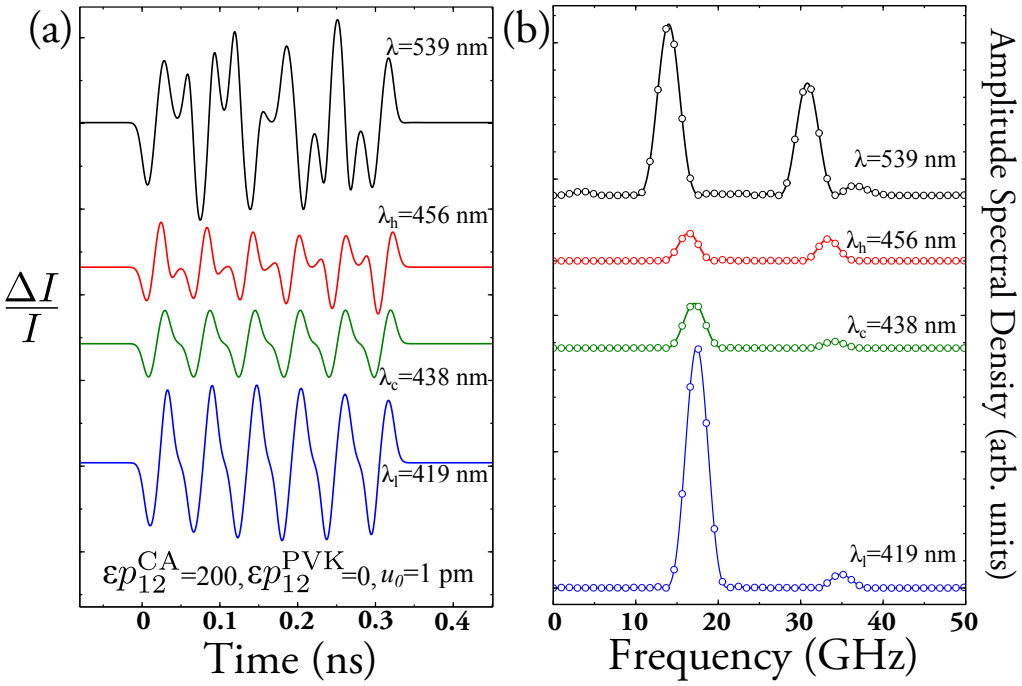

Figure 5.12: (a) shows calculated signals at a range of probe wavelengths for a DBR where the photoelastic constant of one of the materials is significantly different to the other. (b) Results of FFT's performed on the signals shown in (a) (dots). Also shown are the results of zero-padded FFT's (solid lines) to act as a guide for the eye. In this case, higher harmonics of the signal are seen to be significant and the signals are strongly anharmonic.

relative to a homogeneous film is only several percent even when $n \gg 1$. If, however, the materials of the DBR are chosen so that the elasto-optical constants are significantly different in each layer ($\epsilon_{CA}^2 p_{12}^{CA} \neq \epsilon_{PVK}^2 p_{12}^{PVK}$), further calculations, performed by our collaborator, N. A. Gippius, show the reflected signals will consist of several harmonics and the difference in the optical response becomes large when a picosecond strain pulse is applied to the DBR rather than a homogeneous film. These are shown in Figure 5.12

The results show that the FFTs of the experimentally measured signals (see Figures 5.6(a) and (b)) in the time interval $t_1 < t < t_2$ are well described by single spectral line. Thus, based on the theory above, it may be concluded that the photoelastic effect is sufficient to describe the experimentally observed acousto-optical modulations and only the fundamental ($l = 0$) mode is active in forming the reflectance signal. From a comparison of the measured and calculated amplitudes and phases of the oscillations in the signals at $\lambda = 400$ nm, for various values of θ and both s and p polarizations it is estimated that the elasto-optical constants: $p_{12}^{CA} \sim p_{12}^{PVK} \sim p_{11}^{CA} \sim p_{11}^{PVK} \sim 1$.

To convince of the agreement between calculations and experiment it is possible to make a qualitative comparison between the temporal evolution of measured and calculated signals for $p_{12}^{CA} = p_{12}^{PVK} = p_{11}^{CA} = p_{11}^{PVK} = 1$ signals, $\Delta I(t)$. The calculated signals were again provided by N. A. Gippius. They were calculated by determining a series of reflectance spectra for the DBR as the pulse moves through it via the transfer matrix method. These spectra were then multiplied with a measured spectrum for the probe beam and the result integrated to give the expected signal. Figures 5.13 and 5.14 show the measured and calculated signals for both s- and p-polarizations at two separate angles of incidence, corresponding to probing on each edge of the stop band.

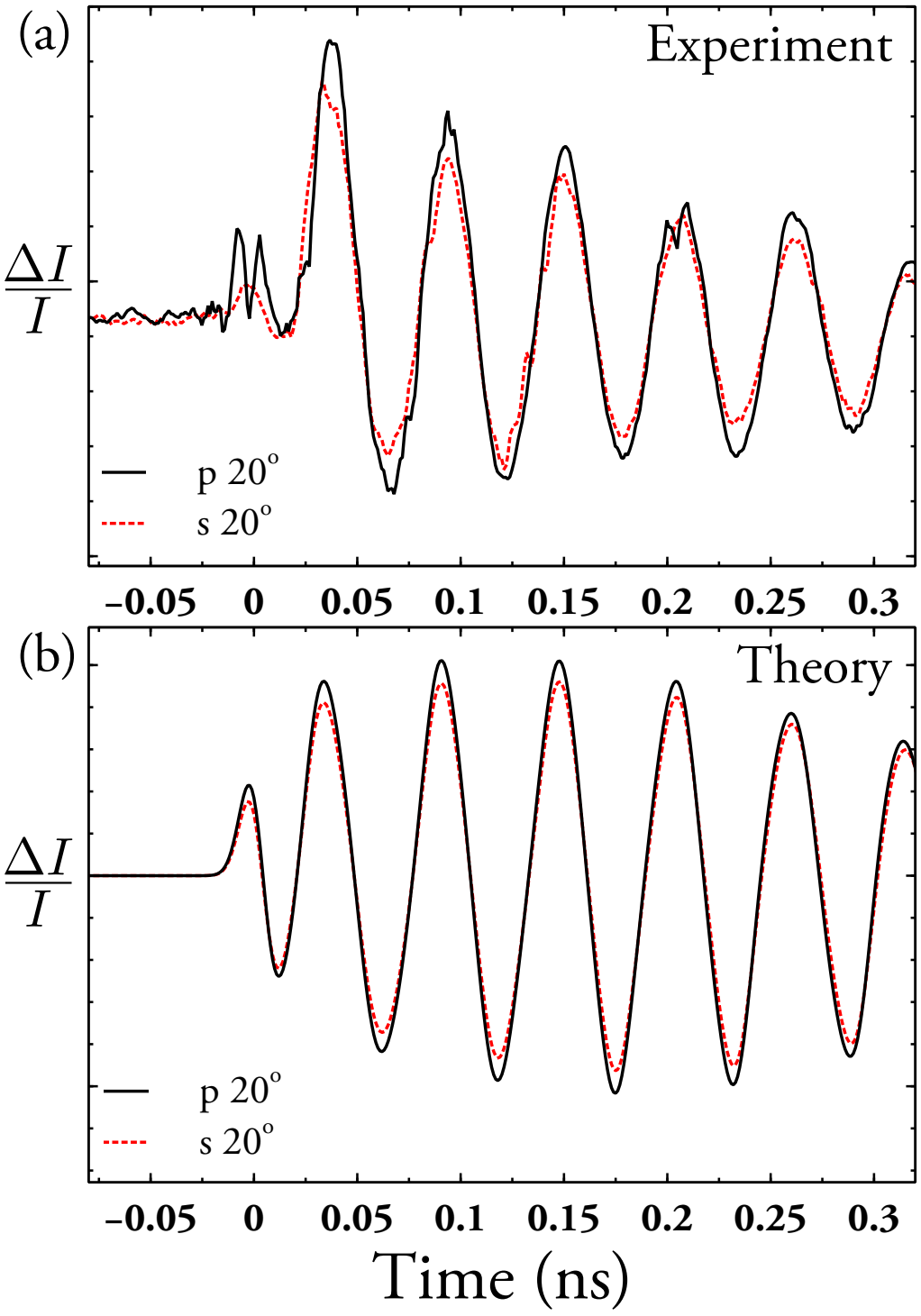

Figure 5.13: (a) & (b) show examples of experimentally measured and calculated signals respectively, for both s (dotted red line) and p (solid black line) polarizations of probe light at an angle of incidence of 20°, allowing a qualitative comparison to be made. The calculated signals reproduce the key features of the measured signals, supporting the validity of the theoretical approach applied to modelling the optical response of the DBR.

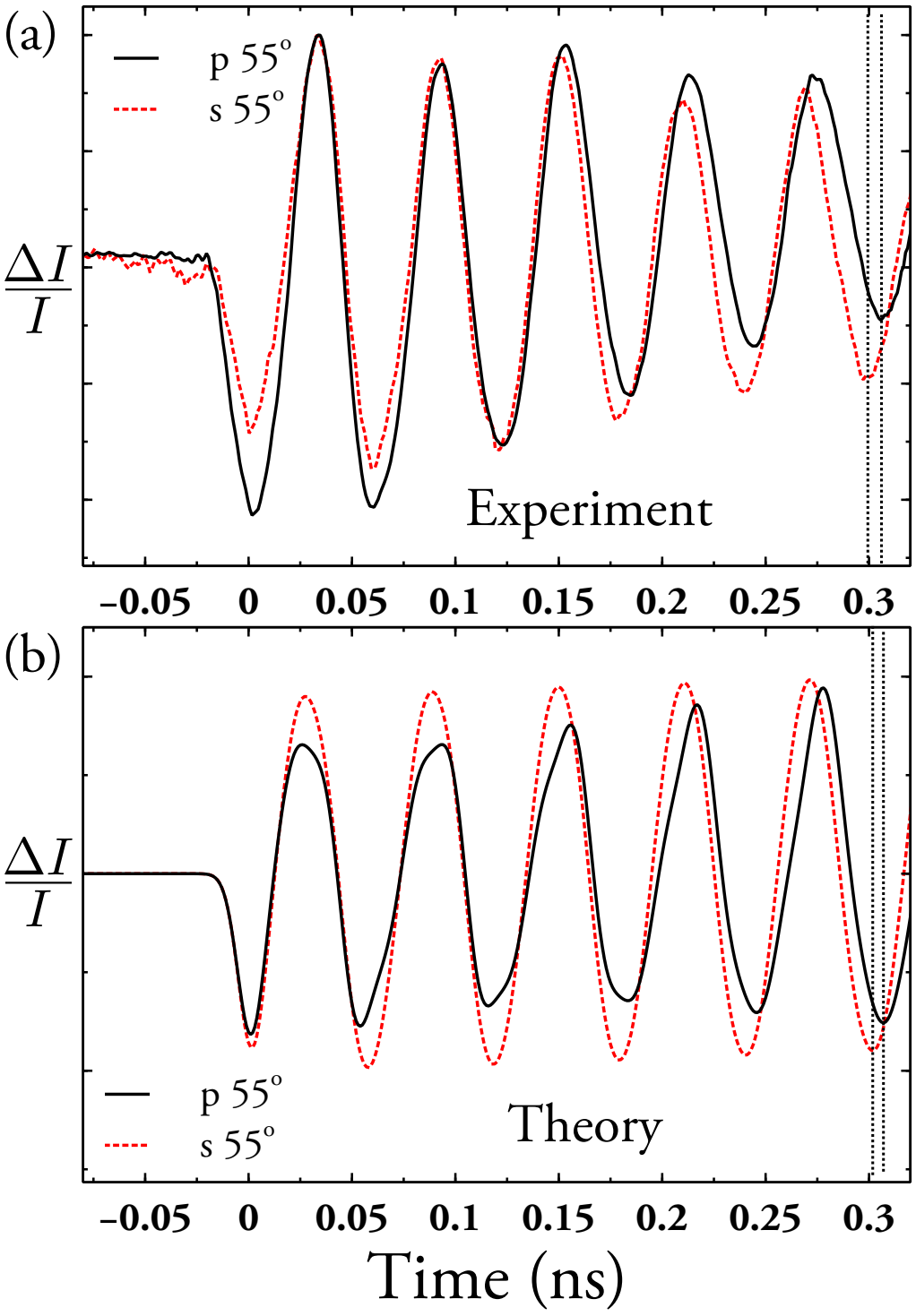

Figure 5.14: (a) & (b) show examples of experimentally measured and calculated signals respectively, for both s (dotted red line) and p (solid black line) polarizations of probe light at an angle of incidence of 55°, allowing a qualitative comparison to be made. The calculated signals reproduce the key features of the measured signals, supporting the validity of the theoretical approach applied to modelling the optical response of the DBR. The dashed vertical lines highlight the shifts in the oscillation period that are observed between the p and s components of the reflected light intensity (see text).

Both the experimental (Figures 5.13(a) and theoretical 5.14(a)) and (Figures 5.13(b) and 5.14(b)) curves show oscillations close to harmonic waveforms and are found to be in good agreement. For $\theta = 20°$ the signals $\Delta I(t)$ for different polarizations are almost the same. A small but distinguishable difference in values of T for s- and p- light is seen at the higher angle of incidence (Figure 5.14). This difference is noticeable in both, experimental and theoretical, curves when comparing the temporal positions of the maxima/minima in $\Delta I(t)$ at the times corresponding to 4th and 5th oscillations. It is important to note that this difference, indicated by vertical dashed lines in Figure 5.14, for s- and p-light is not due to optical anisotropy induced by the strain pulse because the model assumes that $\delta\epsilon_{xx} = \delta\epsilon_{yy} = \delta\epsilon_{zz}$ but is due instead to the differences in the angular dependence of the p and s reflection coefficients. This difference is not present at the lower angle of incidence due to the fact that the p and s reflection coefficients for dielectric interfaces are similar close to normal incidence. In both cases, there is good agreement between the periods obtained for the measured and calculated signals.

Theoretical $\Delta I(t)$ curves for the p polarization show small anharmonic features as shown in Figure 5.14(b) (black solid curve), which are due to the larger contribution of the interface modulation effects for large incident angles. These anharmonic features are not seen in the experimentally measured $\Delta I(t)$ [Figure 5.14(a)] due to the relatively low signal to noise ratio in the experiments.

In the above discussion the absence of modes with $l > 0$ has been attributed to the dominance of the photoelastic effect. Another reason for damping of higher harmonics in $\Delta I(t)/I_0$ could be due to strong attenuation of high-frequency acoustic components in the strain pulse wavepacket while it propagates in the polymer film. It is noted, however, that the mean free path for these high frequency phonons is larger than the period

of the DBR [26,27]. This would mean that when the strain pulse passed the first few layers in the DBR (from the substrate side) anharmonic features would be noticeable in the temporal evolution of $\Delta I(t)$. This is not observed experimentally and it may therefore be concluded that anharmonic modulations due to modes with $l > 0$ and the displacement of the interfaces of the DBR are relatively weak in the DBR studied here.

5.6 Conclusion

In summary, the reflected signals, $\Delta I(t)/I_0(t)$, induced by the picosecond strain pulse are shown to be close to harmonic when the photoelastic effect is the dominant mechanism of reflectance modulation and only the fundamental $l = 0$ mode is active. For the DBR studied in the present work, the modulated signals may be characterized by a single period, T, with a value close to that expected in a homogeneous film with a mean permittivity ϵ. The model calculations show that the angular and wavelength dependencies of this period are suppressed slightly when probing in the region of the PSB relatively to the plain film. The amplitude of the modulation depends on the position of the probe wavelength λ relative to the PSB. In DBRs with a large number of layers, n, modulations due to both the photo-elastic effect and interface displacement become negligible when λ lies in the PSB. When n is not so high, modulations due to interface displacement are negligible when $\lambda = \lambda_c$ but those due to the photo-elastic effect are still obvious in the signals. The semi-quantitative agreement between the measured and calculated signals and the success of the theoretical approach used in reproducing specific features of the signals from the DBRs suggests that the model captures the essential physics of optical modulation in these samples.

For the polymer sample structure considered here, the picosecond strain

pulse induces only small changes in the reflectance of the DBR. In fact, the maximum amplitude of $\Delta I(t)/I_0(t)$ is less than 1% and does not differ significantly from the case of a homogeneous film. Despite its weak acousto-optical response, if the DBR is used as an element in an active device (e.g. a vertical-cavity surface-emitting laser), even small changes in the reflectance could result in large changes in the optical output and mode structure of the laser device [73].

It is also noted that the weak optical response from the DBR would be favourable for some applications. For example, it was recently proposed that strong photon-phonon interactions in optical microcavitites formed using DBRs can be used for light modulation in optoelectronic devices [59, 73–75]. In this case the modulation takes place in the cavity layer and any acousto-optic effects in the DBRs should be minimal. On the other hand, a DBR with high photoelastic constants could be used for efficient modulation and clocking of the optical signals. The important difference between homogeneous films and DBRs is that it would be possible to generate higher acoustic harmonics using DBRs. Therefore, the approach presented in this work may be applied to the engineering of various nanophotonic devices based on DBRs where efficient GHz modulation of light using acousto-optical effects is required.

It is clear polymer structures such as this provide an interesting avenue for further research in this area. Understanding the nature of the acousto-optical interactions in such polymer multilayers and the importance of the photoelastic effect as structures such as this are subject to strain pulses is the key result of the work in this chapter.

6. Capillary instabilities in floated annuli

6.1 Introduction

Wrinkling in thin films is a common phenomenon in the world around us. From human skin, to dried fruit and through to the wrinkles on the coagulated protein layer that forms when one heats milk, when a thin film is stretched or strained it tends to buckle and bend [76].

Wrinkling, or bending out of the plane of a sheet, can occur when it lowers the elastic energy required to stretch the sheet along its plane. Stretching a sheet along its plane in one direction will generate in plane strains in an orthogonal direction via the Poisson effect. Beyond some critical strain the sheet will buckle to accommodate this [77]. This typically leads to wrinkling occurring in a direction orthogonal to the applied strain.

Figure 6.1: Wrinkles formed by skin around the eye being stretched.

Previous work has considered such wrinkling generally by minimising the total elastic energy stored in the film at a given strain [76, 77]. This leads to scaling relationships between the amplitude and wavelength of the wrinkles. These arguments have been applied in a variety of contexts, in particular the study of artificial skins [78] and scars [79].

Understanding the reasons for wrinkles forming may be of interest in preventing them when they are not desired but also for useful applications such as guiding the assembly of materials or fabrication of various functional devices including optical gratings or channels for microfluidic devices [78]. Knowledge of the physics of wrinkling could also potentially help to measure otherwise hard to access properties, such as the elastic modulus of thin films. Indeed, it is precisely this that is the goal of the work reported this chapter.

There are obviously many ways to strain thin films. In biological or soft materials, however, the films are often in a fluid environment. This work is similar in that it deals with films floated on a water surface. To understand these cases then, an understanding of thin film wrinkling due to capillary or surface tension forces is needed.

One relevant effort to achieve this has been carried out by Huang *et al* [80]. They floated ultra-thin (∼30-230 nm) polystyrene (PS) films on to water, where the surface tension of the water-air interface around the perimeter of the films initially pulled them flat. By placing drops of water on top of the films, they were able to induce a radial pattern of wrinkles around the droplet.

This pattern was reproducible, and by determining scaling laws for the number and length of the wrinkles related to the size of the droplets and the thickness of the polymer film, Huang *et al.* were able to show that either the thickness or elastic modulus of the films could be extracted thus opening up the possibility of using capillary wrinkling as a simple method for measuring the elastic properties on ultra-thin polymer films.

In order to controllably study capillary instabilities such as this, and to accurately characterise parameters such as the critical strain at which wrinkling occurs, it is desirable to develop a method where the strain can be modified dynamically for a single film. The work in this chapter details

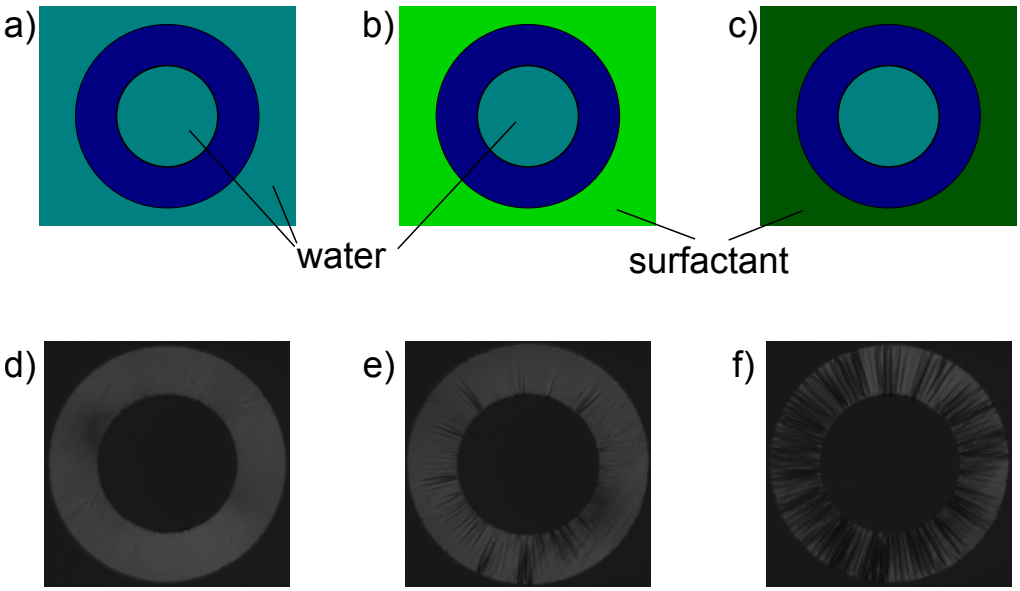

Figure 6.2: This figure shows schematically the technique used to induce wrinkling in ultrathin polymer films. A polymer annulus is floated on to a water surface on a Langmuir-Blodgett (LB) trough, forming a barrier (a & d). Surfactant is placed around the outside of the annulus but does not penetrate in to the centre, creating a surface tension difference between the inner and outer edges, at a certain point this induces wrinkling (b & e). The barriers of the LB trough can then be moved in, increasing the concentration of the surfactant and further lowering the surface tension outside the annulus. This increases the number of wrinkles (c & f). Images d,e and f are photographs taken of annuli during the process, this is discussed in more detail in the following sections.

efforts to achieve this, using ultra-thin, floated, polymer annuli on a water surface in a Langmuir-Blodgett trough.

By placing surfactant around the outside of the annulus, which forms a barrier to surfactant at the surface, a surface tension difference between the inner and outer perimeters of the film can be controlled by moving the trough barriers in and out. This in turn results in compressive forces and a strain being applied to the film, eventually causing wrinkling to occur. This process is summarised in Figure 6.2.

A similar technique was recently detailed by Piñeirua *et al.* [81], all be it for much larger, thicker annuli than those considered here. Rather than polystyrene, their annuli were cut from spin coated sheets of polyvinylsiloxane, and were of thicknesses between 16 and 110 μm.

It should be noted that due to the larger size of their annuli, Piñeirua *et al.* concluded that gravitational forces had a significant effect of the wavelength of wrinkles formed, rather than the purely capillary driven behaviour expected for ultra-thin films.

The work here can be viewed as a combination of the previous techniques described. That is, using the controllable, reversible annulus method but on films in the ultra-thin regime ($<$ 200 nm). The main goal of this initial work was to assess the validity of this technique in studying the elastic properties of ultra-thin polymer films as well as developing a theory that allowed for the elastic modulus of the films to be extracted.

There is great interest in investigating and measuring the elastic moduli of ultra-thin polymer films, as this quantity strongly affects how they behave under stress or strain, for example in the acoustic measurements in the previous two chapters. This in turn has implications on their use for designing and manufacturing the wide range of potential devices as mentioned in Chapter 1.

In addition, there is further interest of the elastic and mechanical prop-

erties of polymer films with thicknesses approaching the rms end to end distance, R_{rms}. Polymer films with thicknesses on this scale result in the polymer chains being strongly confined and have displayed effects such as deviations in the glass transition temperature [82]. Understanding how the elastic properties of the film behave in this regime is an intriguing prospect.

In particular, there is interest in how the elastic moduli of an ultra-thin polymer films deviates from the bulk as the thickness of the film approaches zero. Previous studies have shown that the moduli tends to decrease as the film thickness approaches ∼30 nm, although the onset of this deviation is dependant on the polymer [83, 84]. These techniques used wrinkling instabilities, induced by straining a stiff polymer film such as PMMA on a soft substrate such as PDMS [85]. The technique discussed in this chapter has the potential to provide a complementary method to directly measure the elastic moduli of polymer thin films.

This chapter deals with the progress made towards using this technique for consistent measurements of ultra-thin polymer films. A theory is presented to describe the onset of wrinkling at a critical surface pressure difference, that is the difference between the surface tension inside and and outside the annulus, as a function of the annulus dimensions. The growth in the number of wrinkles as a function of surface pressure difference is also related to the elastic modulus and annulus dimensions.

Details of the method and techniques used in analysis of the wrinkles are presented as well as a discussion of the current limitations of the theory and avenues for future work.

6.2 Theory

This section contains the details of the model proposed to describe the wrinkling behaviour of the floated annuli under study. To describe the behaviour expected, two expressions are initially needed: one for the strain energy stored in an annulus under compression and one for the work done by bending stresses during wrinkling.

The total change in elastic energy is the sum of these quantities and by minimising this value, an expression for the number of wrinkles formed as a function of the net stress applied to the annulus can be calculated. It is helpful first to be reminded of the situation being considered, as shown in Figure 6.3.

A polystyrene (PS) annulus which is of the order of a centimetre in external radius, but with a thickness of the order of a hundred nanometres is floated on to a bath of distilled, deionised water in a Langmuir-Blodgett (LB) trough. Surfactant is dropped around the outside of the annulus at a low concentration so that it forms a layer at the surface of the water. The annulus then acts as a barrier to this surfactant.

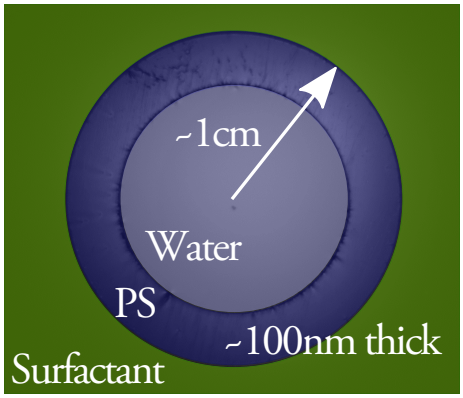

Figure 6.3: An image of a typical thin films annulus of PS with an inner radius of 6.2 mm, an outer radius of 8.8 mm and a thickness of 131 nm.

By moving the barriers on the LB trough, the concentration of the surfactant outside the annulus is increased, lowering the surface tension. At the same time, the surface tension inside the annulus has a value close to that of pure water. This results in a

net compressive stress on the inner edge of the annulus. Past a certain value of this net stress, the annulus wrinkles in a radially symmetric pattern.

As the thickness of the annulus, h, is much smaller than the in plane dimensions, we have the conditions of plane strain and can describe the system using cylindrical coordinates where the vertical component of the displacement, $\mathbf{u}$, is zero i.e. $u_z = 0$. The first task is to find solutions for the displacement and stress fields in the annulus.

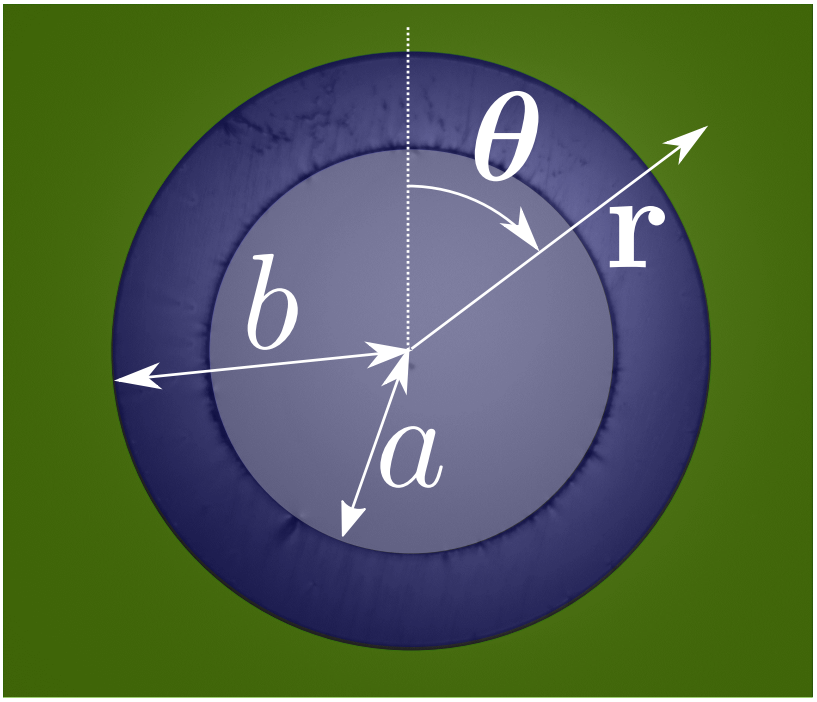

Figure 6.4: An image showing the dimensions used to label the annuli. The two coordinate directions, $\mathbf{r}$ and $\boldsymbol{\theta}$, are labelled. The inner and outer annulus radii are labelled a and b respectively. The thickness is not shown but is labelled h.

The coordinate system and the main in plane annulus dimensions, the inner, a, and outer, b, radii, are shown in Figure 6.4. Defining traction vectors, $\hat{\mathbf{t}}$ similar to Slaughter [86], $\hat{\mathbf{t}} = \hat{\mathbf{n}}\sigma_{\mathbf{rr}}$, where $\hat{\mathbf{n}}$ is the normal vector to an edge of the annulus and σ_{rr} is the radial component of the stress field

we can write the following boundary conditions:

$$\sigma_{rr}(r = a) = \sigma_1 \tag{6.1}$$

$$\sigma_{rr}(r = b) = \sigma_2 \tag{6.2}$$

where σ_1 and σ_2 are the stresses acting on the inside and outside the annulus respectively. This is shown schematically in Figure 6.5.

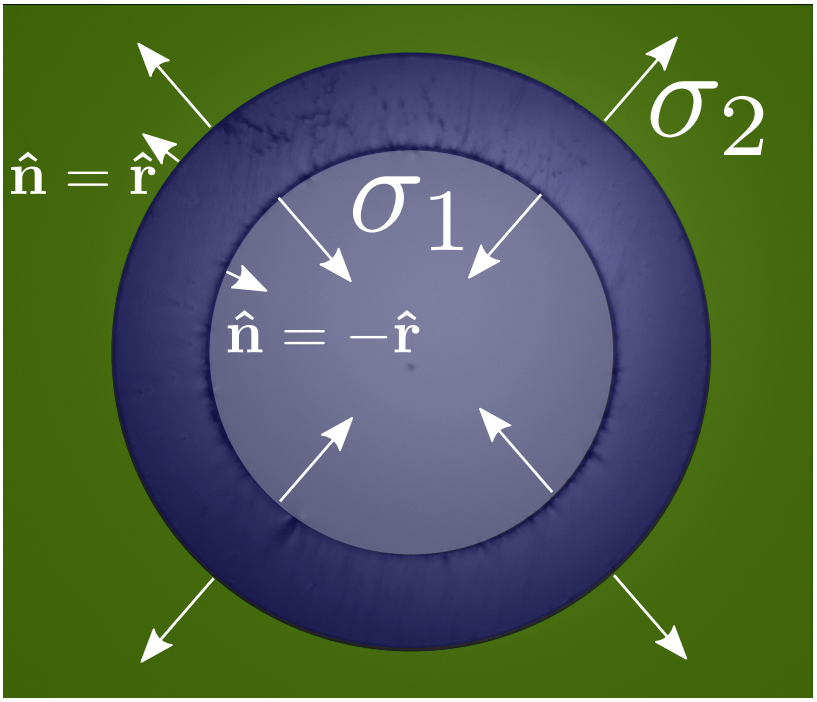

Figure 6.5: An image showing the stresses inside (σ_1) and outside (σ_2) the annulus, as well the definition of the normal vectors, $\hat{\mathbf{n}}$, at each edge with respect to the unit radial vector, $\hat{\mathbf{r}}$.

Assuming that the displacement field in the annulus has the form $\mathbf{u} = u_r\hat{\mathbf{r}} + u_\theta\hat{\boldsymbol{\theta}}$ we can write the strain components, ϵ_{ij}, as so:

$$\epsilon_{rr} = \frac{\partial u_r}{\partial r} \tag{6.3}$$

$$\epsilon_{\theta\theta} = \frac{1}{r}\left(\frac{\partial u_\theta}{\partial \theta} + u_r\right) \tag{6.4}$$

$$\epsilon_{r\theta} = \frac{1}{2}\left(\frac{1}{r}\frac{\partial u_r}{\partial \theta} + \frac{\partial u_\theta}{\partial r} - \frac{u_\theta}{r}\right) \tag{6.5}$$

We can write the stress field components, σ_{ij}, in terms of the strain using the Lamé constants (μ and λ) like so: $\sigma_{ij} = 2\mu\epsilon_{ij} + \lambda(\epsilon_{rr} + \epsilon_{\theta\theta})\delta_{ij}$. Thus we obtain:

$$\sigma_{rr} = 2\mu\epsilon_{rr} + \lambda(\epsilon_{rr} + \epsilon_{\theta\theta}) \tag{6.6}$$

$$\sigma_{\theta\theta} = 2\mu\epsilon_{\theta\theta} + \lambda(\epsilon_{rr} + \epsilon_{\theta\theta}) \tag{6.7}$$

$$\sigma_{r\theta} = 2\mu\epsilon_{r\theta} \tag{6.8}$$

Now taking the equations for plane stress elasticity [86]:

$$\frac{\partial\sigma_{rr}}{\partial r} + \frac{1}{r}\frac{\partial\sigma_{r\theta}}{\partial\theta} + \frac{1}{r}(\sigma_{rr} - \sigma_{\theta\theta}) = 0 \tag{6.9}$$

$$\frac{\partial\sigma_{r\theta}}{\partial r} + \frac{1}{r}\frac{\partial\sigma_{\theta\theta}}{\partial\theta} + \frac{2}{r}\sigma_{r\theta} = 0 \tag{6.10}$$

These can be rewritten in terms of strain using equations 6.6-6.8. We may also assume that the displacement field solution exhibits the same cylindrical symmetry as the the problem, i.e. $u_r = U(r)$, $u_\theta = 0$. Thus we can rewrite equations 6.3-6.5:

$$\epsilon_{rr} = \frac{\partial U}{\partial r} = U' \tag{6.11}$$

$$\epsilon_{\theta\theta} = \frac{U}{r} \tag{6.12}$$

$$\epsilon_{r\theta} = 0 \tag{6.13}$$

Using equations 6.11-6.13 and equations 6.6-6.8, the left hand side of equation 6.10 trivially becomes zero and we may rewrite equation 6.9:

$$r^2U'' + rU' - U = 0 \tag{6.14}$$

This is an Euler-Cauchy equation and has a general solution of the form:

$$U(r) = Br + \frac{C}{r} \tag{6.15}$$

where B and C are some constants to be determined.

Now, we rewrite equation 6.6 using equations 6.11 and 6.12:

$$\sigma_{rr} = 2\mu U' + \lambda\left(U' + \frac{U}{r}\right) \tag{6.16}$$

Remembering our boundary conditions, equations 6.1 and 6.2, and using the general solution of $U(r)$, equation 6.15, we can thus write a pair of simultaneous equations:

$$2(\mu+\lambda)B - \frac{2\mu}{a^2}C = \sigma_1 \tag{6.17}$$

$$2(\mu+\lambda)B - \frac{2\mu}{b^2}C = \sigma_2 \tag{6.18}$$

Solving these gives expressions for B and C in terms of a, b, σ_1, σ_2, μ and λ. Inserting these in to the general solution for $U(r)$ we now have the form of the displacement field, $\mathbf{u} = u_r\hat{\mathbf{r}} + u_\theta\hat{\boldsymbol{\theta}}$ where:

$$u_r = \frac{r}{2(\mu+\lambda)}\left(\frac{a^2\sigma_1 - b^2\sigma_2}{a^2-b^2}\right) + \frac{a^2b^2}{2\mu r}\left(\frac{\sigma_1-\sigma_2}{a^2-b^2}\right) \tag{6.19}$$

$$u_\theta = 0 \tag{6.20}$$

We can now also write an expression for the radial component of the stress field by inserting equation 6.19 in to 6.16, to give:

$$\sigma_{rr} = \left(\frac{a^2\sigma_1 - b^2\sigma_2}{a^2-b^2}\right) - \frac{a^2b^2}{r^2}\left(\frac{\sigma_1-\sigma_2}{a^2-b^2}\right) \tag{6.21}$$

Similarly, starting from equation 6.7 we can write the angular component as:

$$\sigma_{\theta\theta} = \left(\frac{a^2\sigma_1 - b^2\sigma_2}{a^2-b^2}\right) + \frac{a^2b^2}{r^2}\left(\frac{\sigma_1-\sigma_2}{a^2-b^2}\right) \tag{6.22}$$

We are now nearly in the position to calculate both the strain energy stored in the annulus under compression, and the work done by bending stresses as we require. First we must define a form for the deflection of

the annulus, w, due to wrinkling. Assuming n wrinkles periodically spaced around the annulus we can use an expression:

$$w = w_0 \cos n\theta \tag{6.23}$$

where,

$$\frac{\partial w}{\partial r} = 0 \tag{6.24}$$

$$\frac{\partial w}{\partial \theta} = -nw_0 \sin n\theta \tag{6.25}$$

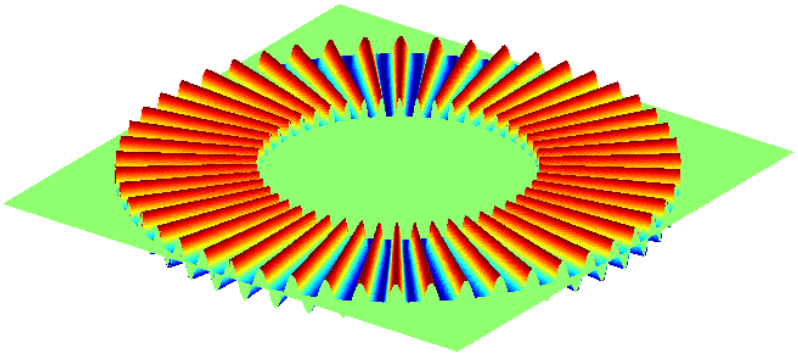

Figure 6.6: A computer generated image of the chosen deflection (equation 6.23) plotted around an annulus for some arbitrary amplitude, w_0. This closely mimics the form of the wrinkles observed on the measured annuli, for example Figure 6.2 f).

Figure 6.6 shows the form of this deflection when plotted around an annulus. It is visually similar to the wrinkles observed on the measured annuli.

Now, we are the position to calculate the desired energies. The strain energy stored in the annulus under compression, ΔU_{strain}, is calculated by integrating the stress field over the annulus given the above deflection [87]:

$$\Delta U_{\text{strain}} = \frac{1}{2} \int_0^{2\pi} \int_a^b \left\{ \sigma_{rr} h \left(\frac{\partial w}{\partial r} \right)^2 + \sigma_{\theta\theta} h \left(\frac{1}{r} \frac{\partial w}{\partial \theta} \right)^2 \right\} r dr d\theta \tag{6.26}$$

Using the expressions for σ_{rr}, $\sigma_{\theta\theta}$ and w we obtain an equation for ΔU_{strain}:

$$\boxed{\Delta U_{\text{strain}} = \frac{\pi h n^2 w_0^2}{4(a^2-b^2)}\left(2\left(a^2\sigma_1 - b^2\sigma_2\right)\ln\left(\frac{b}{a}\right) + \left(b^2-a^2\right)\left(\sigma_1-\sigma_2\right)\right)} \tag{6.27}$$

The work done in bending the plate, ΔU_{bend} can be calculated as [87]:

$$\begin{aligned}\Delta U_{\text{bend}} = \int_0^{2\pi}\int_a^b \Bigg\{ & \frac{D}{2}\left(\frac{\partial^2 w}{\partial r^2} + \frac{1}{r}\frac{\partial w}{\partial r} + \frac{1}{r^2}\frac{\partial^2 w}{\partial \theta^2}\right)^2 \cdots \\ & - D(1-\nu)\frac{\partial^2 w}{\partial r^2}\left(\frac{1}{r}\frac{\partial w}{\partial r} + \frac{1}{r^2}\frac{\partial^2 w}{\partial \theta^2}\right)\cdots \\ & + D(1-\nu)\left(\frac{1}{r}\frac{\partial^2 w}{\partial r \partial \theta} + \frac{1}{r^2}\frac{\partial w}{\partial \theta}\right)^2\Bigg\} r\,dr\,d\theta\end{aligned} \tag{6.28}$$

where

$$D = \frac{Eh^3}{12\left(1-\nu^2\right)} \tag{6.29}$$

and E is the Young's modulus and ν is the Poisson ratio of the annulus.

Using the expressions for D and w an equation for ΔU_{bend} is obtained:

$$\boxed{\Delta U_{\text{bend}} = \frac{D\pi n^2 w_0^2}{4}\left(\frac{b^2-a^2}{a^2 b^2}\right)\left(n^2 - 2(1-\nu)\right)} \tag{6.30}$$

The next step is to find an expression for the expected number of wrinkles, n. To do this, we must find the equilibrium state of the annulus by minimising the total energy, $\Delta U = \Delta U_{\text{strain}} + \Delta U_{\text{bend}}$. That is, when:

$$\frac{d(\Delta U)}{dn} = 0 \tag{6.31}$$

Using equations 6.27 and 6.30 we get:

$$\begin{aligned}\frac{d(\Delta U)}{dn} &= D\pi n^3 w_0^2 \left(\frac{b^2-a^2}{a^2b^2}\right) - D\pi n w_0^2 \left(\frac{b^2-a^2}{a^2b^2}\right)(1-\nu)\ldots \\ &+ \frac{\pi h n w_0^2}{2(a^2-b^2)}\left(2\left(a^2\sigma_1 - b^2\sigma_2\right)\ln\left(\frac{b}{a}\right) + \left(b^2-a^2\right)(\sigma_1-\sigma_2)\right) \\ &= 0 \end{aligned} \tag{6.32}$$

There are two solutions to this. One where $n = 0$, i.e. wrinkles of infinite wavelength, that corresponds to the entire annulus buckling inwards, or one where there is a finite number of wrinkles:

$$n^2 = (1-\nu) - \frac{h}{2D}\left(\frac{a^2b^2}{a^2-b^2}\right)\left(\frac{2(a^2\sigma_1 - b^2\sigma_2)\ln\left(\frac{b}{a}\right)}{b^2-a^2} + (\sigma_1-\sigma_2)\right) \tag{6.33}$$

At this point, it is important to make the distinction between the stresses acting on the annulus, σ_1 and σ_2, which have been used so far, and the quantity that is measured in the experiment.

The LB trough was equipped with a Wilhelmy plate, positioned outside the annulus, that measured a surface tension difference relative to the pure water sub-phase. This surface tension difference, labelled Π, is calculated as:

$$\Pi = \gamma_1 - \gamma_2 = \frac{\sigma_1}{h} - \frac{\sigma_2}{h} \tag{6.34}$$

where γ_1 and γ_2 are the surface tensions of the liquid inside and outside the annulus respectively.

Using this notation, we are now able to write an expression for the number of wrinkles as a function of the measured surface tension difference:

$$\boxed{n^2(\Pi) = 2(1-\nu) - \frac{2}{D}\left(\frac{a^2b^2}{a^2-b^2}\right)\left(\frac{((a^2-b^2)\gamma_1 + b^2\Pi)\ln\left(\frac{b}{a}\right)}{b^2-a^2} + \frac{\Pi}{2}\right)} \tag{6.35}$$

Plotting out equation 6.35 for some typical values we can see that, as expected, there is a well defined value of Π at which the wrinkles begin to

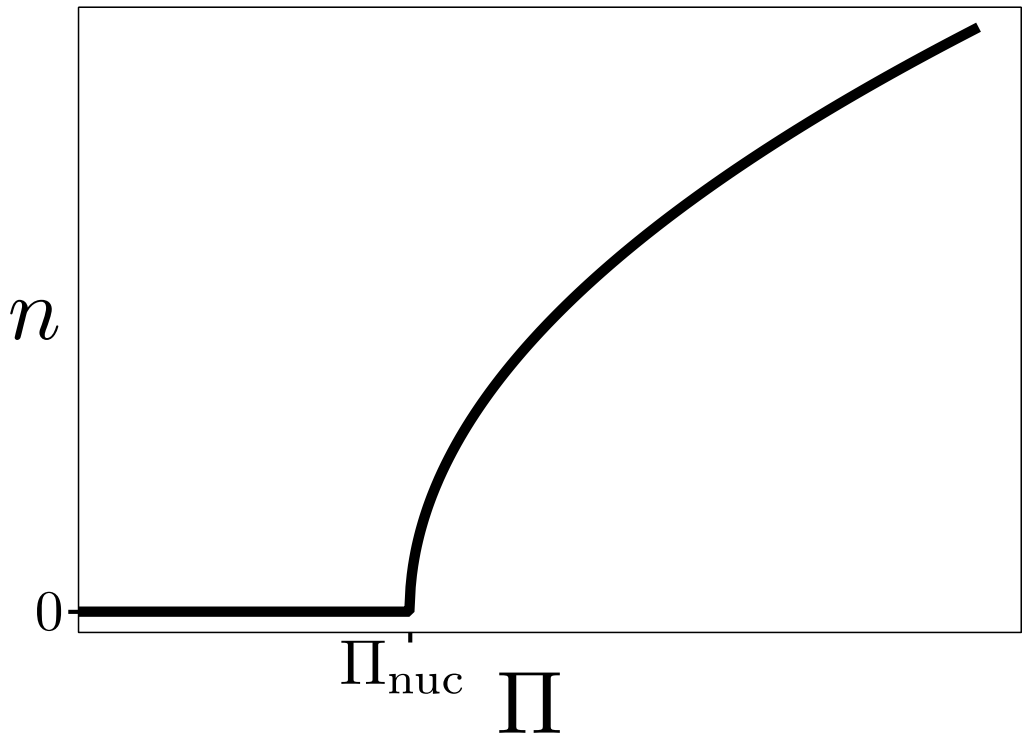

Figure 6.7: A graph showing the form of $n(\Pi)$. It shows that initially, no wrinkles are formed until Π is increased past the threshold nucleation pressure, Π_{nuc}. Past this point they increase quickly, scaling as $\Pi^{\frac{1}{2}}$

nucleate. This is shown in Figure 6.7. We label this the nucleation surface pressure, Π_{nuc}.

This quantity is useful as a test of the validity of the theory so far. If we consider the threshold case: $n^2(\Pi_{\text{nuc}}) = 0$, we can rearrange equation 6.35 to obtain an expression for the nucleation pressure:

$$\Pi_{\text{nuc}} = \frac{\gamma_1 \ln\left(\frac{b}{a}\right) + D(1-\nu)\left(\frac{a^2-b^2}{a^2b^2}\right)}{\left(\left(\frac{b^2}{b^2-a^2}\right)\ln\left(\frac{b}{a}\right) + \frac{1}{2}\right)} \tag{6.36}$$

This expression can be simplified by realising that, for typical values for the annuli studied (a and $b < 1$ cm), the second term in the numerator is $\sim 10^6$ times smaller than the first term. As such it can be considered negligible and so Π_{nuc} can be approximated as a function of the in plane annulus dimensions, a and b, and the surface tension of the sub-phase, γ_1:

$$\Pi_{\text{nuc}} = \frac{\gamma_1 \ln\left(\frac{b}{a}\right)}{\left(\left(\frac{b^2}{b^2-a^2}\right)\ln\left(\frac{b}{a}\right) + \frac{1}{2}\right)} \tag{6.37}$$

It is the case in our experiment that each of these values should be known, as the annulus size is measured and γ_1 should simply be the surface tension of pure water. Thus, we can use a comparison to the nucleation pressure to check that our theory is behaving appropriately.

When considering how to extract the Young's modulus, it is easier to consider n^2 rather than n directly. The form of $n^2(\Pi)$ is shown in Figure 6.8. Calculating the gradient by differentiating equation 6.35 with respect to Π yields:

$$\frac{dn^2}{d\Pi} = \frac{12(1-\nu^2)}{Eh^3}\left(\frac{a^2b^2}{a^2-b^2}\right)\left(\left(\frac{2b^2}{b^2-a^2}\right)\ln\left(\frac{b}{a}\right) + \frac{1}{2}\right) \tag{6.38}$$

This is a function of the annulus dimensions, a, b and h, and the Young's modulus and Poisson ratio, E and ν respectively. This means, that as we know the annulus dimensions, if we know one of the elastic properties we can measure the other directly.

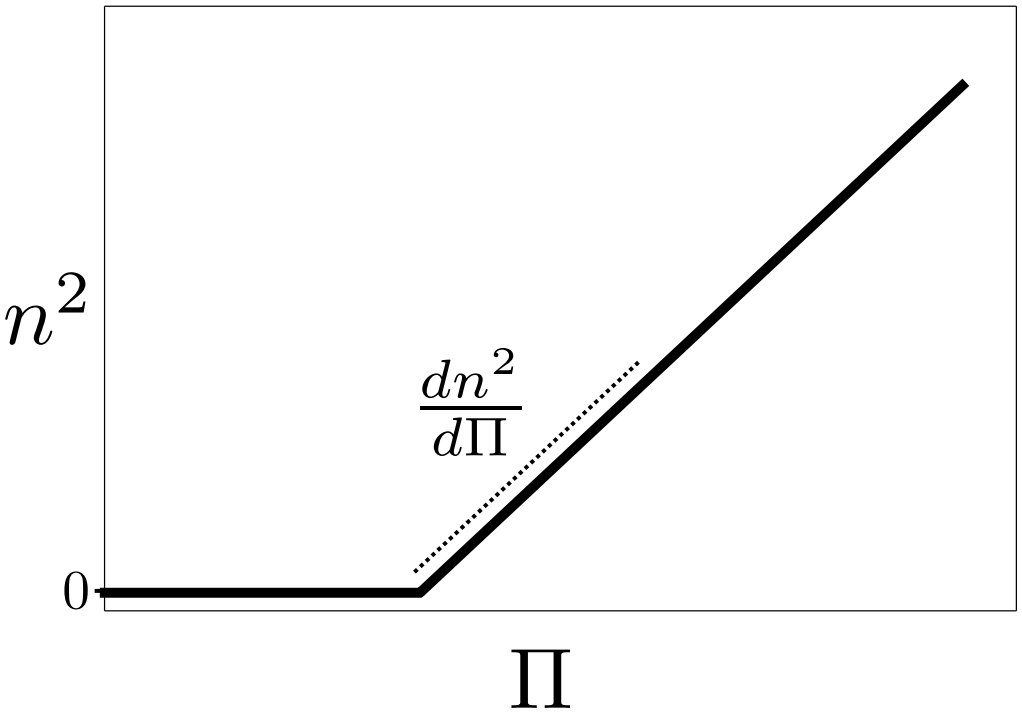

Figure 6.8: A graph showing the form of $n^2(\Pi)$. As before, no wrinkles are formed until Π is increased past the threshold nucleation pressure. Past this point the gradient, $\frac{dn^2}{d\Pi}$, is an important quantity for determining the Young's modulus of the film.

We now have the basis of theory to describe the annulus wrinkling. The next sections will discuss the method and data analysis before discussing how successful the theory is in describing the annulus behaviour.

6.3 Method

The method used for these experiments has already been briefly described, this section will consider the techniques used in more detail.

First, the polymer films were prepared. This consisted of spin coating polystyrene (PS) on to mica wafers. The PS, supplied by PolymerSource, had a M_w of 1,144,000 kDa and a polydispersity (M_w/M_n) of 1.09. Initially, films of a single thickness were required so to spin coat, the polymer was made up to a 2% by weight solution in toluene and a spin speed of 3000 rpm was used.

The films were then annealed under vacuum at 120°C (above the T_g of PS) for one hour to remove any residual solvent. To determine the thickness, the films needed to be transferred to silicon substrates. To do this, sections of the films were cut out by scoring carefully with tweezers. These sections could then be floated on to a bath of distilled, deionised water by slowly immersing the entire sample, lifting the scored section up and leaving it at the surface of the water. Here, they were collected on pieces of polished silicon wafer and studied using ellipsometry (see Section 3.2). Measurements of a selection of films prepared this way gave a consistent thickness of $h = 131 \pm 5$ nm.

The annealing is a key step to remove any residual solvent in the films. Were any left it may change their behaviour once floated on to the LB trough as it would affect the mechanical properties of the film. Annealing the films, however, means that they won't float off glass or silicon substrates without first modifying their surface. It is for this reason that more delicate mica substrates are used as they allow annealed films to float on to a water surface.

To create the annuli, the films, on their mica substrates, were placed back on the spin coater. While being spun at a few thousand rpm, they

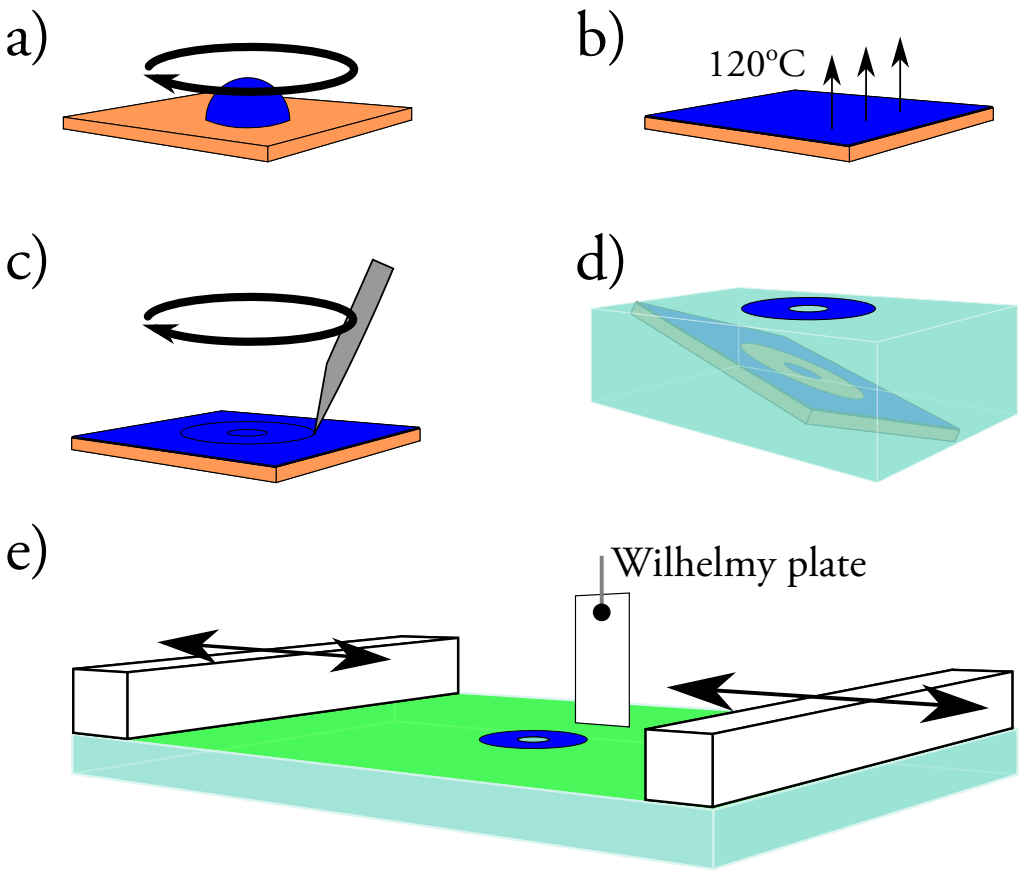

Figure 6.9: The diagram shows schematically how the method progresses. First, a PS in toluene solution in spun on a mica substrate (a) before being annealed in a vacuum oven (b). The sample is placed back on the spin coater and the annulus scored using a sharp pair of tweezers (c). Once the trough is ready, the annulus is floated on to a pure water sub-phase (d). Finally, once the surfactant is added, the surface pressure is controlled by moving the barriers and measured using a Wilhelmy plate (e).

were then scored twice by a pair of sharp tweezers, creating two concentric circular cuts. Care had to be taken not to score through the film and too deep in to the mica as this resulted in edge defects on the annuli as well as increasing their chance of being pinned to the substrate rather than floating off as required, see Figure 6.9.

The LB trough used for the experiments was a commercial model produced by KSV Nima. It had a pair of moving barriers, controlled via an attached PC. Surface pressure measurements were made using the supplied Wilhelmy plate apparatus with plates made in house using chromatograpy paper. In order to prevent the surface pressure reading drifting over time as the plate saturated, all plates were pre-soaked in water from the same supply as that used to fill he trough for at least 2 hours.

Before being filled, the trough was thoroughly cleaned each time using chloroform. Once filled, the barriers were closed and the surface of the water sub-phase 'cleaned' using a small water vacuum pump until the surface pressure reading stabilised. The barriers were then opened and the surface pressure observed. If this didn't change (to within 0.1 mN/m, the resolution of the surface tension measurement) as the barriers opened then the reading was zero'd and the annulus floated on to the trough.

The surfactant used to lower the surface tension outside the annulus was Span 80 (Sigma-Aldrich). A few drops of a dilute aqueous solution of this were dropped in to the trough outside the annulus. At this point, the surface tension outside the annulus could be controlled by moving the barriers in and out. This was measured using a Wilhelmy plate.

In order to check whether or not surfactant was entering the inside of the annulus, a test was conducted by placing the Wilhelmy plate inside an annulus and cycling the barriers in and out. This measurement was performed by Richard Taylor, another student in the group. The annulus used had a large inner radius in order for the Wilhelmy plate to fit. No

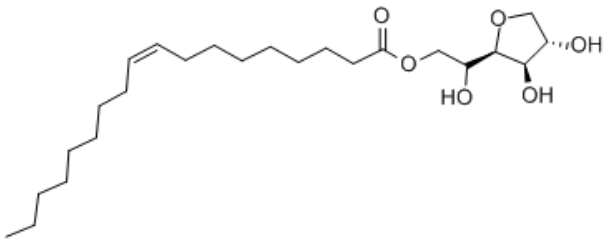

Figure 6.10: The chemical structure of Span 80.

significant change in surface tension was measured, suggesting that the annulus provides an adequate barrier to surfactant layer at the surface of the water until the point that it collapses. A plot of this data is shown in Figure 6.11.

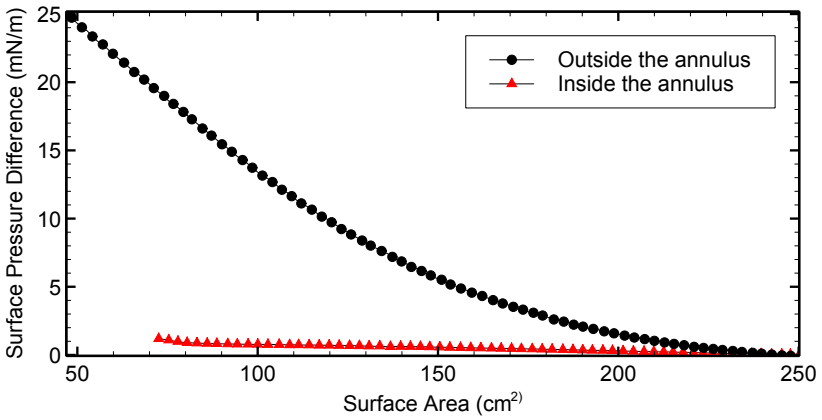

Figure 6.11: A plot of surface pressure difference vs trough surface area, with the Wilhelmy plate placed both inside (red triangles) and outside (black circles) the annulus. This measurement was performed by Richard Taylor, another student in the group. It can be seen that while the surface pressure outside changes significantly as the barriers are moved in (and the area gets smaller), there is little to no change inside the annulus.

The optical set up used to image the annuli is shown in Figure 6.12. The experiment is illuminated by a white LED lamp, diffused through a piece of clouded perspex in order to achieve uniform illumination. A beam splitter is placed on the axis in between the camera and the annulus to light the annulus from above. This means that the wrinkles appear clearly,

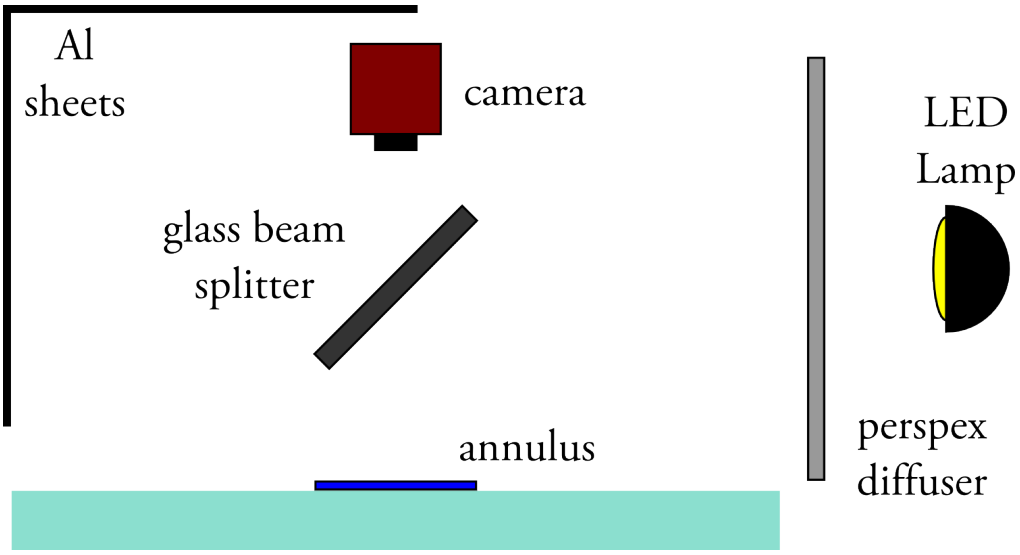

Figure 6.12: This schematic shows the optical set up used to image the annuli while they wrinkled. It relies on the annulus being aligned on the surface of the trough below the camera. As it tended to shift while the barriers are moved it had to be carefully re-centred using tweezers.

rather than casting shadows due to being lit from the side, which would distort their apparent shape.

The camera was a Allied Vision Guppy Pro purchased from Stemmer Imaging. It was controlled via a LabView script that also displayed and recorded the surface pressure when an image was taken. The anodised aluminium sheets were placed to remove any stray reflections from either the LED lamp or the lights in the room.

Examples of the images obtained using this set up are shown in Figure 6.13.

To obtain a set of measurements for an annulus, the surface pressure, Π, was increased in steps of 1-2 mN/m by moving the LB trough barriers until wrinkles started to nucleate. At this point, smaller steps of 0.5 mN/m made, with an image taken at each step.

To extract the number of wrinkles from each image a semi automated process was used. Code written in MATLAB was used to process the

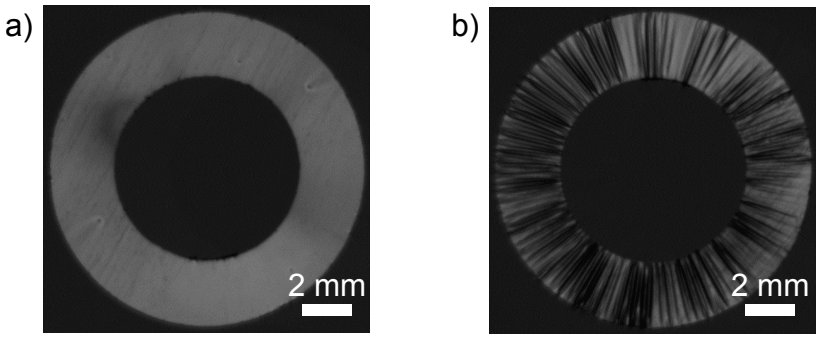

Figure 6.13: Example of the images obtained for a) an unwrinkled annuli and b) a wrinkled annulus after they have been cropped.

images. First, a background image of the trough with no annulus present was subtracted from the images. The images were then binarised at a user defined threshold resulting in an image similar to that shown in Figure 6.14.

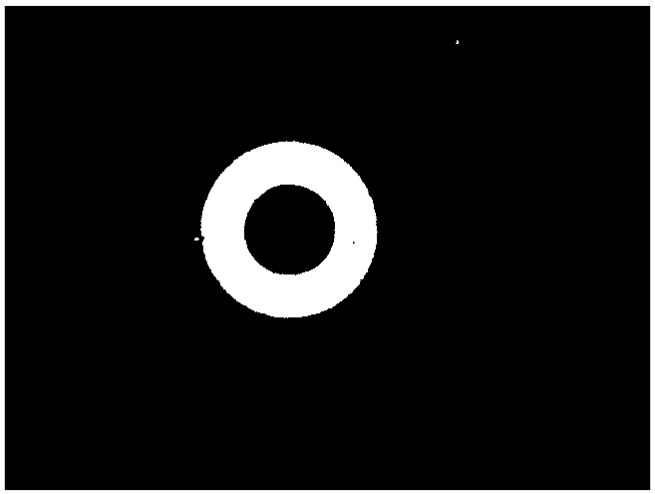

Figure 6.14: Example of the result obtained after removing the background and thresholding an image.

The position and size of the annulus was then registered so it could be centred and the image cropped to include just the annulus. This was performed using MATLAB's `imfindcircles` function, part of the image

processing toolbox, that uses a circular Hough transform to find circular shapes in a given image.

Once the position of the annulus was determined, this was used to crop the original, non-binarised image to just show the annulus, as seen in Figure 6.13. The size of the annulus was calculated using a calibration image, obtained by imaging a ruler placed at the position of the annulus.

Once the appropriate section of the image has been cropped, with the annulus centred, a radial average intensity is calculated. To do this, the program draws a series of circles with radius values between the inner and outer edges of the annulus. The intensity values of circles are added up at each angle and used to produce a plot of average intensity vs angle around the annulus.

In a wrinkled annulus, the tops of wrinkles appear bright whereas the troughs appear darker. Wrinkles are then apparent as peaks in the radial average intensity plot. By identifying these peaks by finding local maxima in this plot, the number and position of wrinkles could be determined.

This method is mostly effective, correctly identifying $>80\%$ of wrinkles automatically. The sensitivity depends on the threshold at which a peak is declared in the radial average intensity plot. To ensure that an accurate count of wrinkles was achieved, this threshold could be adjusted manually by the user.

Typically, when analysing an image, the threshold value was increased until no false positive peaks were observed. Any wrinkles that were missed (false negatives) could then be tagged manually. By using this two stage process, an accurate count of the wrinkles could be made in a reasonable time frame.

We will now move on to consider some of the results obtained using this method.

6.4 Results & Analysis

This section contains examples of the results obtained using the methods laid out in the previous section. Details of how the nucleation pressures, Π_{nuc}, and the wrinkling gradient, $\frac{dn^2}{d\Pi}$, are obtained are also given.

For a typical measurement, as predicted by the theory contained in Section 6.2, no wrinkles are initially present on the annulus as the surface pressure Π is increased. Past a certain point, the wrinkles nucleated and then increased in number rapidly, again in agreement with the theory.

Figure 6.16 shows the typical evolution of the wrinkles on an annulus as the surface pressure is increased. Initially, the annulus is flat. As the nucleation pressure is reached a few wrinkles can be seen starting to grow in. The number and extent of these increases as the surface pressure difference is increased.

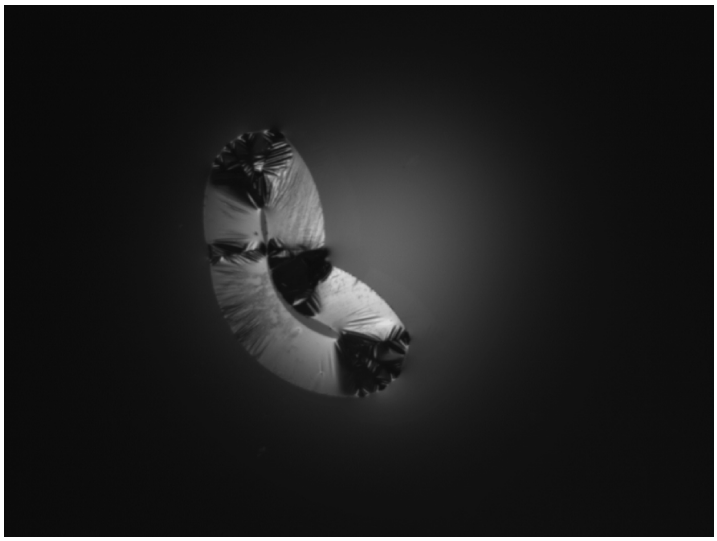

Figure 6.15: An example image of an annulus that has collapsed in on itself as the surface pressure difference became too large.

It can be seen that although the wrinkles initially nucleate at only a few points, they are soon distributed around the entire circumference of the annulus. In the case where there was some irregularity or edge defect,

the annulus tended to wrinkle only at this point, resulting in only a few wrinkles whose amplitude increased with surface pressure, rather than the behaviour seen opposite.

The final image in the series (Π = 30 mN/m) shows the annulus is almost entirely saturated with wrinkles. When the barriers were brought in and Π increased one more step the annulus collapsed in on itself, irreparably damaging it, as seen in Figure 6.15. Each measurement was performed until this occurred.

Once a set of images, such as that shown in Figure 6.16 was obtained, the number of wrinkles in each image was extracted via the process described in the previous section. An example of the resulting plots is shown in Figure 6.17.

This plot shows the number of wrinkles at each surface pressure for the same annulus as shown in Figure 6.16. It is similar to the form predicted for the number of wrinkles versus surface pressure (Figure 6.7).

The next step was to check whether our theory correctly predicts the nucleation pressures and wrinkling gradients of the annuli. To do this, series of annuli where the only parameter altered was the inner radius were made and measured. Due to the process by which the annuli were cut, there is still some small variation in the outer diameters ($\sim$ 0.5 mm). For ease, the data sets are referred to using an average value of the outer radius.

The two sets of data collected were for $\bar{b} = 8.6 \pm 0.4$ mm and $\bar{b} = 6.2 \pm 0.6$ mm. These are shown in Figure 6.18 and Figure 6.19 respectively. Data for each annulus is plotted in a different colour with different shaped data points. The inner and outer dimensions of the annuli are listed, in general, with increasing width $(b - a)$ from top to bottom.

In both plots, it can be seen that the wider annuli (larger $b - a$) appear to have higher nucleation pressures. That is, it is harder to get them to buckle. Intuitively, one would expect this, as it takes more energy to buckle

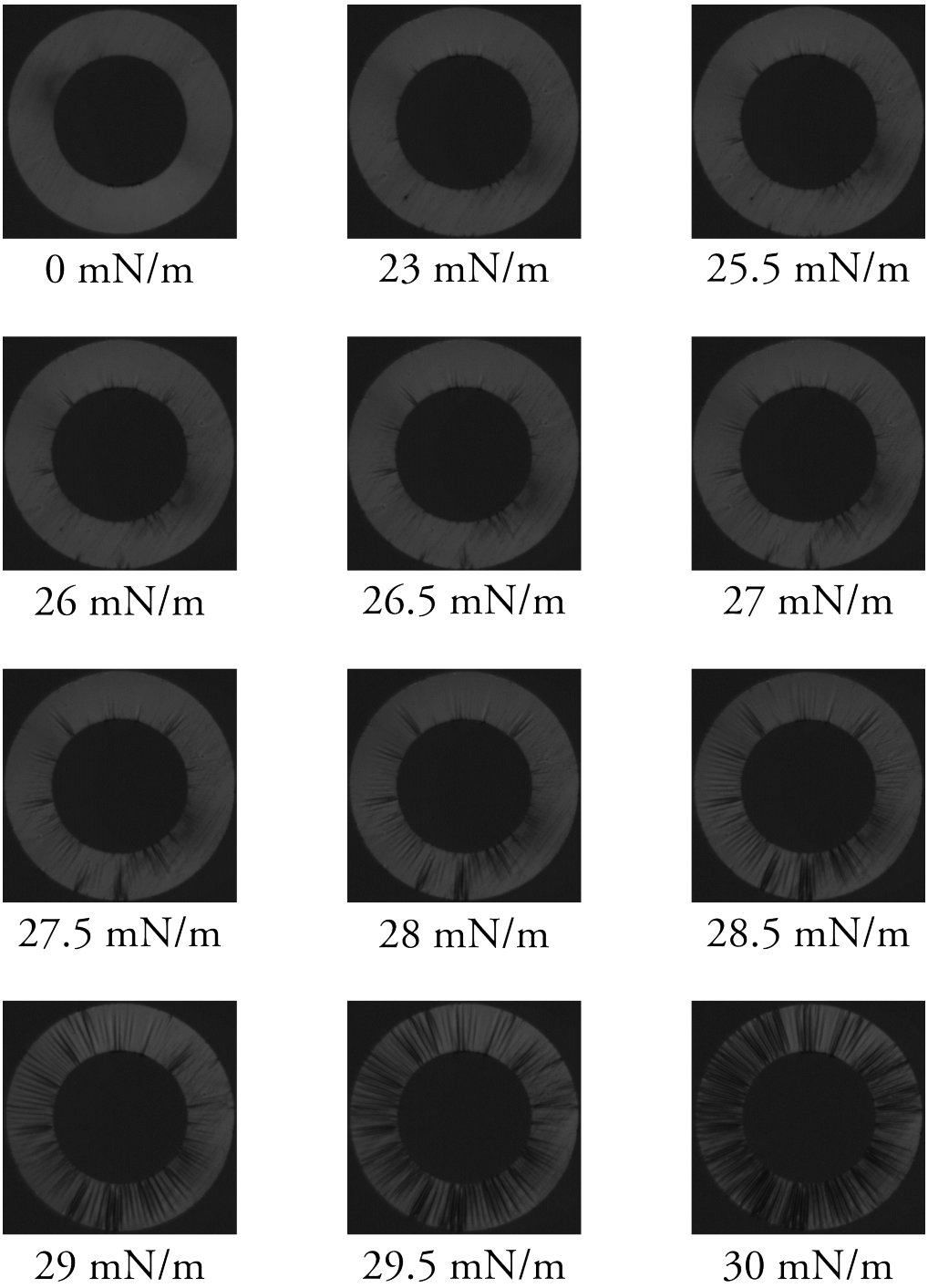

Figure 6.16: A set of images for an annulus with dimensions $a = 3.6$ mm, $b = 6.3$mm. The surface pressure is labelled under each image, increasing left-to-right, top-to-bottom.

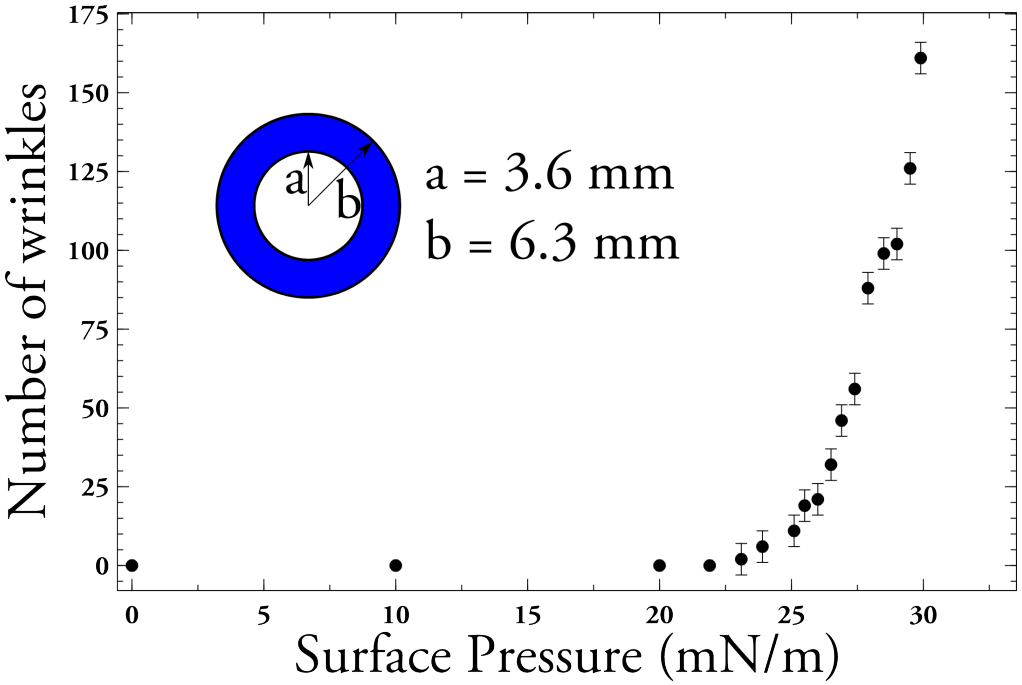

Figure 6.17: The result of the analysis for the number of wrinkles performed on the set of images shown in Figure 6.16. The error bars are ±5 wrinkles. These were chosen based on comparing counts done entirely manually with the part automated count used.

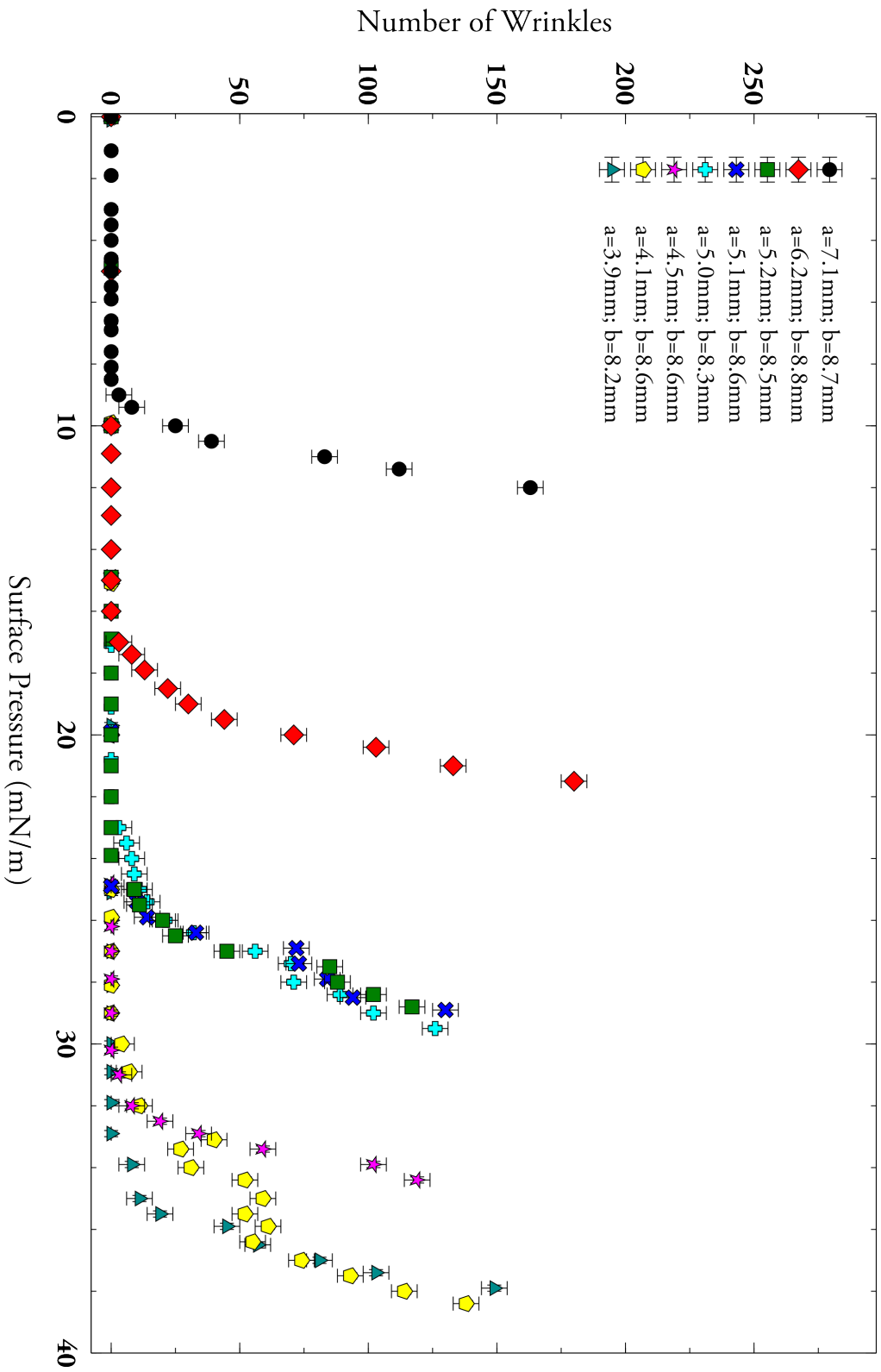

Figure 6.18: The combined data for annuli with $\bar{b} = 8.6$ mm.

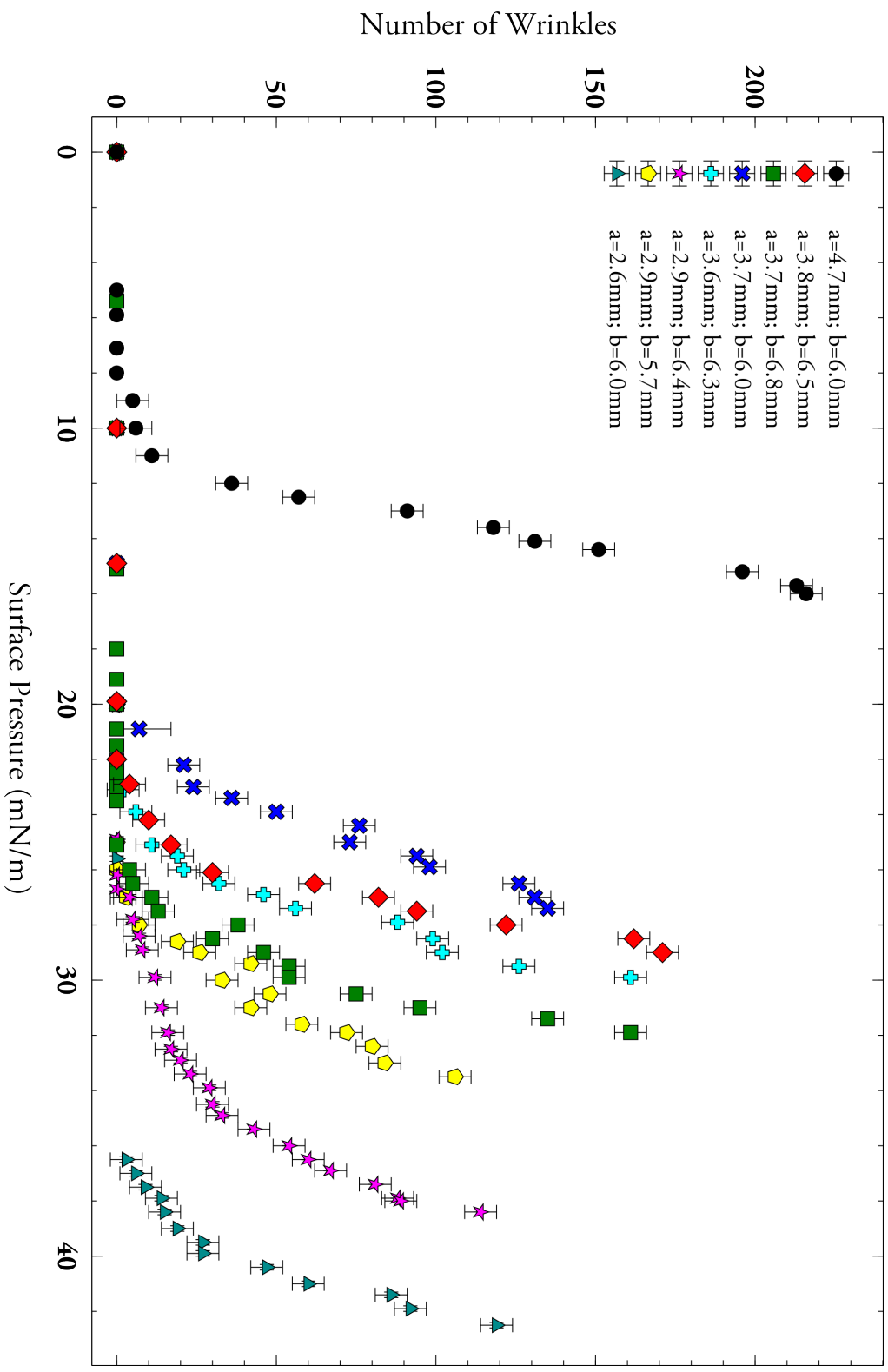

Figure 6.19: The combined data for annuli with $\bar{b} = 6.2$ mm.

a wider plate.

In Figure 6.18, there were three almost identical annuli (green squares, blue x's, turquoise crosses) measured. The data points for each of these annuli sit on top of each other. This confirms that the measurements are reproducible.

While it appears that there are some variations in wrinkling gradient in the data presented, it is hard to assess these by looking at the raw data. To obtain these, as well as accurate values for the nucleation pressures, linear fits were made to the data.

An example of how the fits are made is shown in Figure 6.20. It is worth noting that the fit is made to square of the number of wrinkles, that is: n^2 versus Π. This is for ease when calculating the Young's modulus from the gradients, see Equation 6.38.

The nucleation pressures, Π_{nuc}, were calculated as the x-intercept of these fits. This value was used rather than simply taking the first pressure at which wrinkles occur as identifying wrinkles at the point where they are just starting to nucleate was somewhat arbitrary. By using this fitting method, more data could be taken in to account, increasingly the reliability of this measurement.

In order to check whether the annuli were in fact being deformed elastically, rather than suffering a plastic deformation, a measurement was performed where an annulus was wrinkled close to saturation but not to the point of collapse. The barriers on the LB trough were then stepped back out, decreasing the surface pressure, with the number of wrinkles being counted at each step as before.

The results of this test are shown in Figure 6.21. It can be seen that the variation in the number of wrinkles doesn't change as the surface pressure difference changes when the barriers are cycled in and out, it is only a

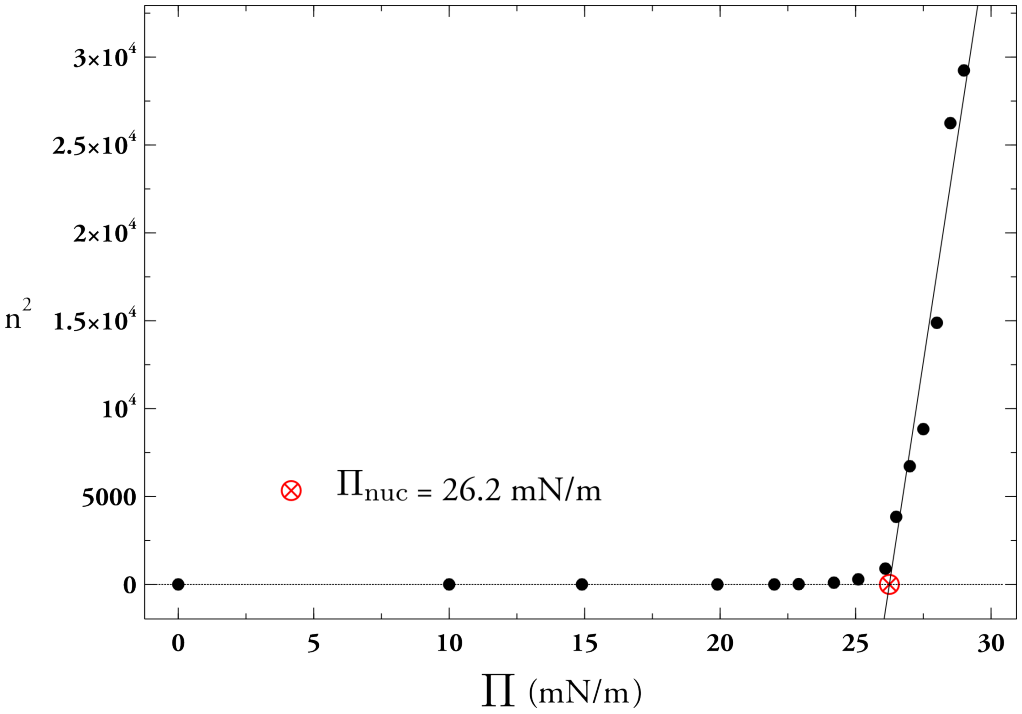

Figure 6.20: A plot showing an example linear fit to the wrinkled part of a plot of n^2 vs Π. This is for the same annulus as Figures 6.16 and 6.17.

function of the surface pressure, strongly suggesting that the wrinkling is elastic in nature.

The data has been presented and qualitatively appears to behave as expected. Using the fitting procedure presented above, we can extract the values needed to check the theory. It is, therefore, time to conduct a more quantitative discussion as to the success of the experiment and the theory used to describe it.

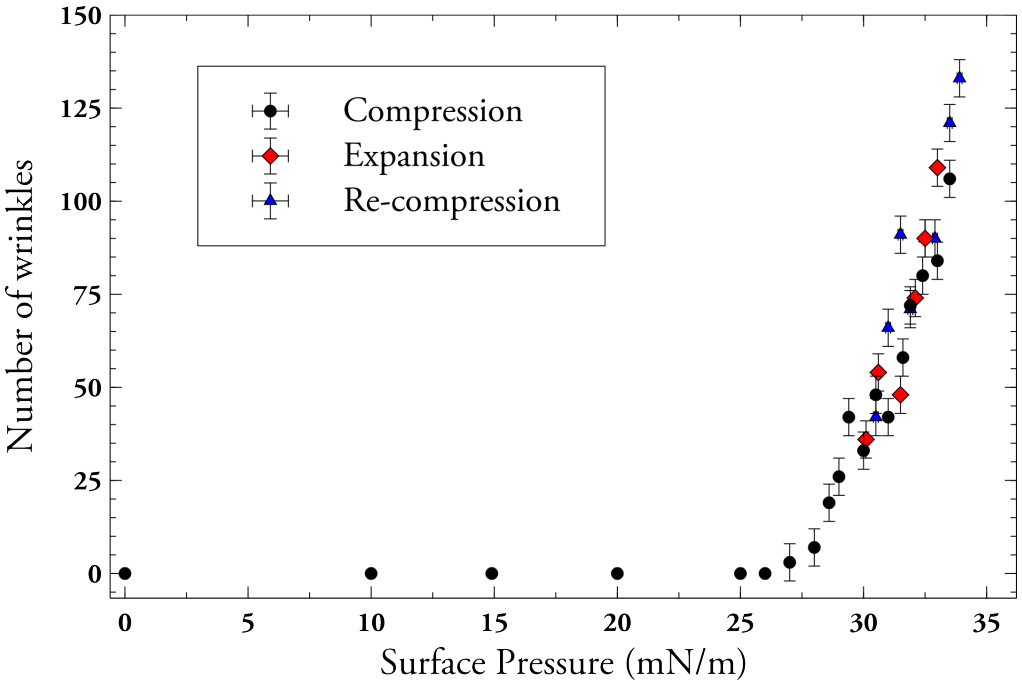

Figure 6.21: A plot showing the results of cycling the barriers in and out, 'compression' and 'expansion' respectively. The annulus shown here had the dimensions: $a = 2.9$ mm, $b = 5.7$mm.

6.5 Discussion

This section contains a quantitative discussion of the data and the success of the described theory in explaining it.

First, we will look at the nucleation pressures, Π_{nuc}. Recalling the expression for Π_{nuc} (Equation 6.37):

$$\Pi_{\text{nuc}} = \frac{\gamma_1 \ln\left(\frac{b}{a}\right)}{\left(\left(\frac{b^2}{b^2-a^2}\right)\ln\left(\frac{b}{a}\right)+\frac{1}{2}\right)}$$

As we know all the parameters for each annulus, we can compare the measured values of Π_{nuc} with theoretical ones given by our equation. The results of this comparison are shown in Figure 6.22. The main theoretical lines are calculated for the appropriate value of $\bar{b}$ for each set. The bounds are calculated using the minimum and maximum values of b in each set.

γ_1 is the surface tension of the sub-phase. This is expected to be pure water, hence a value: $\gamma_1 = 72$ mN/m was used.

The vertical error bars are the standard error in Π_{nuc} calculated from the confidence bounds given by the fits such as that shown in Figure 6.20. The horizontal error bars take in to account the uncertainty in determining a from the images.

There is good agreement between the theoretical prediction and the measured data. The majority of the data points lie in the bounds predicted by the theory. This is encouraging as it suggests that the theory is adequate for predicting the nucleation pressures.

It is useful to present the data in such as way that it can be collapsed on to a master curve. In order to do this we can rewrite Equation 6.37 in terms of a single parameter containing the annulus dimensions as so:

$$\Pi_{\text{nuc}} = \gamma_1 X \tag{6.39}$$

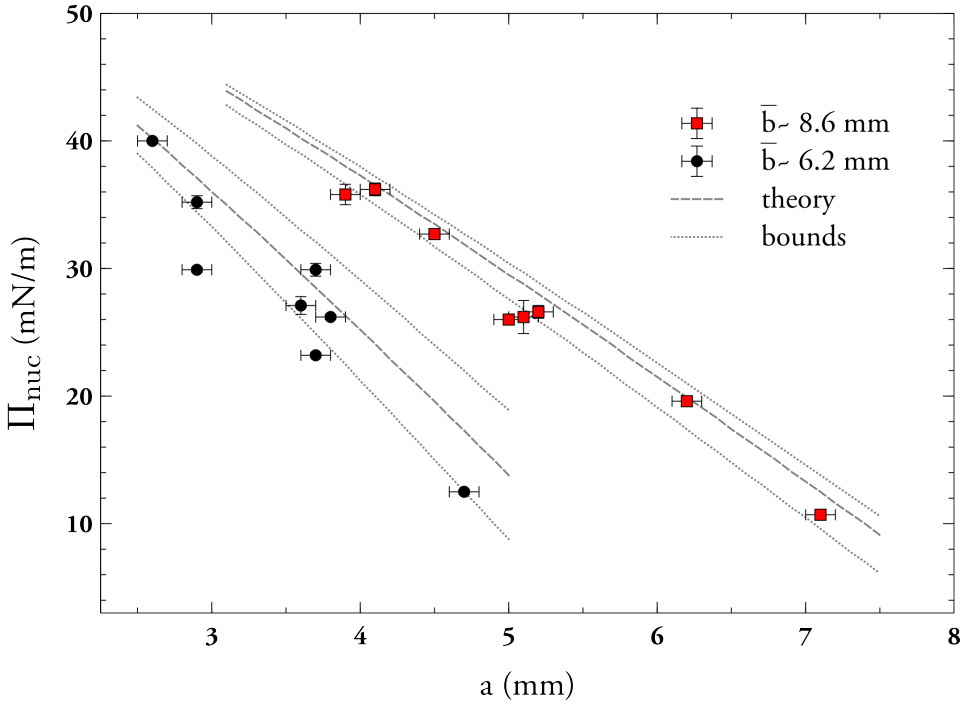

Figure 6.22: A plot showing the measured nucleation pressures of the annuli as a function of their inner radii for the two data sets. Also shown for each set, are a theoretical line for the appropriate value of $\bar{b}$ as well as bounds related to the minimum and maximum values of b in each set.

where:

$$X = \frac{\ln\left(\frac{b}{a}\right)}{\left(\left(\frac{b^2}{b^2-a^2}\right)\ln\left(\frac{b}{a}\right)+\frac{1}{2}\right)} \tag{6.40}$$

Figure 6.23 contains a plot of the data in this form. The points appear to collapse nicely on to a single line, as predicted by the theory. Also shown in the plot is a linear fit to the data. We can use this line as another test of the validity of the theory.

The gradient of this line is expected to be the surface tension of the subphase inside the annulus. Given that the experiment relies on the annuli acting as a barrier to surfactant, we expect this to be a pure water surface.

Taking the gradient of the fit, we obtain 76 ± 4 mN/m, where the error is the standard error calculated from the confidence bounds of the fit. This agrees within error with the expected value for pure water: 72 mN/m.

It would appear from these comparisons that the simple theory presented in Section 6.2 correctly predicts the nucleation pressures required for annuli to wrinkle, based on their dimensions. It is interesting to note that in this ultra-thin regime, the nucleation point is not dependant on either the thickness of the annulus or on its elastic properties.

In order to start to investigate the elastic properties, we instead need to consider the gradient of the wrinkling in its initial stage. Again we recall the expression derived in Section 6.2 for this (equation 6.38):

$$\frac{dn^2}{d\Pi} = \frac{12(1-\nu^2)}{Eh^3}\left(\frac{a^2b^2}{a^2-b^2}\right)\left(\left(\frac{2b^2}{b^2-a^2}\right)\ln\left(\frac{b}{a}\right)+\frac{1}{2}\right)$$

This then contains the Young's modulus and Poisson ratio of the annuli.

As with the nucleation pressure, we can write this in terms of a single parameter including all the annulus dimensions as so:

$$\frac{dn^2}{d\Pi} = \frac{12(1-\nu^2)}{Eh^3}Y \tag{6.41}$$

where:

$$Y = \frac{a^2b^2}{a^2-b^2}\left(\frac{2b^2}{b^2-a^2}\ln\left(\frac{b}{a}\right)+\frac{1}{2}\right) \tag{6.42}$$

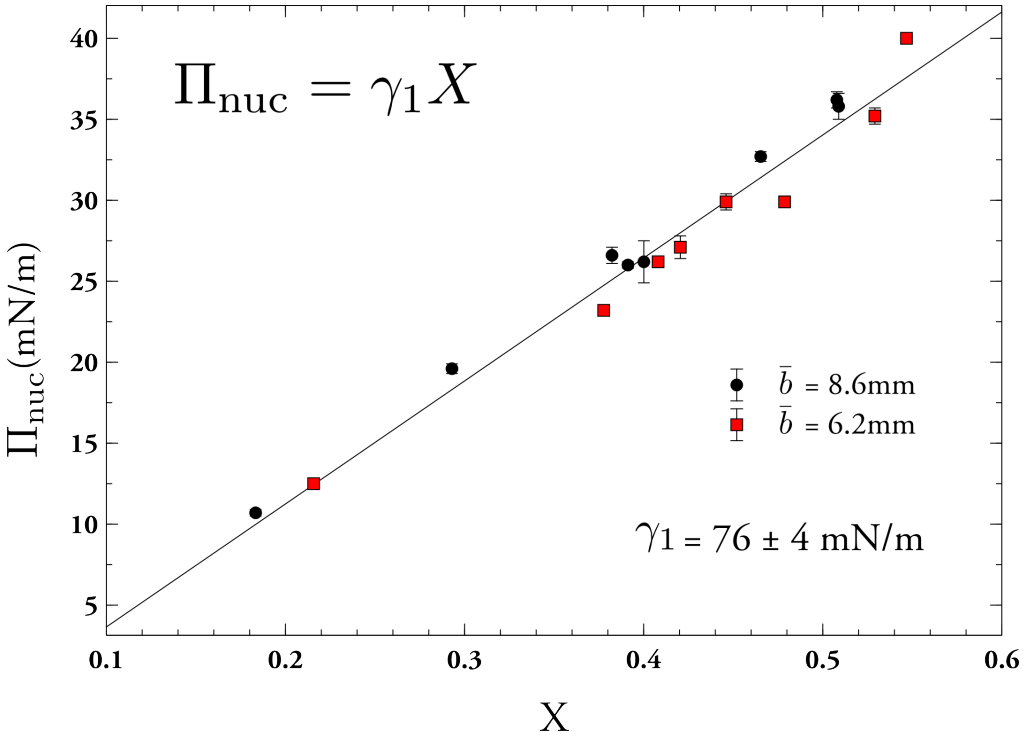

Figure 6.23: A plot showing the measured nucleation pressures of the annuli plotted against the combined dimensional parameter, X. The line is the result of a linear fit performed to all the data, which gives a gradient (surface tension of the sub-phase, γ_1) that agrees with the expected value for water within error.

The plot of the wrinkling gradient, $\frac{dn^2}{d\Pi}$ versus this parameter, Y is shown in Figure 6.24.

While the data once again appears to have collapsed to a similar region of the plot, it is clear that the agreement is not as good as with the nucleation pressures. The vertical error bars, calculated as the standard errors via the confidence bounds on the fits, are much larger than for the Π_{nuc} data points.

Also shown, as a black line, is a linear fit to the data. We have a measured value for h (131 nm), and can use a value for the Poisson ratio of polystyrene, $\nu = 0.33$ [16]. This means that by using the gradient of the fit, we can extract a value for the Young's modulus, E of the annuli.

It is expected that this value will be similar to the Young's modulus of bulk polystyrene, $E \sim 3$ GPa. The fit to the data in Figure 6.24, however, yields a Young's modulus: $E = 50 \pm 10$ GPa.

Even taking in to account the large uncertainty associated with this value it is clearly much larger than one might expect. As such, it suggests that the theory does not successfully describe the rate at which the number of wrinkles increase.

The theory currently overestimates the rate at which the number of wrinkles increases. We therefore need to consider additional forces acting on the annulus which may act to retard this.

We can neglect the effects of gravity as the amplitude of the wrinkles is far below that of the capillary length of water (~ 2 mm). One possible explanation is that as the annulus wrinkles, its surface area in contact with the water increases slightly, leading to an extra interfacial energy between the annulus and the water.

We can write an expression for this term by considering the change in area of the annulus due to the deflection around the annulus (Equation

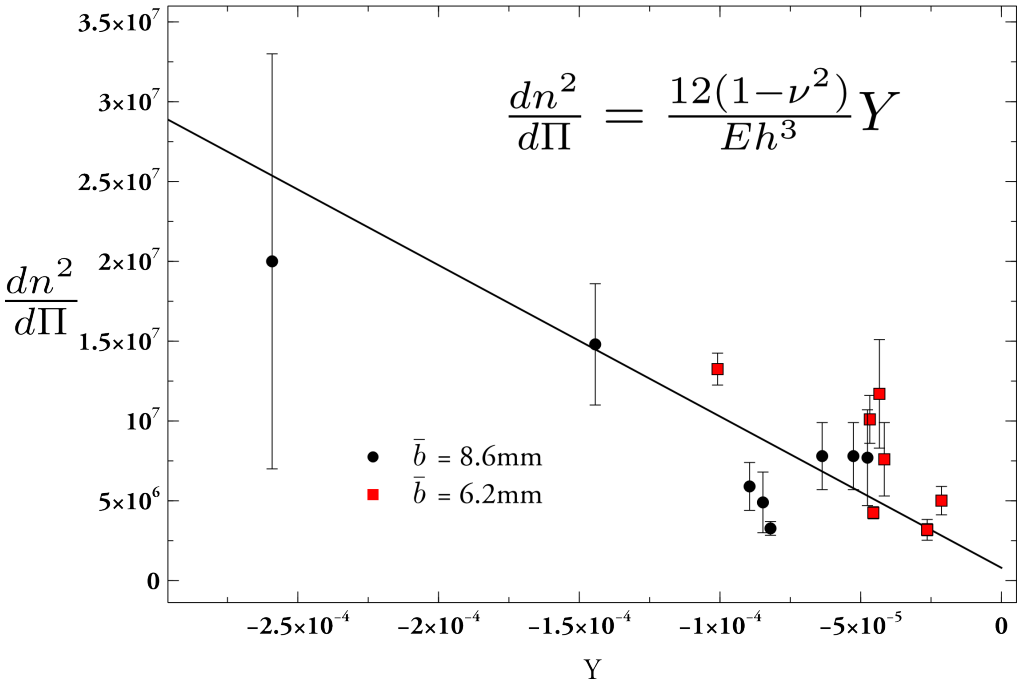

Figure 6.24: A plot showing the measured wrinkling gradients of the annuli plotted against the combined dimensional parameter, Y. The line is the result of a linear fit performed to all the data.

6.23):

$$w = w_0 \cos n\theta$$

By working this through (see Appendix B), we can obtain an expression for the change in area, ΔA:

$$\Delta A = \frac{\pi}{2} w_0^2 n^2 \ln\left(\frac{b}{a}\right) \tag{6.43}$$

We can then define another energy term related to this:

$$\Delta U_{\text{surf}} = \gamma_{\text{PS/water}} \Delta A = \gamma_{\text{PS/water}} \frac{\pi}{2} w_0^2 n^2 \ln\left(\frac{b}{a}\right) \tag{6.44}$$

where $\gamma_{\text{PS/water}}$ is the interfacial energy between polystyrene and water.

This term will then result in an additional term in the expression for n^2. This additional term, however, is not dependant on Π, so will disappear when the derivative $\frac{dn^2}{d\Pi}$ is taken. It will not, therefore, affect the expression for the wrinkling gradient.

Clearly, despite the success of the simple theory in predicting the nucleation pressure for wrinkling, it is not sufficient to describe the rate at which wrinkling occurs.

The obvious next step is to check whether the theory scales correctly and is simply missing some pre-factor. To do this, it is clear that more data needs to be collected. In particular, annuli of different thicknesses need to be tried as Equation 6.38 predicts that the wrinkling gradient will scale as $\sim h^{-3}$. Unfortunately, time did not allow for this data to be collected as part of this project.

Huang *et al.* [80] had success using scaling laws and fitting to independently known values to empirically determine the constants related to their wrinkling patterns. Assuming a similar process could be followed here, it opens up the potential for this technique to be used for further investigations of polymer properties.

A key advantage over Huang *et al.*, beyond the greater control of the applied stress, is the potential to measure polymer films down to smaller thicknesses. This is because, in the annulus technique, there is no requirement for the film to be strong enough to support a droplet. The method used to make the annuli is scalable, with spin coating still being suitable for producing thinner films. Care will be needed while annealing as ultra-thin films are susceptible to dewetting during this process, due to the relatively unfavourable surface energy of a very thin film. Floating films with very low thicknesses is also a delicate procedure and may require the use of higher molecular weight polymers to avoid them breaking apart.

These challenges, while significant, are surmountable thus opening up the possibility of being able to measure films with thicknesses approaching the rms end to end distance, R_{rms}, of the polymer chains - a key area of polymer research.

6.6 Conclusion

In summary, significant progress has been made towards using capillary wrinkling in floated polymer annuli to investigate their elastic properties.

The technique used builds on previous investigations in to capillary wrinkling in ultra-thin films. By using a polymer annulus floated on an LB trough, the stress applied to the film can be controlled reproducibly with a high degree of accuracy. This is a key advantage as a single annulus can be measured over range of surface pressures.

Several experimental hurdles have been overcome and a consistent method for creating, floating and imaging the annuli has been arrived at. Counting the wrinkles has been partly automated reducing the time needed to analyse the experimental data.

A simple theory has been proposed to describe the wrinkling behaviour

in terms of the elastic properties the polymer it's made from. By balancing terms for the strain energy stored in an annulus under compression and for the work done by bending stresses during wrinkling it is possible to accurately predict the surface pressure at which wrinkles begin to nucleate.

The theory was also designed to account for the rate at which the number of wrinkles increased with increasing surface pressure. Here, it was not a success, providing a measurement of the Young's modulus of polystyrene over 10 times larger than the accepted value.

Clearly, a more in depth treatment of the theory is needed, beyond the scope of this work. Another possibility would be to empirically investigate the data using a series of scaling laws.

Either way, it is clear that this technique has the potential to be used for investigating the elastic properties of ultra-thin polymer films down to the scale of a few dozen nanometres, an area of great interest.

7. Conclusion

This thesis contains a variety of investigations of the behaviour of polymers at the nanoscale. In particular we have investigated ultra thin films and multilayers. Due to the relative ease of processing polymers in to ultra-thin structures such as these, they are an interesting material to study.

Our manufacturing capabilities for devices such as electrical and optical components are now reaching the nanoscale. As we reach this level there is a clear need to investigate new materials and their behaviour in this regime. Polymer and other soft materials have a key advantage in this area as, compared to crystalline or hard materials, they are often much cheaper and easier to process.

As with any material we wish to investigate, we must first develop reliable methods for doing this. There are a variety of established ways of investigating ultra-thin polymer films, ellipsometry for example, but finding simple new ways to investigate their mechanical and elastic properties is still an important area.

While investigating the properties of these materials at a fundamental level is important, we also need to consider whether or not they are suitable for making devices that could complement, improve or replace existing technologies. The experiments carried out as part of this thesis aimed to cover both of these areas.

The final experimental chapter, on capillary wrinkling phenomena in polymer annuli, dealt primarily with the the first of these goals. It detailed attempts to measure the elastic properties, primarily the Young's modulus, of ultra-thin floated polymer films in a new and controllable way.

The experimental procedure consisted of making polymer annuli, floating them on a Langmuir-Blodgett trough, placing surfactant on the surface

outside the annulus and moving the barriers to control the surface pressure difference between the inside and outside of the annulus.

The goal was to induce wrinkling patterns in the annuli and relate them to the applied surface pressure difference and the Young's modulus of the polymer. Great progress was made in imaging these wrinkle patterns and developing a method of accurately and efficiently counting the number of wrinkles. The experiments also proved to be reproducible and the surface pressure applied to be controllable and reversible.

A simple theory was described in order to account for this wrinkling pattern. This worked by balancing terms for the strain energy stored in an annulus under compression and for the work done by bending stresses during wrinkling.

The theory successfully predicted the form of the wrinkling, that they would nucleate at a well defined surface pressure and then increase in number as the pressure was increased. It also quantitatively predicted the nucleation pressure to a high degree of accuracy.

It was not successful, however, in quantitatively predicting the Young's modulus of the polymer, giving values an order of magnitude too high. The reasons for this are likely to lie in the assumptions used forming the model, notably that of a vanishingly small wrinkle amplitude.

To progress the work in this area, either a more rigorous theoretical treatment, or an empirical comparison to scaling laws based on the dimensions of the annuli is needed. These are both areas of interest for future investigations on this technique.

A particular area that shows promise as an investigation is changing the thickness of the annuli. The experiments here only considered a single thickness ($\sim$130 nm). Theoretically there is no reason why this technique could not be employed at a range of thickness, including much smaller thicknesses ($<$ 30 nm), as all that is required is a film that will float on a

water sub-phase.

This is a likely avenue for any future work as it could potentially include films with thicknesses in the regime where their mechanical and elastic properties (e.g. the glass transition temperature) are known to deviate from their bulk values (for example: Sharp *et al* 2003 [82]. It would be interesting to see how the Young's modulus of the film behaves in this situation.

The first two experimental chapters were based on high frequency acoustic measurements performed on polymer films. The picosecond acoustic technique used, is more normally used with crystalline materials. More recent investigations of polymers have proved fruitful [22,27] so it was hoped that this use could be developed further.

Furthermore, each of these chapters detailed attempts at assessing the possibility of using polymer films in this way as devices, one of the key goals mentioned above.

Chapter 4 looked at quantised vibrations in ultra-thin polystyrene films. Specifically, it looked at what effect loading the polymer film with some mass had on the observed frequency. One of the aims of this was to assess the suitability of using polymer films in the same way as the crystal in a quartz crystal microbalance (QCM). That is, as a highly sensitive mass sensor.

The experiments performed consisted of measuring the harmonic vibrational frequencies of a polystyrene films on a silicon substrate that was 'pumped' by an optically induced strain pulse. Areas of the film were then covered in various thicknesses of gold, from 2.5-30 nm.

When the film was pumped on these areas the vibrational frequencies were decreased. A theory consisting of matching the boundary conditions of the elastic wave equation in the structure was used to model this shift and excellent agreement between experiment and theory was obtained.

Furthermore, the analysis suggested that in certain regimes, the film may be sensitive to not only the mass of the load, but also its acoustic impedance. This, combined with the relatively high spatial resolution of the technique compared to conventional QCM suggests the potential of such films as mass sensors.

The theoretical sensitivity of the films is also much higher than current devices, thanks to the higher frequencies involved (GHz vs MHz). It should be noted, however, that the ability to resolve the frequency shifts to the same accuracy as a QCM limits the value of this.

Possible avenues for further study in this investigation are numerous. One key advantage of polymer films is the wide range of available surface chemistries that can be accessed. It is possible that by creating a film that is selective to certain biological molecules, proteins for example, then this could be used as a highly efficient bio-sensor.

To do this, it is likely that the film would need to be placed in a liquid environment. With careful cell design this is likely to be achievable but would require modification of the theory to take in to account the damping effect of the liquid medium.

Another barrier to their use as sensors is the complex optical set up and expensive laser required to create and detect the vibrations. Work is being carried out currently aiming to electrically generate and detect these pulses. If this is successful it would greatly reduce the complexity of the equipment required for these measurements.

Overall, the potential for ultra-thin polymer films to be used as sensors in this way is clear, although experimental hurdles remain before this is likely to be realised.

The second acoustic chapter, Chapter 5, is again looking a high frequency measurements in polymer. This time, however, a multilayer system is considered. Again, while the fundamental physics of the optical be-

haviour of a multilayer as a strain pulse travels through it was of great interest, there remains a possibility that similar structures could be included in, or form the basis of high frequency optical components.

The experiments performed consisted of observing the change in the reflected intensity of a laser beam from a polymer bragg reflector. The bragg reflector was designed so that the photonic band gap was in the same vicinity as the laser wavelength. By changing the angle of incidence, the position of the laser wavelength relative to the band gap could be adjusted to be inside it, or on the edge.

It was observed that when a strain pulse was passed through the multilayer, the reflected intensity was modulated. Comparing these signals with numerically generated signals provided by a collaborator suggests that the dominant source of this modulation is via the photoelastic effect. That is, the light being reflected by the strain pulse as it travels through the structure.

For the polymer structure considered here, the optical modulation is small ($\sim 1\%$). While this precludes such a structure being useful for modulating light by itself, it is possible that it could be used as part of a component to achieve this.

For example, it was recently proposed that strong photon-phonon interactions in optical microcavitites formed using bragg reflectors can be used for light modulation in optoelectronic devices [59, 73–75]. In this case the modulation takes place in the cavity layer and any acousto-optic effects in the bragg reflectors should be minimal.

It is possible, therefore, that structures such as the polymer multilayers used heremay be used to engineer various nanophotonic devices based on bragg reflectors where efficient GHz modulation of light using acousto-optical effects is required.

It is clear from each of the investigations in this thesis that polymers

remain interesting materials with great potential. The works here that focussed on their acoustic and elastic properties at a small scale provide a taste of the rich physics accessible in these structures.

More than that, as our understanding and manufacturing capabilities with polymers nano-structures increase, they hold extreme potential for new range of nanoscale devices in the future.

A. The distribution function of an ideal random walk

We wish to derive a probability distribution for an ideal polymer chain that tells us how the monomers are spread out. To start, we consider a one dimensional random walk as shown in Figure A.1.

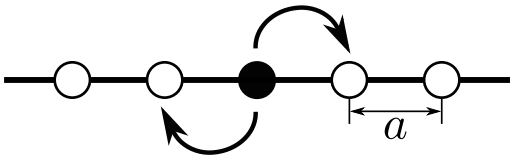

Figure A.1: A one dimensional random walk where either a step forward, N_+, or a step back, N_-, are the only options. Each step is of length a, the length of a monomer unit.

Each step in the walk is length a. There are a total of N steps that can be either forward, N_+, or backwards, N_-. The end to end distance of chain can then be written as,

$$R_x = a(N_+ - N_-) \tag{A.1}$$

To get our distribution function we must obtain the statistical weight, Ω, for a given R_x. We do this by calculating the number of possible combinations of walks that give an end to end distance of R_x. This is equivalent to the number of ways or combinations of obtaining N_+ forward steps from a total of N steps:

$$\Omega_{R_x} = \frac{N!}{N_+!(N - N_+)!} \tag{A.2}$$

It is useful at this point to recall that the entropy of this arrangement

can be written, $S = k_B \ln \Omega_{R_x}$. We now define:

$$f = \frac{N_+}{N} \tag{A.3}$$

$$1 - f = \frac{N - N_+}{N} \tag{A.4}$$

Substituting A.3 and A.4 into A.2 and taking the natural logarithm we obtain:

$$\ln \Omega_{R_x} = -N\big(f \ln f + (1-f)\ln(1-f)\big) \tag{A.5}$$

The equilibrium of the distribution corresponds to the point with the highest entropy (or statistical weight). $\ln \Omega_{R_x}$ is maximum when

$$\frac{\mathrm{d}(\ln \Omega_{R_x})}{\mathrm{d}f} = 0$$

Now,

$$\begin{aligned}\frac{\mathrm{d}(\ln \Omega_{R_x})}{\mathrm{d}f} &= -N\big(\ln f - \ln(1-f)\big) \\ &= -N \ln\left(\frac{f}{1-f}\right)\end{aligned} \tag{A.6}$$

A.6 is zero when $\ln\left(\frac{f}{1-f}\right) = 0$, i.e. $\frac{f}{1-f} = 1$ so $f = \frac{1}{2}$.

We can now expand $\ln \Omega_{R_x}$ about $f = \frac{1}{2}$:

$$\begin{aligned}\ln \Omega_{R_x} = \ln \Omega_{R_x}|_{f=\frac{1}{2}} &+ \left(f - \frac{1}{2}\right) \left.\frac{\mathrm{d}(\ln \Omega_{R_x})}{\mathrm{d}f}\right|_{f=\frac{1}{2}} \cdots \\ &+ \frac{1}{2}\left(f - \frac{1}{2}\right)^2 \left.\frac{\mathrm{d}^2(\ln \Omega_{R_x})}{\mathrm{d}f^2}\right|_{f=\frac{1}{2}} + \ldots\end{aligned} \tag{A.7}$$

Considering $\ln \Omega_{R_x}|_{f=\frac{1}{2}}$ and its derivatives,

$$\begin{aligned}\ln \Omega_{R_x}|_{f=\frac{1}{2}} &= -N\left(\frac{1}{2}\ln\left(\frac{1}{2}\right) + \frac{1}{2}\ln\left(\frac{1}{2}\right)\right) \\ &= -N\left(\ln\frac{1}{2}\right) = N \ln 2\end{aligned} \tag{A.8}$$

$$\left.\frac{\mathrm{d}(\ln \Omega_{R_x})}{\mathrm{d}f}\right|_{f=\frac{1}{2}} = 0 \tag{A.9}$$

$$\frac{\mathrm{d}^2(\ln \Omega_{R_x})}{\mathrm{d}f^2} = \frac{\mathrm{d}}{\mathrm{d}f}\left(-N\big(\ln f - \ln(1-f)\big)\right)$$
$$= -N\left(\frac{1}{f} + \frac{1}{1-f}\right)$$

So,

$$\left.\frac{\mathrm{d}^2(\ln \Omega_{R_x})}{\mathrm{d}f^2}\right|_{f=\frac{1}{2}} = -4N \tag{A.10}$$

Now, inserting A.8, A.9 and A.10 into A.7 we have,

$$\ln \Omega_{R_x} = N \ln 2 - 2N\left(f - \frac{1}{2}\right)^2 \tag{A.11}$$

Using A.1 we can write f in terms of R_x:

$$f = \frac{R_x}{2Na} + \frac{1}{2}$$

inserting this into A.11 we have:

$$\ln \Omega_{R_x} = N \ln 2 - \frac{R_x^2}{2Na^2}$$

and so the statistical weight for a given end to end distance for a one dimensional random walk is:

$$\Omega_{R_x} = Ce^{-\frac{R_x^2}{2Na^2}} \tag{A.12}$$

where C is some constant.

We may now generalize this result to three dimensions to describe our ideal polymer chain. For a 3D random walk, x, y and z steps are independent so:

$$\Omega_{\mathrm{TOT}} = \Omega_{R_x}\Omega_{R_y}\Omega_{R_z}$$
$$\propto e^{-\frac{R_x^2}{2Na_x^2} - \frac{R_y^2}{2Na_y^2} - \frac{R_z^2}{2Na_z^2}} \tag{A.13}$$

Now, using vector notation: $R^2 = R_x^2 + R_y^2 + R_z^2$, $a_x \simeq a_y \simeq a_z$ and if $a^2 = a_x^2 + a_y^2 + a_z^2$ then $a_x = a_y = a_z = \frac{a^2}{3}$. So, our final result for the distribution function of an ideal random walk is:

$$\boxed{\Omega_R = Ae^{-\frac{3R^2}{2Na^2}}} \tag{A.14}$$

where A is a normalisation constant.

B. The change in surface area of a wrinkled annulus

We wish to derive the additional surface area, ΔA, of an annulus when it wrinkles via a deflection, w.

The additional area when the annulus wrinkles is simply the total area of the wrinkled annulus, A_w, minus the initial surface area. That is:

$$\Delta A = A_w - \pi(b^2 - a^2) \tag{B.1}$$

We can define a unit area of the wrinkled annulus:

$$dA_w = dl.dr \tag{B.2}$$

where dl is a unit length around the circumference of the annulus. Taking in to account the deflection, w, we can then write:

$$dA_w = \sqrt{r^2 + \left(\frac{dw}{d\theta}\right)^2}\, d\theta dr \tag{B.3}$$

and so:

$$A_w = \int_a^b \int_0^{2\pi} \sqrt{r^2 + \left(\frac{dw}{d\theta}\right)^2}\, d\theta dr \tag{B.4}$$

We remember that w has the form:

$$w = w_0 \cos(n\theta) \tag{B.5}$$

so we can write:

$$A_w = \int_a^b \int_0^{2\pi} r\left(1 + \frac{w_0^2 n^2}{r^2}\sin^2(n\theta)\right)^{\frac{1}{2}} d\theta dr \tag{B.6}$$

Now,

$$\left(1 + \frac{w_0^2 n^2}{r^2}\sin^2(n\theta)\right)^{\frac{1}{2}} \approx 1 + \frac{w_0^2 n^2}{2r^2}\sin^2(n\theta) + \ldots \tag{B.7}$$

when,

$$\frac{w_0^2 n^2}{r^2} \ll 1 \tag{B.8}$$

which is true for small wrinkling amplitudes. Thus we have:

$$A_w = \int_a^b \int_0^{2\pi} \left(r + \frac{w_0^2 n^2}{2r} \sin^2(n\theta) \right) d\theta dr \tag{B.9}$$

$$= \pi(b^2 - a^2) + \frac{\pi}{2} w_0^2 n^2 \ln\left(\frac{b}{a}\right) \tag{B.10}$$

and so:

$$\boxed{\Delta A = \frac{\pi}{2} w_0^2 n^2 \ln\left(\frac{b}{a}\right)} \tag{B.11}$$

References

[1] W. Gratzer, *Giant Molecules: From nylon to nanotubes*. Oxford University Press, 2009.

[2] H.-H. Greve, "Rubber, 2. Natural," in *Ullmann's Encyclopedia of Industrial Chemistry*, 2000.

[3] R. A. L. Jones, *Soft Condensed Matter*. Oxford University Press, 2002.

[4] D. B. Hall, P. Underhill, and J. M. Torkelson, "Spin coating of thin and ultrathin polymer films," *Polymer Engineering & Science*, vol. 38, pp. 2039–2045, dec 1998.

[5] M. W. Matsen, "Thin films of block copolymer," *The Journal of Chemical Physics*, vol. 106, no. 18, p. 7781, 1997.

[6] M. J. Fasolka and A. M. Mayes, "Block Copolymer Thin Films : Physics and Applications," *Annual Review of Materials Research*, vol. 31, pp. 323–355, aug 2001.

[7] M. Poot and H. S. van der Zant, "Mechanical systems in the quantum regime," *Physics Reports*, vol. 511, no. 5, pp. 273 – 335, 2012.

[8] T. Gorishnyy, M. Maldovan, C. Ullal, and E. L. Thomas, "Sound ideas," *Physics World*, vol. 18, no. December, 2005.

[9] K. Jensen, K. Kim, and a. Zettl, "An atomic-resolution nanomechanical mass sensor.," *Nature nanotechnology*, vol. 3, pp. 533–7, sep 2008.

[10] Y. T. Yang, C. Callegari, X. L. Feng, K. L. Ekinci, and M. L. Roukes, "Zeptogram-scale nanomechanical mass sensing.," *Nano letters*, vol. 6, pp. 583–6, apr 2006.

[11] J. Chan, T. P. M. Alegre, A. H. Safavi-Naeini, J. T. Hill, A. Krause, S. Gröblacher, M. Aspelmeyer, and O. Painter, "Laser cooling of a nanomechanical oscillator into its quantum ground state.," *Nature*, vol. 478, pp. 89–92, oct 2011.

[12] J. D. Teufel, T. Donner, D. Li, J. W. Harlow, M. S. Allman, K. Cicak, a. J. Sirois, J. D. Whittaker, K. W. Lehnert, and R. W. Simmonds, "Sideband cooling of micromechanical motion to the quantum ground state.," *Nature*, vol. 475, pp. 359–63, jul 2011.

[13] R. Bowley and M. Sánchez, *Introductory Statistical Mechanics*. Oxford science publications, Clarendon Press, 1999.

[14] G. Adam and J. H. Gibbs, "On the Temperature Dependence of Cooperative Relaxation Properties in Glass-Forming Liquids," *The Journal of Chemical Physics*, vol. 43, no. 1, p. 139, 1965.

[15] J. A. Forrest and R. A. L. Jones, "The Glass Transition and Relaxation Dynamics in Thin Polymer Films," in *Polymer Surfaces, Interfaces and Thin Films*, pp. 251–294, 2000.

[16] J. Brandrup, E. H. Immergut, E. A. Grulke, A. Abe, and D. R. Bloch, *Polymer Handbook*. Wiley New York, 1999.

[17] R. N. Haward and R. J. Young, eds., *The Physics of Glassy Polymers*. Dordrecht: Springer Netherlands, 1997.

[18] L. E. Kinsler, A. R. Frey, A. B. Coppens, and J. V. Sanders, *Fundamentals of Acoustics (4th Edition)*. Wiley, 2000.

[19] R. Azzam and N. Bashara, *Ellipsometry and polarized light*. North-Holland personal library, North-Holland Pub. Co., 1977.

[20] C. Thomsen, J. Strait, Z. Vardeny, H. Maris, J. Tauc, and J. Hauser, "Coherent Phonon Generation and Detection by Picosecond Light Pulses," *Physical Review Letters*, vol. 53, pp. 989–992, sep 1984.

[21] C. Thomsen, H. Grahn, H. Maris, and J. Tauc, "Surface generation and detection of phonons by picosecond light pulses," *Physical Review B*, vol. 34, pp. 4129–4138, sep 1986.

[22] P. M. Walker, J. S. Sharp, A. V. Akimov, and A. J. Kent, "Coherent elastic waves in a one-dimensional polymer hypersonic crystal," *Applied Physics Letters*, vol. 97, no. 7, p. 073106, 2010.

[23] A. Bruchhausen, R. Gebs, F. Hudert, D. Issenmann, G. Klatt, A. Bartels, O. Schecker, R. Waitz, A. Erbe, E. Scheer, J. Huntzinger, A. Mlayah, and T. Dekorsy, "Subharmonic Resonant Optical Excitation of Confined Acoustic Modes in a Free-Standing Semiconductor Membrane at GHz Frequencies with a High-Repetition-Rate Femtosecond Laser," *Physical Review Letters*, vol. 106, no. 7, p. 077401, 2011.

[24] I. S. Grudinin, H. Lee, O. Painter, and K. J. Vahala, "Phonon Laser Action in a Tunable Two-Level System," *Physical Review Letters*, vol. 104, p. 083901, feb 2010.

[25] A. D. O'Connell, M. Hofheinz, M. Ansmann, R. C. Bialczak, M. Lenander, E. Lucero, M. Neeley, D. Sank, H. Wang, M. Weides, J. Wenner, J. M. Martinis, and A. N. Cleland, "Quantum ground state and single-phonon control of a mechanical resonator.," *Nature*, vol. 464, pp. 697–703, apr 2010.

[26] C. J. Morath and H. J. Maris, "Phonon attenuation in amorphous solids studied by picosecond ultrasonics," *Phys. Rev. B*, vol. 54, pp. 203–213, Jul 1996.

[27] A. V. Akimov, E. S. K. Young, J. S. Sharp, V. Gusev, and A. J. Kent, "Coherent hypersonic closed-pipe organ like modes in supported polymer films," *Applied Physics Letters*, vol. 99, no. 2, p. 021912, 2011.

[28] S. Y. Chou, P. R. Krauss, and P. J. Renstrom, "Imprint Lithography with 25-Nanometer Resolution," *Science*, vol. 272, pp. 85–87, apr 1996.

[29] C. Park, J. Yoon, and E. L. Thomas, "Enabling nanotechnology with self assembled block copolymer patterns," *Polymer*, vol. 44, pp. 6725–6760, oct 2003.

[30] D. a. LaVan, T. McGuire, and R. Langer, "Small-scale systems for in vivo drug delivery.," *Nature biotechnology*, vol. 21, pp. 1184–91, oct 2003.

[31] N. a. Melosh, A. Boukai, F. Diana, B. Gerardot, A. Badolato, P. M. Petroff, and J. R. Heath, "Ultrahigh-density nanowire lattices and circuits.," *Science*, vol. 300, pp. 112–5, apr 2003.

[32] K. Besteman, J.-O. Lee, F. G. M. Wiertz, H. a. Heering, and C. Dekker, "Enzyme-Coated Carbon Nanotubes as Single-Molecule Biosensors," *Nano Letters*, vol. 3, pp. 727–730, jun 2003.

[33] P. Alivisatos, "The use of nanocrystals in biological detection.," *Nature biotechnology*, vol. 22, pp. 47–52, jan 2004.

[34] J. N. Anker, W. P. Hall, O. Lyandres, N. C. Shah, J. Zhao, and R. P. Van Duyne, "Biosensing with plasmonic nanosensors.," *Nature materials*, vol. 7, pp. 442–53, jun 2008.

[35] J. L. Arlett, E. B. Myers, and M. L. Roukes, "Comparative advantages of mechanical biosensors.," *Nature nanotechnology*, vol. 6, pp. 203–15, apr 2011.

[36] K. A. Marx, "Quartz crystal microbalance: A useful tool for studying thin polymer films and complex biomolecular systems at the solution - Surface interface," 2003.

[37] H. Ogi, H. Nagai, H. Naga, Y. Fukunishi, M. Hirao, and M. Nishiyama, "170-MHz electrodeless quartz crystal microbalance biosensor: capability and limitation of higher frequency measurement.," *Analytical chemistry*, vol. 81, pp. 8068–73, oct 2009.

[38] F. Höök, B. Kasemo, T. Nylander, C. Fant, K. Sott, and H. Elwing, "Variations in coupled water, viscoelastic properties, and film thickness of a Mefp-1 protein film during adsorption and cross-linking: a quartz crystal microbalance with dissipation monitoring, ellipsometry, and surface plasmon resonance study.," *Analytical chemistry*, vol. 73, pp. 5796–804, dec 2001.

[39] F. Höök, J. Vörös, M. Rodahl, R. Kurrat, P. Böni, J. Ramsden, M. Textor, N. Spencer, P. Tengvall, J. Gold, and B. Kasemo, "A comparative study of protein adsorption on titanium oxide surfaces using in situ ellipsometry, optical waveguide lightmode spectroscopy, and quartz crystal microbalance/dissipation," *Colloids and Surfaces B: Biointerfaces*, vol. 24, pp. 155–170, mar 2002.

[40] F. Bender, P. Roach, A. Tsortos, G. Papadakis, M. I. Newton, G. Mchale, and E. Gizeli, "Development of a combined surface plasmon resonance / surface acoustic wave device for the characterization of biomolecules," *Measurement Science and Technology*, vol. 20, p. 124011, 2009.

[41] J. Chaste, M. Sledzinska, M. Zdrojek, J. Moser, and a. Bachtold, "High-frequency nanotube mechanical resonators," *Applied Physics Letters*, vol. 99, no. 21, p. 213502, 2011.

[42] T. Maeda, H. Otsuka, and A. Takahara, "Dynamic covalent polymers: Reorganizable polymers with dynamic covalent bonds," *Progress in Polymer Science*, vol. 34, pp. 581–604, jul 2009.

[43] R. J. Wojtecki, M. a. Meador, and S. J. Rowan, "Using the dynamic bond to access macroscopically responsive structurally dynamic polymers.," *Nature materials*, vol. 10, pp. 14–27, jan 2011.

[44] B. Adhikari and S. Majumdar, "Polymers in sensor applications," *Progress in Polymer Science*, vol. 29, pp. 699–766, jul 2004.

[45] E. W. Weisstein, "Newton's Method."

[46] M. Maldovan, "Sound and heat revolutions in phononics," *Nature*, vol. 503, pp. 209–217, nov 2013.

[47] B. Jusserand, D. Paquet, F. Mollot, F. Alexandre, and G. Le Roux, "Influence of the supercell structure on the folded acoustical Raman line intensities in superlattices," *Physical Review B*, vol. 35, no. 6, pp. 2808–2817, 1987.

[48] T. Gorishnyy, C. Ullal, M. Maldovan, G. Fytas, and E. Thomas, "Hypersonic Phononic Crystals," *Physical Review Letters*, vol. 94, pp. 1–4, mar 2005.

[49] W. Cheng, J. Wang, U. Jonas, G. Fytas, and N. Stefanou, "Observation and tuning of hypersonic bandgaps in colloidal crystals.," *Nature materials*, vol. 5, pp. 830–6, oct 2006.

[50] J. Groenen, F. Poinsotte, a. Zwick, C. Sotomayor Torres, M. Prunnila, and J. Ahopelto, "Inelastic light scattering by longitudinal acoustic phonons in thin silicon layers: From membranes to silicon-on-insulator structures," *Physical Review B*, vol. 77, p. 045420, jan 2008.

[51] X. Zhang, R. Sooryakumar, a. Every, and M. Manghnani, "Observation of organ-pipe acoustic excitations in supported thin films," *Physical Review B*, vol. 64, p. 081402, aug 2001.

[52] P. Dainese, P. S. J. Russell, G. S. Wiederhecker, N. Joly, H. L. Fragnito, V. Laude, and A. Khelif, "Raman-like light scattering from acoustic phonons in photonic crystal fiber," *Optics Express*, vol. 14, p. 4141, dec 2006.

[53] G. Wiederhecker, A. Brenn, H. Fragnito, and P. Russell, "Coherent Control of Ultrahigh-Frequency Acoustic Resonances in Photonic Crystal Fibers," *Physical Review Letters*, vol. 100, p. 203903, may 2008.

[54] J.-C. Beugnot and V. Laude, "Electrostriction and guidance of acoustic phonons in optical fibers," *Physical Review B*, vol. 86, p. 224304, dec 2012.

[55] Q. Lin, J. Rosenberg, D. Chang, R. Camacho, M. Eichenfield, K. J. Vahala, and O. Painter, "Coherent mixing of mechanical excitations in nano-optomechanical structures," *Nature Photonics*, vol. 4, pp. 236–242, feb 2010.

[56] S. Weis, R. Rivière, S. Deléglise, E. Gavartin, O. Arcizet, A. Schliesser, and T. J. Kippenberg, "Optomechanically induced transparency.," *Science (New York, N.Y.)*, vol. 330, pp. 1520–3, dec 2010.

[57] L. Ding, C. Baker, P. Senellart, A. Lemaitre, S. Ducci, G. Leo, and I. Favero, "High Frequency GaAs Nano-Optomechanical Disk Resonator," *Physical Review Letters*, vol. 105, p. 263903, dec 2010.

[58] A. H. Safavi-Naeini, T. P. M. Alegre, M. Winger, and O. Painter, "Optomechanics in an ultrahigh-Q two-dimensional photonic crystal cavity," *Applied Physics Letters*, vol. 97, no. 18, p. 181106, 2010.

[59] A. Fainstein, N. D. Lanzillotti-Kimura, B. Jusserand, and B. Perrin, "Strong Optical-Mechanical Coupling in a Vertical GaAs/AlAs Microcavity for Subterahertz Phonons and Near-Infrared Light," *Physical Review Letters*, vol. 110, p. 037403, jan 2013.

[60] O. Arcizet, P.-F. Cohadon, T. Briant, M. Pinard, and a. Heidmann, "Radiation-pressure cooling and optomechanical instability of a micromirror.," *Nature*, vol. 444, pp. 71–4, nov 2006.

[61] I. Mahboob, K. Nishiguchi, a. Fujiwara, and H. Yamaguchi, "Phonon Lasing in an Electromechanical Resonator," *Physical Review Letters*, vol. 110, p. 127202, mar 2013.

[62] T.-R. Lin, C.-H. Lin, and J.-C. Hsu, "Enhanced acousto-optic interaction in two-dimensional phoxonic crystals with a line defect," *Journal of Applied Physics*, vol. 113, no. 5, p. 053508, 2013.

[63] M. Maldovan and E. L. Thomas, "Simultaneous localization of photons and phonons in two-dimensional periodic structures," *Applied Physics Letters*, vol. 88, no. 25, p. 251907, 2006.

[64] A. Akimov, Y. Tanaka, a. Pevtsov, S. Kaplan, V. Golubev, S. Tamura, D. Yakovlev, and M. Bayer, "Hypersonic Modulation of Light in Three-Dimensional Photonic and Phononic Band-Gap Materials," *Physical Review Letters*, vol. 101, pp. 1–4, jul 2008.

[65] E. Reed, M. Soljačić, and J. Joannopoulos, "Color of Shock Waves in Photonic Crystals," *Physical Review Letters*, vol. 90, pp. 1–4, may 2003.

[66] I. E. Psarobas, N. Papanikolaou, N. Stefanou, B. Djafari-Rouhani, B. Bonello, and V. Laude, "Enhanced acousto-optic interactions in a one-dimensional phoxonic cavity," *Physical Review B*, vol. 82, p. 174303, nov 2010.

[67] J. D. Joannopoulos, S. G. Johnson, J. N. Winn, and R. D. Meade, *Photonic Crystals: Molding the Flow of Light*. Princeton University Press, 2008.

[68] H. N. Lin, R. J. Stoner, H. J. Maris, and J. Tauc, "Phonon attenuation and velocity measurements in transparent materials by picosecond acoustic interferometry," *Journal of Applied Physics*, vol. 69, no. 7, p. 3816, 1991.

[69] A. A. Maznev, K. J. Manke, C. Klieber, K. A. Nelson, S. H. Baek, and C. B. Eom, "Coherent Brillouin spectroscopy in a strongly scattering liquid by picosecond ultrasonics.," *Optics letters*, vol. 36, pp. 2925–7, aug 2011.

[70] J. W. Tucker and V. W. Rampton, *Microwave Ultrasonics in Solid State Physics*. North Holland Publishing Company, 1972.

[71] J. Bailey and J. S. Sharp, "Thin film polymer photonics: Spin cast distributed Bragg reflectors and chirped polymer structures.," *The European physical journal. E, Soft matter*, vol. 33, pp. 41–9, sep 2010.

[72] Y. Kurokawa, "Adsorption of water on cellulose acetate membrane," *Desalination*, vol. 36, no. 3, pp. 285–290, 1981.

[73] T. Czerniuk, C. Brüggemann, J. Tepper, S. Brodbeck, C. Schneider, M. Kamp, S. Höfling, B. A. Glavin, D. R. Yakovlev, A. V. Akimov, and M. Bayer, "Lasing from active optomechanical resonators.," *Nature communications*, vol. 5, p. 4038, jan 2014.

[74] Y. Léger, "Double Magic Coincidence in an Optomechanical Laser Cavity," *Physics*, vol. 6, p. 6, jan 2013.

[75] C. Brüggemann, A. V. Akimov, A. V. Scherbakov, M. Bombeck, C. Schneider, S. Höfling, A. Forchel, D. R. Yakovlev, and M. Bayer, "Laser mode feeding by shaking quantum dots in a planar microcavity," *Nature Photonics*, vol. 6, pp. 30–34, nov 2011.

[76] E. Cerda and L. Mahadevan, "Geometry and Physics of Wrinkling," *Physical Review Letters*, vol. 90, p. 074302, feb 2003.

[77] E. Cerda, K. Ravi-Chandar, and L. Mahadevan, "Thin films. Wrinkling of an elastic sheet under tension.," *Nature*, vol. 419, no. 6907, pp. 579–580, 2002.

[78] J. Genzer and J. Groenewold, "Soft matter with hard skin: From skin wrinkles to templating and material characterization," *Soft Matter*, vol. 2, no. 4, p. 310, 2006.

[79] E. Cerda, "Mechanics of scars," *Journal of Biomechanics*, vol. 38, no. 8, pp. 1598–1603, 2005.

[80] J. Huang, M. Juszkiewicz, W. H. de Jeu, E. Cerda, T. Emrick, N. Menon, and T. P. Russell, "Capillary wrinkling of floating thin polymer films.," *Science (New York, N.Y.)*, vol. 317, pp. 650–3, aug 2007.

[81] M. Piñeirua, N. Tanaka, B. Roman, and J. Bico, "Capillary buckling of a floating annulus," *Soft Matter*, vol. 9, no. 46, p. 10985, 2013.

[82] J. Sharp and J. Forrest, "Free Surfaces Cause Reductions in the Glass Transition Temperature of Thin Polystyrene Films," *Physical Review Letters*, vol. 91, p. 235701, dec 2003.

[83] J. M. Torres, C. M. Stafford, and B. D. Vogt, "Elastic modulus of amorphous polymer thin films: relationship to the glass transition temperature.," *ACS nano*, vol. 3, no. 9, pp. 2677–85, 2009.

[84] Z. Ao and S. Li, "Temperature- and thickness-dependent elastic moduli of polymer thin films," *Nanoscale Research Letters*, vol. 6, no. 1, p. 243, 2011.

[85] C. M. Stafford, C. Harrison, K. L. Beers, A. Karim, E. J. Amis, M. R. VanLandingham, H.-C. Kim, W. Volksen, R. D. Miller, and E. E. Simonyi, "A buckling-based metrology for measuring the elastic moduli of polymeric thin films," *Nature Materials*, vol. 3, no. 8, pp. 545–550, 2004.

[86] W. Slaughter, *The Linearized Theory of Elasticity*. Birkhäuser Boston, 2002.

[87] T. Yu and W. Johnson, "The buckling of annular plates in relation to the deep-drawing process," *International Journal of Mechanical Sciences*, vol. 24, pp. 175–188, 1982.